



OPEN ACCESS

EDITED BY

Steven Koester,
University of Minnesota Twin Cities,
United States

REVIEWED BY

Alon Ascoli,
Technical University Dresden, Germany
Rivu Midya,
Massachusetts Institute of Technology,
United States

*CORRESPONDENCE

Wei Yi,
✉ wyi@hrl.com

RECEIVED 17 July 2024
ACCEPTED 17 February 2025
PUBLISHED 12 May 2025

CITATION

Yi W (2025) Nonlinear dynamics and stability analysis of locally active Mott memristors using a physics-based compact model. *Front. Mater.* 12:1465852. doi: 10.3389/fmats.2025.1465852

COPYRIGHT

© 2025 Yi. This is an open-access article distributed under the terms of the [Creative Commons Attribution License \(CC BY\)](#). The use, distribution or reproduction in other forums is permitted, provided the original author(s) and the copyright owner(s) are credited and that the original publication in this journal is cited, in accordance with accepted academic practice. No use, distribution or reproduction is permitted which does not comply with these terms.

Nonlinear dynamics and stability analysis of locally active Mott memristors using a physics-based compact model

Wei Yi*

Sensors and Electronics Laboratory, HRL Laboratories, LLC., Malibu, CA, United States

Locally active memristors (LAMs) are a class of emerging nonlinear dynamic circuit elements that hold promise for scalable yet biomimetic neuromorphic circuits. Starting from a physics-based compact model, we performed small-signal linearization analyses and applied Chua's local activity theory to a one-dimensional, locally active vanadium dioxide Mott memristor based on an insulator-to-metal phase transition. This approach establishes a connection between the dynamical behaviors of a Mott memristor and its physical device parameters, enabling a complete mapping of the locally passive and edge-of-chaos domains in the frequency and current operating parameter space. This mapping could guide materials and device development for neuromorphic circuit applications. We also examined the applicability of local analyses to a second-order relaxation oscillator circuit, which consists of a voltage-biased vanadium dioxide memristor coupled to a parallel reactive capacitor element and a series resistor. Chua's local activity criteria allows a mapping of this second-order system's dynamics and stability in the frequency and circuit parameter space, which is essentially a phase diagram for complexity. It shows that the coupling increases both the system's dimension and its dynamical complexity and creates a locally active and unstable region to host instabilities and persistent oscillations. We show that global nonlinear techniques, including nullclines and phase portraits, provide further insights into instabilities and persistent oscillations near non-hyperbolic fixed points. Specifically, we observe a supercritical Hopf-like bifurcation, where an orbitally stable limit cycle emerges as a new attractor when a stable spiral transitions to an unstable one, with each of the three circuit parameters acting as a bifurcation parameter. The abrupt growth of the limit cycle resembles the Canard explosion phenomenon observed in systems exhibiting relaxation oscillations. Finally, we show that experimental limit cycle oscillations in a vanadium dioxide nano-device relaxation oscillator closely match SPICE simulations based on the compact model.

KEYWORDS

local activity theory, edge of chaos, memristor, negative differential resistance, Mott insulator-to-metal phase transition, Hopf bifurcation, limit cycle, neuromorphic circuits

1 Introduction

In recent years, a surge of interest has been witnessed in exploiting nonlinear dynamical phenomena in emerging devices for novel circuit applications, such as

neuromorphic computing. A subject that has been intensively studied is one-port (two-terminal) passive memristors, which exhibit a pinched hysteresis that always passes through the origin in their current–voltage (I–V) loci, thereby possessing a non-volatile memory effect (Strukov et al., 2008; Dittmann and Strachan, 2019). Passive memristors offer a scalable and energy-efficient approach to emulating biological synapses and implementing computationally efficient neuromorphic learning rules (Kim et al., 2015; Wang et al., 2017; Covi et al., 2018; Brivio et al., 2021).

Although a canonical memristor is a passive circuit element, any one-port device that exhibits a pinched hysteresis is considered an extended memristor (Chua, 2014), which includes a class of one-port devices that exhibit non-monotonicity in their experimental quasi-direct current (quasi-DC) I–V curves—a negative differential resistance (NDR). These devices typically exhibit a pronounced I–V hysteresis when driven by a voltage stimulus; however, the hysteresis *collapses* at a finite voltage. Therefore, they only have a transient (volatile) memory effect. Importantly, these globally passive one-port devices are *locally active* within the NDR region. Under proper biasing conditions, they can function as one-port amplifiers that increase the power of an alternating-current (AC) signal applied to the same port. It was recently shown that a locally active memristor (LAM) in a distributed form can act as an axon-like signal-amplifying transmission line (Brown et al., 2024). Signal amplification is an essential capability for information processing and communication, a field that has been dominated by transistors. Figure 1 shows the comparison of typical quasi-DC I–V curves measured from a passive memristor and a locally active memristor. Such a measurement varies V or I stimulus slowly and measures time-averaged device responses, which could capture the resistance states before and after a resistance switching event (see arrows) but not the ultrafast switching dynamics that could occur within femtoseconds. Figure 1A shows a bipolar tantalum oxide ($\text{TaO}_x\text{-Ta}_2\text{O}_5$) passive memristor, which switches from a low-resistance state (LRS) to a high-resistance state (HRS) if a sufficiently large positive voltage is applied (Reset) and switches from the HRS back to the LRS if a sufficiently large negative voltage is applied (Set). Both Reset and Set operations are nonvolatile, i.e., resistance changes are retained even after power is turned off. In contrast, Figure 1B shows a unipolar vanadium dioxide (VO_2) locally active memristor, which abruptly switches from an HRS to an LRS if a sufficiently large voltage is applied, regardless of its polarity. As the voltage is reduced below a smaller threshold level, the device switches from the LRS back to the HRS—these resistance changes are volatile and are lost once the power is turned off. It should be noted that the exemplary characteristics in Figure 1 are by no means exhaustive. Passive memristors can exhibit either bipolar or unipolar non-volatile resistance switching behaviors, which are determined by the intertwined ionic and electronic transport mechanisms within the nanoscale device volume (Waser et al., 2009; Jeong et al., 2012). They may also exhibit a fading memory effect, where the asymptotic behavior is solely determined by the state dynamics, irrespective of the initial condition (Ascoli et al., 2016; Pershin and Slipko, 2019).

We now focus on one-port devices that possess the peculiar I–V characteristics shown in Figure 1B. One-port devices with such switching characteristics have been extensively studied and implemented in engineering practice. They have been made out of many materials based on a variety of operating

mechanisms. A familiar category is electro-thermal threshold switches such as ovonic threshold switches (OTSs), which show rapid changes in resistance due to nonlinear interactions among local temperature, metastable structural change, and electrical conductivity (Ovshinsky, 1968; Noé et al., 2020). Being a one-port device, LAMs and passive memristors share the same level of $4F^2$ (F: half pitch in lithography) scalability in a crossbar device geometry (Amsinck et al., 2005), resolving the trade-off between scalability and biological fidelity.

LAMs may generally be classified into two types, namely, current-controlled (S-type) and voltage-controlled (λ -type), where the letters “S” and “ λ ” resemble the characteristic shape of NDR in the I–V curve plotted with voltage as the x -axis (Ridley, 1963). S-type LAMs are “normally off” devices with an HRS when the power is turned off. λ -type LAMs such as resonant tunneling diodes are “normally on” devices with an LRS when the power is turned off (Esaki, 1958). Therefore, S-type LAMs are superior to λ -type LAMs in terms of standby power consumption. Hereafter, we focus our discussion on current-controlled LAMs.

A particularly interesting class of current-controlled LAMs is based on the insulator-to-metal phase transition (IMT) phenomena in strongly correlated materials that arise from a coupling between structural distortions (Peierls transition) and electronic instabilities (Mott transition) (Andrews et al., 2019). They possess several attractive features for circuit applications, such as ultralow (femtojoule) switching energy (Prinz et al., 2020), ultra-fast (tens of femtosecond) switching speed (Jager et al., 2017), and electroforming-free operations (Yi et al., 2018). We term all these IMT-based LAMs “Mott memristors” without discerning the subtle differences in their phase transition mechanisms. Vanadium dioxide (VO_2) and niobium dioxide (NbO_2) are two intensively studied Mott memristor materials among many others (Andrews et al., 2019).

For neuromorphic computing applications, circuits of self-excited oscillators and spiking neuron emulators have been built with one or more LAMs that are coupled with reactive elements (capacitors) (Farhat and Eldefrawy, 1993; Moon et al., 2015; Ignatov et al., 2015; Stoliar et al., 2017; Wang et al., 2018). An illustrative example is a scalable spiking neuron, which constitutes two oppositely energized (“polarized” in neuroscience glossary) LAMs to mimic the voltage-gated potassium and sodium cell membrane ion channels. When coupled with parallel membrane capacitors and series load resistors, the composite circuit emulates a single-compartment nerve cell, initiating all-or-nothing action potentials upon a suprathreshold stimulus (Yi et al., 2018; Pickett et al., 2013) or acting as a delayed buffer, which allows bidirectional, distortion-free propagation of action potentials when daisy-chained (Pickett and Williams, 2013; Yi, 2022). Such a circuit topology bears some resemblance to a biologically plausible Hodgkin–Huxley (HH) axon model (Chua et al., 2012) and the early 1960s proposals of “neuristor” axons utilizing non-scalable components such as inductors (Crane, 1960; Crane, 1962; Nagumo et al., 1962). Experimental spiking neurons built with VO_2 Mott memristors have shown about two dozen biological neuronal temporal dynamics, including all three classes of neuronal excitability (Yi et al., 2018). Arguably, LAM-based neurons and passive memristor-based synapses form a self-sufficient basis to construct a transistorless neural network (Yi and Cruz-Albrecht, 2019).

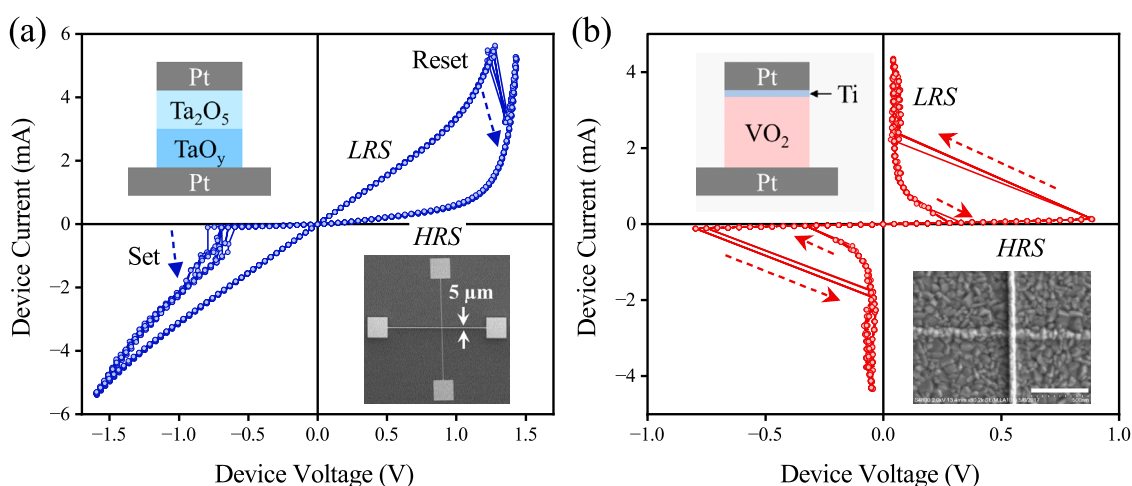


FIGURE 1

Experimental quasi-DC I–V curves for (A) a TaO_y-Ta₂O₅ bilayer passive memristor and (B) a VO₂ locally active memristor, constructed and characterized by HRL Laboratories, LLC. Resistance switching events are indicated by dashed arrows. (A) These insets show the layer structure and optical image of the 5 × 5 μm² TaO_y-Ta₂O₅ (y < 2) crossbar device. (B) These insets show the layer structure and scanning electron micrograph of the 50 × 50 nm² VO₂ nano-crossbar device (scale bar: 500 nm). Memristor crossbars are tested in a four-terminal Kelvin connection (see Yi et al. (2019) for details). The external voltage is swept at ~1 V/s rate in the sequence of 0 → +V_p → 0 → -V_n → 0 (repeated 10 times). V_p(V_n) = 2.5(2) V in (A) and V_{p,n} = 1.45 V in (B). The metal electrodes contribute a series resistance of 600–800 Ω.

Despite numerous experimental demonstrations, predictive modeling and analysis of LAM elements and circuits remain challenging and hinder technology development. These difficulties are, in part, due to the fundamental mathematical challenges associated with nonlinear differential systems. One illustrious example is the second part of Hilbert's 16th problem that questions whether there exists a finite upper bound for the number of limit cycles of planar polynomial differential systems. It remains unsolved today, even for quadratic polynomials (degree $n = 2$) (Ilyashenko, 2002). Qualitative local analyses, on the contrary, are facilitated by small-signal linearization techniques, which allow linear analysis to be applied to a nonlinear system near a *hyperbolic* fixed point with all eigenvalues of the linearization having non-zero real parts (Perko, 1991). A key theoretical contribution made by Chua is the local activity (LA) theorem, which provides a rigorous mathematical definition of the LA as a necessary prerequisite for the emergence of complexity in nonlinear systems (Chua, 2005). Moreover, Chua provided a set of explicit and computable criteria in the parameter space, which allows for identifying the *edge-of-chaos* (EOC) region that is both locally active and stable, where most of the complexity phenomena emerge. In recent years, Chua's LA principle has been applied to clarify several long unsolved fundamental problems about dissipative systems, including Prigogine's symmetry-breaking instability in homogeneous cellular media (Prigogine and Nicolis, 1967); the emergence of Turing instability (Turing, 1952) and its higher-order analog, Smale's paradox (Smale, 1976), in reaction-diffusion systems; and Hodgkin–Huxley all-or-nothing excitability of nerve cells (Hodgkin and Huxley, 1952). All these complex phenomena are associated with the EOC domain within a system's parameter space (Ascoli et al., 2022a; Ascoli et al., 2022b; Ascoli et al., 2022c; Chua, 2022).

Mathematically rigorous yet unphysical toy models of nonlinear dynamical elements were frequently used in the LA analysis

procedure (Mannan et al., 2016; Mannan et al., 2017). For engineering practice, such toy models fall short of establishing a connection between circuit- or network-level dynamics and the measurable physical properties of constituent components. A recent review thoroughly elaborated on the importance of applying appropriate device physics into the mathematical memristor framework and defining physically relevant model parameters to control the circuit dynamic behavior (Brown et al., 2022b).

The main objective of this manuscript is to apply relevant theoretical techniques to understand the dynamics and stability of nonlinear circuits that involve locally active Mott memristors and map the conditions for the LA regime within the design parameter space (Messaris et al., 2021; Ascoli et al., 2021). These theoretical techniques include essential local analysis methods such as the small-signal linearization and the LA theorem and global techniques such as the nullclines and phase portraits. For engineering relevance, we base our analyses on an analytical one-dimensional (1D) Mott memristor compact model that is built on the laws of thermodynamics and only contains physically relevant device parameters. The model was developed by Pickett and Williams for NbO₂ Mott memristors (Pickett and Williams, 2012). Previously, we have verified that it is also applicable to VO₂ Mott memristors after replacing the material properties (Oh et al., 2010; Berglund and Guggenheim, 1969), and our SPICE simulations based on this model faithfully reproduced most of the measured neuronal dynamics in neuron circuits built with VO₂ memristors (Yi et al., 2018). In this study, we demonstrate that this physics-based compact model is mathematically tractable for applying local and global analysis techniques, with closed-form expressions for all the important quantities involved in the analyses. It enables a connection between the system dynamics and component physical parameters to guide circuit designs and process development. The algorithmic analysis procedure we present using a VO₂ Mott

memristor model is general in nature and suitable for analyzing other Mott memristor materials. Qualitatively, the predictions regarding the dynamics and stability in this work are similar to those made by compact models based on different choices of state variables and kinetic functions (Brown et al., 2022b).

We focus on theoretical analyses and only included a cursory comparison between the model simulated and experimental characteristics of a VO₂ nano-device relaxation oscillator near the end. More detailed comparisons in the context of VO₂ Mott memristor neurons can be found in supplementary materials of Yi et al. (2018). It is understood that the compact model presented in this study has some simplifications and limitations. It is a nontrivial task to construct a computationally efficient compact model for locally active memristors with an appropriate balance between the dynamical fidelity and the computational complexity of solving the model equations. This is especially important for digital computer simulations of a scaled network that contains many instances of memristor elements, which could be costly in time and energy consumption.

The remainder of this paper is organized as follows: The first three sections (Sections 2–4) provide the analyses of an isolated 1D Mott memristor. In Section 2, we introduce the physics-based compact model and analyze the stability of an isolated 1D Mott memristor by examining its power-off plot (POP) and dynamic route map under constant input currents or voltages. This exercise confirms that the metallic state of a Mott memristor is unstable without power and is asymptotically stable with a finite input current. It also reveals that varying the voltage as the bifurcation parameter leads to a supercritical saddle-node bifurcation. In Section 3, we solve its locus of steady states (fixed points) in the three-dimensional (3D) state space and their two-dimensional (2D) projections. Note that we use both fixed point and steady state for the same concept in an interchangeable manner but avoid the term equilibrium unless the input is 0. See Subsection 2.2 for an elaboration on this topic.

In Section 4, we apply local analysis techniques on an isolated Mott memristor, including linearization and small-signal analysis, pole-zero diagram, Chua's LA theorem, and frequency response. Its complex domain (*s*-domain) equivalent circuit derived by the Laplace transform contains three virtual elements—a negative nonlinear capacitor in parallel with a negative nonlinear resistor, both in series with a positive nonlinear resistor. The negative *s*-domain capacitance gives rise to an apparent inductive response, similar to the memristive models of potassium and sodium ion channels (Chua et al., 2012). We found that an isolated Mott memristor near a fixed point dwells either in the locally passive (LP) or the EOC region. The EOC region coincides with the NDR region in its steady state or DC I–V locus. Brown et al. (2022b) explained that for an extended electro-thermal memristor, the coincidence between NDR and EOC or LA regions is not guaranteed. Therefore, NDR shall not be used as a sole signature for EOC. In our case, the crossover between the LP and EOC regions also manifests itself in the small-signal frequency response, which shows a sign reversal in the real part of the impedance (complexity) function $\text{Re}Z(s; Q)$, as predicted by the fourth LA criterion. In the frequency domain, an isolated Mott memristor is equivalent to a positive inductor in series with a resistor that is positive in the LP region and negative in the EOC domain. We derived the parametric Nyquist plot of the LP ↔

EOC crossover at a single current level and then extended it to a 2D color-scale map of $\text{Re}Z(s; Q)$ to visualize the LP and EOC regions in the parameter space spanned by frequency and current, which is effectively a phase diagram for complexity. We also examined the scaling trend of the EOC region versus the device size, which shows that the VO₂ conduction channel radius is the relevant dimension for device miniaturization to enhance the EOC frequency regime.

Although an EOC region exists in an isolated 1D Mott memristor, the topological constraint limits the dynamics it can possess, making it impossible to exhibit persistent oscillations. In Sections 5–6, we remove the topological constraint for an isolated 1D Mott memristor by coupling it with one or more reactive elements, increasing the system's dimensionality and dynamical complexity. For simplicity, we choose a DC voltage (V_{dc})-biased Pearson–Anson relaxation oscillator, formed using a Mott memristor coupled with a parallel capacitor C_p and a series resistor R_s , as an example of a 2D nonlinear system for our analysis (Pearson and Anson, 1921). The same analysis procedure can be applied to higher-dimensional systems, such as spiking neuron circuits consisting of two or more Mott memristors coupled with passive and reactive elements.

In Section 5 we first apply Chua's LA criteria and local linearization techniques to this example system, including the element combination approach, the Jacobian matrix method, and the trace-determinant plane classification to study the stability and qualitative behaviors of its hyperbolic fixed points. The element combination approach considers a Mott memristor in parallel with a capacitor to be a composite second-order nonlinear element. The small-signal transfer function of the element-combined system has a pair of complex conjugate or real poles. We derived the Nyquist plot and a 2D phase diagram of the system's poles. The pole phase diagram, combined with Chua's LA criteria, allows a visualization of the LP, EOC and locally active and unstable (LA\EOC) regions in the circuit parameter space. These results are corroborated by the trace-determinant plane analysis of the Jacobian linearized 2D system, which reveals a stability-change bifurcation as the parametric (trace and determinant) locus crosses the zero-trace axis as one of the three circuit parameters is varied (R_s , C_p , and V_{dc}). However, analyzing the stability behavior of a non-hyperbolic center requires additional theoretical tools since the Hartman–Grobman theorem is not applicable due to the loss of hyperbolicity (Hartman, 1960; Grobman, 1959).

Finally, in Section 6 we apply several global methods, such as the nullclines and numerical phase portrait analyses to understand qualitative behaviors of the non-hyperbolic centers in this example 2D nonlinear system. We found that each of the three circuit parameters (R_s , C_p , and V_{dc}) acts as a bifurcation parameter that switches the stability of a fixed point as the parametric (trace and determinant) locus crosses a center. We verified that there exists a supercritical 2D Hopf-like bifurcation, i.e., the creation of a stable limit cycle encircling an unstable spiral as the fixed point switches its stability from stable to unstable. We also noticed that the limit cycle emerges abruptly over an extremely narrow bifurcation parameter interval, a phenomenon known as “canard explosion” in relaxation oscillations within chemical and biological systems (Krupa and Szmolyan, 2001; Rotstein et al., 2012). This is a prominent distinction from the classical Hopf bifurcation, which predicts a gradual growth proportional to the square root of the

bifurcation parameter. Each bifurcation parameter has different bifurcation growth characteristics. We conclude the section with a comparison between the experimental limit cycle characteristics of a VO₂ relaxation oscillator and SPICE simulations based on the Mott memristor model, showing excellent agreements between them.

We conclude the manuscript with brief remarks on the application implications of locally active memristors and scalable neuromorphic dynamic neurons with a high degree of complexity.

2 One-dimensional locally active Mott memristor

2.1 Physics-based analytical compact model

The physics-based compact model for a 1D (one state variable) locally active Mott memristor is biphasic in nature (Pickett and Williams, 2012). It assumes that once an IMT is triggered by Joule self-heating beyond a threshold level, metallic and insulating phases coexist in a constant volume conduction channel defined by the top and bottom electrodes. For mathematical simplification, the conduction channel has an axial symmetry with a constant radius r_{ch} along its length. An experimental crossbar device may have a square or rectangular cross section defined by its top and bottom electrodes. The insulating phase has significantly lower thermal and electrical conductivity than the metallic phase. Therefore, the core region turns metallic first, and its radius r_{met} increases as Joule heating increases. In analogy to the case of an ice–water mixture, the maximum temperature within the metallic core is capped to the transition temperature T_c until the whole conduction channel turns metallic. The minimum temperature at the outer edge of the insulator shell is fixed at the ambient temperature T_0 . The temperature rise required for IMT to occur is defined as $\Delta T = T_c - T_0$. With these assumptions, a radial temperature profile bounded between T_0 and T_c is established across the insulating shell surrounding the metallic core. The schematic representation of this biphasic thermal model is shown in Figure 2.

The state variable $x \triangleq r_{met}/r_{ch}$ is modeled as the dimensionless volumetric fraction of the metallic phase in the conduction channel and is bounded between 0 and 1. The model derives that the temperature at a specific radius $T(r)$ is a nonlinear function of x of the form $T(r) = T_0 + \Delta T \ln(\frac{r}{r_{ch}})/\ln(x)$, where $r_{met} \leq r \leq r_{ch}$.

Another assumption the model makes for mathematical simplification is to ignore the axial heat exchanges with the electrodes and the associated temperature gradients near the top and bottom interfaces. Moreover, the thermal and electrical conductivity of the insulating shell are approximated as constants, regardless of the radial temperature gradient across it. This approximation holds true if neither of them varies significantly as temperature increases from T_0 to T_c . This is probably the case for VO₂ with a small ΔT ($T_c \approx 340$ K and $\Delta T \approx 43$ K) (Berglund and Guggenheim, 1969) but becomes questionable for NbO₂ with a very large ΔT ($T_c \approx 1080$ K and $\Delta T \approx 784$ K) (Janninck and Whitmore, 1966).

The compact model consists of two coupled equations that satisfy the definition of a 1D extended memristor (Chua, 2014): a state-dependent instantaneous relationship between voltage and current in the form of Ohm's law (state-dependent Ohm's law) and a

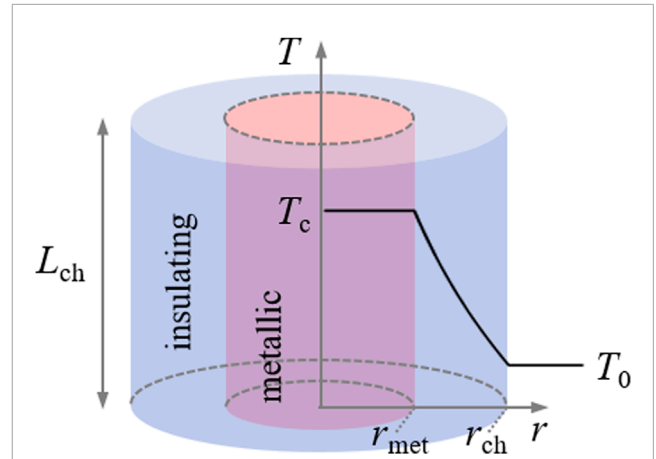


FIGURE 2 Schematic representation of the biphasic thermal model for a Mott memristor that undergoes an insulator-to-metal transition, illustrating a cylindrical conduction channel with a metallic-phase core surrounded by an insulating-phase shell. The model assumes that the metallic core is fixed at the transition temperature T_c , and the outer edge of the conduction channel is fixed at the ambient temperature T_0 . The black solid line shows a calculated radial temperature profile. The top and bottom electrodes are not shown for clarity.

first-order ordinary differential equation (ODE) that determines the dynamics of the single state variable x (state equation). The kinetic function that accounts for the state dynamics is a function of both the state variable x and the input variable (voltage v or current i). A Mott memristor, therefore, is a dynamical system—a system whose state at a future time depends deterministically on its present state and a physical law that governs its evolution over time.

Since Joule self-heating depends on the passage of current, a Mott memristor is a current-controlled memristor, and current i instead of voltage v is the appropriate input variable. The model equations take the following form:

$$v(x, i) = R_{ch}(x) i, \quad (1)$$

$$\frac{dx}{dt} \triangleq f_x(x, i) = \frac{i^2 R_{ch}(x) - \Gamma_{th}(x) \Delta T}{H'(x)}. \quad (2)$$

The single state variable $x \in (0, 1)$ is a dimensionless quantity within the bounded open interval between 0 and 1. $f_x(x, i)$ is the kinetic function of the state variable x . The derivation of $f_x(x, i)$ is nontrivial and is the main task of building the compact model. For Mott memristors and, more generally, electro-thermal memristors, $f_x(x, i)$ is derived from the first law of thermodynamics, which states that the change in the total enthalpy of a system ΔH equals the net heat flow q_p into it at constant pressure: $\Delta H = q_p$. Therefore, their time derivatives are also equal: $\frac{d\Delta H}{dt} = \frac{dq_p}{dt}$. This basic law forms the theoretical basis to interpret electro-thermal memristors, wherein the local temperature change plays a key role. It is worth pointing out that since there is no explicit dependence on time t in $f_x(x, i)$, this is an *autonomous* system.

To simplify the expression of $f_x(x, i)$, three nonlinear auxiliary functions are defined, namely, the state-dependent memristance function $R_{ch}(x)$ (Equation 3), the state-dependent thermal conductance function $\Gamma_{th}(x)$ (Equation 4), and $H'(x) \triangleq \frac{d\Delta H}{dx}$

TABLE 1 Material properties and device parameters of a VO₂ Mott memristor model.

Model property	Symbol	Value	Unit	Reference
Volumetric heat capacity	c_p	3.30×10^6	$\text{Jm}^{-3}\text{K}^{-1}$	Oh et al. (2010)
Volumetric enthalpy change in IMT	Δh_{tr}	2.35×10^8	Jm^{-3}	Berglund and Guggenheim (1969)
Thermal conductivity of the insulating phase	κ	3.5	$\text{Wm}^{-1}\text{K}^{-1}$	Oh et al. (2010)
Electrical resistivity of the metallic phase	ρ_{met}	3.00×10^{-6}	Ωm	Oh et al. (2010); Berglund and Guggenheim (1969)
Electrical resistivity of the insulating phase	ρ_{ins}	1.00×10^{-2}	Ωm	Berglund and Guggenheim (1969)
Temperature increase in IMT	ΔT	43	K	Berglund and Guggenheim (1969)
Radius of the conduction channel	r_{ch}	3.60×10^{-8}	m	Experimental
Length of the conduction channel	L_{ch}	5.00×10^{-8}	m	Experimental

(Equation 5), which is defined as the derivative of the total enthalpy change ΔH with regard to the state variable x .

$$R_{ch}(x) = \frac{1}{A(1+Bx^2)}, \quad (3)$$

$$\Gamma_{th}(x)\Delta T = -\frac{C}{\ln x}, \quad (4)$$

$$H'(x) \triangleq \frac{d\Delta H}{dx} = D \left(\frac{1-x^2+2x^2 \ln x}{2x(\ln x)^2} + Ex \right), \quad (5)$$

where $A = \frac{\pi r_{ch}^2}{\rho_{ins} L_{ch}}$, $B = \frac{\rho_{ins}}{\rho_{met}} - 1$, $C = 2\pi L_{ch} \kappa \Delta T$, $D = \pi L_{ch} r_{ch}^2 c_p \Delta T$, and $E = \frac{2\Delta h_{tr}}{c_p \Delta T}$ are constant coefficients whose values are determined by physical model parameters, including material properties and device geometry. Table 1 lists the values of these physical model parameters for the case of VO₂ material. The radius and length of the memristor conduction channel are device-dependent parameters and can be determined experimentally by the device geometry. The remaining model parameters listed in Table 1 are electronic, thermal, and phase transition properties of VO₂ material reported in the literature (Oh et al., 2010; Berglund and Guggenheim, 1969). These material property-dependent parameters can be optimized using a calibration procedure with well-devised characterization of VO₂ devices and least-square data fitting (Brown et al., 2022a), but this is beyond the scope of this work.

Table 2 lists the values of model coefficients A , B , C , D , and E for three arbitrarily chosen VO₂ device sizes, including the radius r_{ch} and length L_{ch} of the conduction channel. Coefficients B and E are dimensionless and device size-independent. Without loss of generality, these three device sizes are used throughout this manuscript to illustrate the scaling trend of a calculated quantity as the device size varies. If not mentioned explicitly, hereafter, the modeled VO₂ device is the medium-sized one in Table 2 with $r_{ch} = 36$ nm and $L_{ch} = 50$ nm, and is referred to as the *midsize* VO₂ Mott memristor or *midsize* VO₂ device.

A more general approach to the physical modeling of an electrothermal memristor considers the internal temperature the sole state variable (Brown et al., 2022b). The kinetic function is derived from Newton's law of cooling, which establishes a connection between the net heating power and a time-varying device's internal

temperature through a temperature-dependent thermal capacitance. There is clearly a benefit of adopting a universal state variable and a generalized formula of the kinetic function, albeit the temperature dependence of thermal capacitance is unknown and requires a model fitting with experimental characterization, such as the temperature dependence of self-excited oscillation frequency in a memristor-based relaxation oscillator (Brown et al., 2022a). It is interesting that both approaches can yield the same qualitative predictions regarding the system dynamics, despite differences in model assumptions, state variables, and kinetic functions.

2.2 Stability analyses

We start the stability analyses by focusing on an isolated or uncoupled Mott memristor. The first step is to examine the stability of solutions for Equation 2 by considering the input current to be a parameter with a zero or nonzero constant value and plotting the kinetic function $f_x(x, i)$ as a function of the state variable x . If a solution $f_x(x, i) = 0$ exists at a point x_Q , it is called a fixed point (Shashkin, 1991). This is because the state variable $x(t)$ with an initial condition $x(0) = x_Q$ remains unchanged at any future time, i.e., $x(t) = x_Q$ for $t > 0$. The literature from different disciplines has adopted a variety of terminologies for the same concept, including the stationary point, invariant point, equilibrium point, critical point, singular point, and steady-state point. These terms are generally interchangeable but may cause confusion if not carefully chosen. In particular, the use of the equilibrium point may cause misinterpretation by physical scientists for reasons we will elaborate below.

A system at equilibrium remains stable over time and does not require a net flow of energy or work to maintain that condition. A steady state also has stable internal conditions that remain unchanged over time. However, it requires a continuous energy input or work from the external environment to remain in a constant state. A memristor with stable internal states while a *finite* current flows through it is in a non-equilibrium steady state rather than equilibrium since there is a net heat transfer q_p into the memristor. In this manuscript, we mainly use the term fixed point because

TABLE 2 Values of model coefficients for three VO₂ device sizes.

Coefficient	Formula	Unit	$r_{ch} = 10 \text{ nm}$	$r_{ch} = 36 \text{ nm}$	$r_{ch} = 56 \text{ nm}$
			$L_{ch} = 10 \text{ nm}$	$L_{ch} = 50 \text{ nm}$	$L_{ch} = 100 \text{ nm}$
A	$\frac{\pi^2 r_{ch}^2}{\rho_{ms} L_{ch}}$	Mho	3.14159×10^{-6}	8.14301×10^{-6}	9.85203×10^{-6}
B	$\frac{\rho_{ins}}{\rho_{met}} - 1$	Unitless	3332.3	3332.3	3332.3
C	$2\pi L_{ch} \kappa \Delta T$	Watt	9.45619×10^{-6}	4.7281×10^{-5}	9.45619×10^{-5}
D	$\pi L_{ch} r_{ch}^2 c_p \Delta T$	Joule	4.45792×10^{-16}	2.88873×10^{-14}	1.398×10^{-13}
E	$\frac{2\Delta h_c}{c_p \Delta T}$	Unitless	3.31219	3.31219	3.31219

of its prevalence in mathematics. Steady state will also be used as a descriptive term when it facilitates interpretation. For example, steady-state resistance is a preferred term over fixed-point resistance.

For a current-controlled memristor, current is the appropriate input variable for stability analysis. However, one can still consider voltage v to be an input and run the same type of analysis. Interestingly, doing so would result in a bifurcation—a qualitative change in the solution of a nonlinear system incurred by a small change in a parameter, such as the creation or annihilation of fixed points or a change in their stability.

2.2.1 Power-off plot

The question of whether a memristor is non-volatile can be answered by examining the power-off plot (Chua, 2015). For a current-controlled memristor, its POP is the locus of the kinetic function $f_x(x, i)$ as a function of the state variable x at zero input current, i.e., the locus of $f_x(x, 0)$ vs x (Equation 6).

By setting the input current to 0 in Equation 2, we obtain

$$f_x(x, 0) = \frac{-\Gamma_{th}(x)\Delta T}{H'(x)} = \frac{2Cx \ln x}{D[1 - x^2 + 2x^2 \ln x + 2E(x \ln x)^2]} \quad (6)$$

If $f_x(x, 0)$ has an intersection with the x -axis, then the intersection is an equilibrium point x_Q . The memristor state $x(t)$ with an initial state $x(0) = x_Q$ remains unchanged at any future time, i.e., $x(t) = x_Q$ for any $t > 0$.

Figure 3 shows that for a Mott memristor at zero input current, $f_x(x, 0)$ remains negative for any state variable $x \in (0, 1)$. It is plausible since if there were a finite fraction of the conduction channel in the metallic phase at the beginning, it is unstable without the presence of Joule heating and will always vanish over time. The memory effect in a Mott memristor is, therefore, transient or volatile in nature and will be lost, given sufficient time after the removal of electrical power. Figure 3 inset shows that the negative rate of change in x increases dramatically as x approaches 1.0 asymptotically. The calculations are performed using VO₂ model parameters, but this conclusion is generally applicable to other Mott memristor materials.

2.2.2 Dynamic route map at constant input current

If input current is fixed at a finite constant level $i_0 \neq 0$, one can plot the dynamic route (DR)—the locus of the

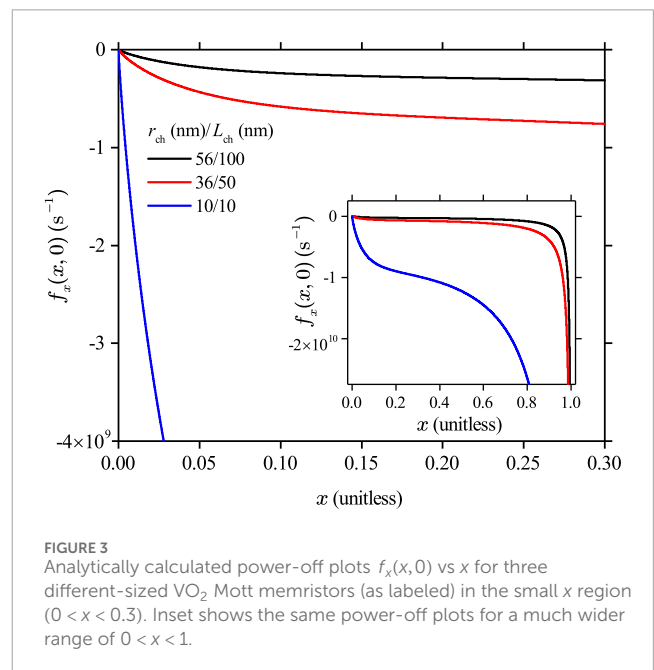


FIGURE 3 Analytically calculated power-off plots $f_x(x, 0)$ vs x for three different-sized VO₂ Mott memristors (as labeled) in the small x region ($0 < x < 0.3$). Inset shows the same power-off plots for a much wider range of $0 < x < 1$.

kinetic function $f_x(x, i_0)$ as a function of the state variable x at a constant input current i_0 (Chua, 1969). A set of dynamic routes parameterized by input current (or voltage for a voltage-controlled memristor) is called a dynamic route map (DRM) (Chua, 2018). Rewriting $f_x(x, i)$ in Equation 2 by replacing the auxiliary functions $R_{ch}(x)$, $\Gamma_{th}(x)$, and $H'(x)$ with their explicit expressions, we obtain

$$f_x(x, i_0) = \frac{\frac{2x(\ln x)^2}{A(1+Bx^2)} i_0^2 + 2Cx \ln x}{D[1 - x^2 + 2x^2 \ln x + 2E(x \ln x)^2]} \quad (7)$$

As shown in Figure 4A, even a tiny input current of a few μA creates a positive slope for the DR locus of the midsize VO₂ device, flipping the fourth-quadrant POP locus up into the first quadrant once a finite current is supplied. The slope of the DR then levels off and becomes negative again as x further increases. Consequently, a constant-current DR locus always intersects the x -axis at a single fixed point x_Q . This is confirmed by Figure 4B which shows the DRM loci over a much wider current range from 0 to 3 mA.

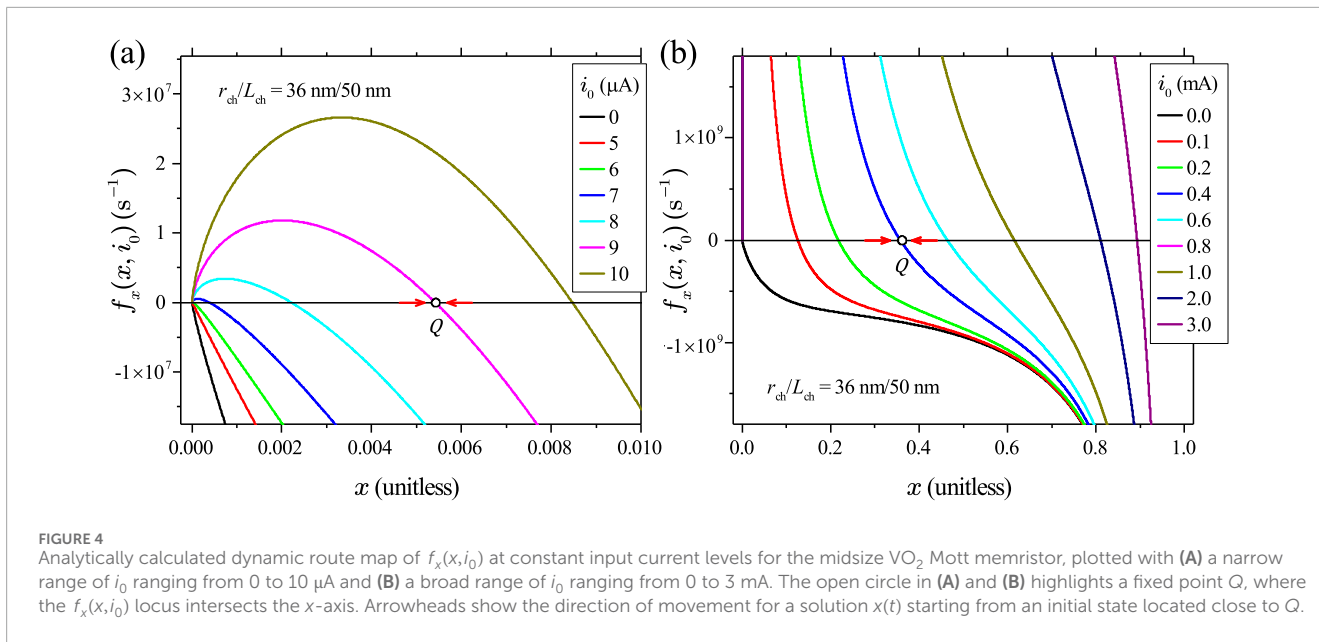


FIGURE 4 Analytically calculated dynamic route map of $f_x(x, i_0)$ at constant input current levels for the midsize VO₂ Mott memristor, plotted with (A) a narrow range of i_0 ranging from 0 to 10 μ A and (B) a broad range of i_0 ranging from 0 to 3 mA. The open circle in (A) and (B) highlights a fixed point Q , where the $f_x(x, i_0)$ locus intersects the x -axis. Arrowheads show the direction of movement for a solution $x(t)$ starting from an initial state located close to Q .

The theory of nonlinear dynamics indicates that the fixed point x_Q is *asymptotically stable* because the solution $x(t)$ starting from any initial state $x(0) \neq x_Q$ approaches the fixed point x_Q as $t \rightarrow \infty$. For $x < x_Q$, $dx/dt > 0$. For $x > x_Q$, $dx/dt < 0$. The arrowhead pointing to the right indicates that the solution $x(t)$ starting from any initial state $x(0) \neq x_Q$ on the DR above the x -axis must move to the right of $x(0)$ because $dx/dt > 0$ for $t > 0$, as long as $x(t)$ lies above the x -axis. Conversely, the arrowhead pointing to the left indicates that the solution $x(t)$ starting from any initial state $x(0) \neq x_Q$ below the x -axis on the DR must move to the left of $x(0)$ because $dx/dt < 0$ for $t > 0$, as long as $x(t)$ lies below the x -axis.

2.2.3 Dynamic route map at constant input voltage: saddle-node bifurcation

Although a Mott memristor is a current-controlled device, it is interesting to examine the state dynamics for the case where a constant finite input voltage is applied. Replacing current i by voltage v in Equation 2, the kinetic function can be rewritten as a function of x and v . At a constant input voltage v_0 , it takes the following form:

$$f_x(x, v_0) = \frac{1}{H'(x)} \left(\frac{v_0^2}{R_{ch}(x)} - \Gamma_{th}(x) \Delta T \right) = \frac{2Ax(\ln x)^2(1+Bx^2)v_0^2 + 2Cx \ln x}{D[1-x^2 + 2x^2 \ln x + 2E(x \ln x)^2]} \quad (8)$$

Figure 5A shows the DRM loci of $f_x(x, v_0)$ in Equation 8 vs x at constant v_0 levels, ranging from 0 to 1.2 V in 0.1 V intervals for the midsize VO₂ device. Figure 5B is a zoomed view, which reveals three behaviorally distinctive regions determined by the amplitude of v_0 . At a very small $v_0 < 0.0973$ V, the DR locus stays in the fourth quadrant and does not intersect with the x -axis. In other words, $f_x(x, v_0) < 0$ is satisfied at any $x \in (0, 1)$. It indicates that at such small input voltages, even if the initial condition is a metallic phase, a Mott memristor always returns to the insulating state after a

finite time. Physically speaking, the Joule heating level at such small voltages is too small to sustain a metallic filament at the IMT critical temperature against the heat loss. At $v_0 = 0.0973$ V, the DR locus becomes tangent to the x -axis with only one intersection point close to $x_0 = 0.606$. At a $v_0 > 0.0973$ V, the DR locus “swings” from the fourth quadrant to the first quadrant, and then, it swings back to the fourth quadrant, intersecting the x -axis at two distinctive points to the left and right of x_0 .

For a 1D nonlinear ODE system, a saddle-node (tangent) bifurcation is the generic bifurcation in which the number of fixed points changes as a parameter varies. If additional conditions are met, a transcritical or pitchfork bifurcation may occur. A simple example of a saddle-node bifurcation is $dx/dt = \mu \pm x^2$, where μ is the bifurcation parameter and the sign determines whether it is supercritical ($\mu - x^2$) or subcritical ($\mu + x^2$). For the supercritical case, as μ increases through $\mu_0 = 0$ (the bifurcation value), the number of fixed points changes from 0 to 1 and then to 2. If $\mu < \mu_0$, dx/dt is always negative and no fixed point exists. At $\mu = \mu_0$, there is one non-hyperbolic, semi-stable fixed point ($x = 0$). At $\mu > \mu_0$, a pair of stable ($x = \sqrt{\mu}$) and unstable ($x = -\sqrt{\mu}$) hyperbolic fixed points are created.

Figure 6 illustrates that if a VO₂ Mott memristor is biased by a constant voltage v_0 , a small change in v_0 , acting as the bifurcation parameter, results in a supercritical saddle-node bifurcation. For the midsize VO₂ device, the bifurcation value for v_0 is approximately 0.0973 V. Figure 6A shows the re-plots of the two DRM loci in Figure 5 at v_0 levels of 0.0973 V and 0.1 V. At $v_0 = 0.0973$ V, there is a single semi-stable fixed point $Q_0 (\times)$. Increasing the input voltage by a small amount to $v_0 = 0.1$ V results in a qualitative change in the solution structure and creates a pair of fixed points—the left one $Q_1 (\circ)$ is unstable and the right one $Q_2 (\bullet)$ is stable. The stability of a fixed point is told by the arrowheads, indicating the direction of move for a solution $x(t)$ starting from an initial state located close to it. Figure 6B shows the bifurcation diagram of the 1D saddle-node bifurcation with the input voltage as the bifurcation parameter.

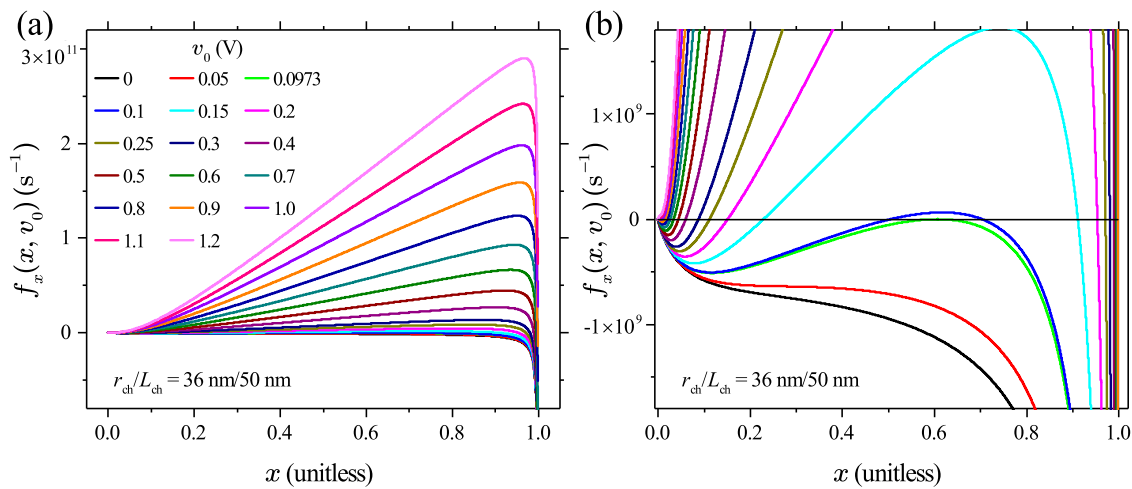


FIGURE 5 (A) Dynamic route map of $f_x(x, v_0)$ at constant input voltages in the range of 0–1.2 V, calculated for the midsize VO₂ Mott memristor. (B) Zoomed-in portion of (A) shows that at $v_0 > 0.0973$ V, the DR locus intersects the x -axis at two distinctive locations. At $v_0 = 0.0973$ V, the DR locus becomes tangent to the x -axis with only one intersection point. At $v_0 < 0.0973$ V, the DR locus stays in the fourth quadrant and does not intersect the x -axis.

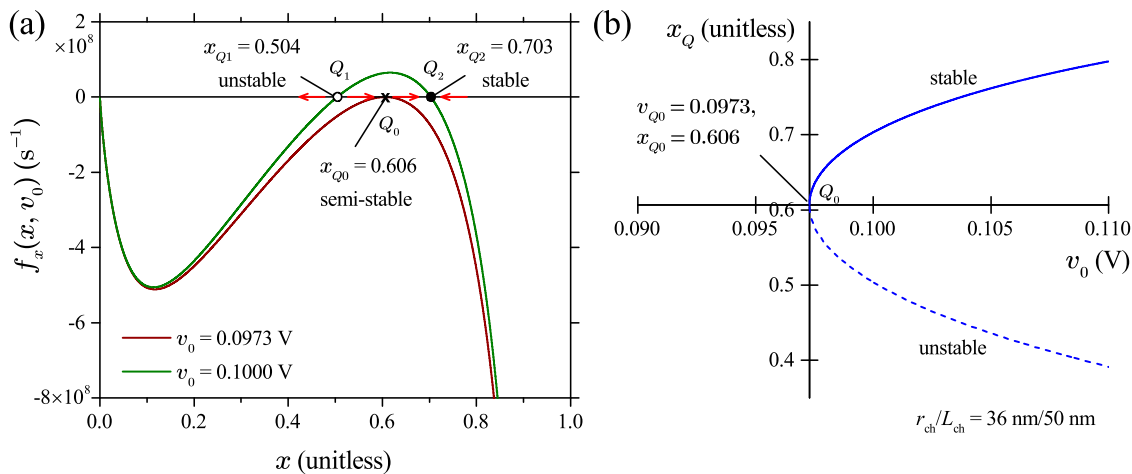


FIGURE 6 (A) Dynamic routes of $f_x(x, v_0)$ at constant input voltages of 0.0973 V and 0.1 V, calculated for the midsize VO₂ Mott memristor. At $v_0 = 0.0973$ V, the single intersection point Q_0 (\times) with the x -axis is a semi-stable fixed point. At $v_0 = 0.1$ V, the left intersection point Q_1 (\circ) with the x -axis is an unstable fixed point, and the right intersection point Q_2 (\bullet) with the x -axis is a stable fixed point. Arrowheads show the direction of movement for a solution $x(t)$ starting from an initial state located close to a fixed point. (B) Bifurcation diagram of the same device, showing a 1D supercritical saddle-node bifurcation with v_0 as the bifurcation parameter. The solid (dashed) line shows the stable (unstable) solutions of fixed points x_Q .

Solid and dashed lines show the stable and unstable solutions of fixed points x_Q , respectively.

3 Loci of steady states

In the present approach, the internal temperature is embedded in the biphasic model and is not considered a state variable. The set of all fixed points (x_Q, i_Q, v_Q) in the 3D (x, i, v) state space that satisfy the instantaneous relationship $v_Q = R_{ch}(x_Q)i_Q$ and $(dx/dt)|_Q = 0$ is defined as the steady-state or DC locus of a Mott memristor. Solving the steady-state locus of an isolated Mott memristor is among the

first steps for the local linearization analysis. Henceforth, both the (x_Q, i_Q, v_Q) locus and its 2D projections are called the steady-state loci without discerning the dimensional difference.

To obtain the steady-state (x_Q, i_Q, v_Q) locus, one can first define a sequence of $i_Q \in \mathbb{R}$ and then find the solutions of the state variable $x = x_Q(i_Q)$ numerically. This is achieved by setting the numerator in Equation 7 to be 0, which provides an equation $CA(1 + Bx_Q^2) = -i_Q^2 \ln x_Q$ that can be solved numerically. After solving $x_Q(i_Q)$, voltage v_Q can be calculated using the Ohm's law relationship $v_Q(i_Q) = R_{ch}(x_Q(i_Q))i_Q$.

However, there is a much easier way to obtain the steady-state (x_Q, i_Q, v_Q) locus. Instead of numerically solving the value of x_Q from

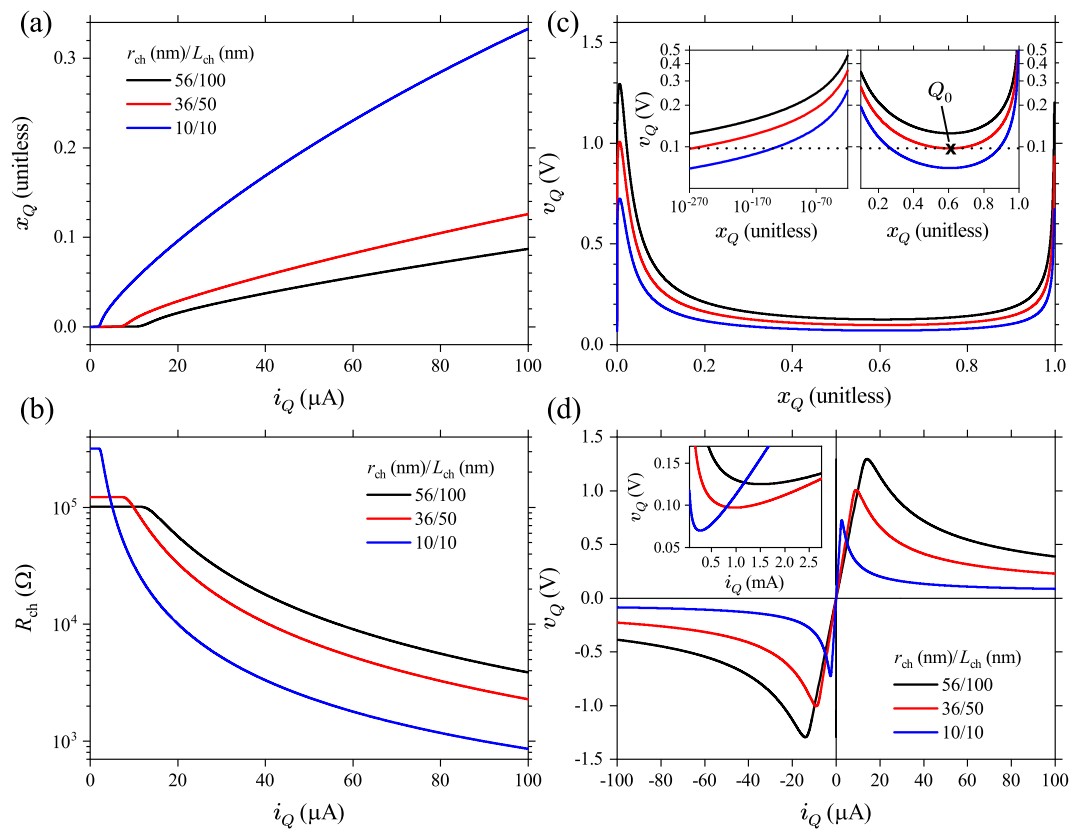


FIGURE 7

(A) Loci of the steady-state current $i_Q(x_Q)$ calculated using Equation 9 and transposed to $x_Q(i_Q)$ with current as the independent variable. (B) Loci of the memristance function $R_{ch}(x_Q)$ vs $i_Q(x_Q)$. (C) Loci of the steady-state voltage $v_Q(x_Q)$. Insets are the very small x_Q (left) and halfway regions (right). The dashed line represents $v_0 = 0.0973$ V. Q_0 (\times) is the semi-stable fixed point shown in Figure 6. (D) Loci of the steady-state (i_Q, v_Q) showing the zero-crossing property of memristors and a PDR-to-NDR crossover at $i_Q \geq 2.522$ μ A, 9.077 μ A, and 14.122 μ A, respectively, for the three VO₂ device sizes, as labeled. The inset reveals another NDR-to-PDR crossover at $i_Q \geq 269.77$ μ A, 971.18 μ A, and 1510.73 μ A, respectively, on the same three loci.

a given i_Q , one can first define a sequence of $x_Q \in (0, 1)$ and then calculate $i_Q(x_Q)$ analytically using the following formula:

$$i_Q(x_Q) = \sqrt{\frac{-CA(1 + Bx_Q^2)}{\ln x_Q}}. \quad (9)$$

Voltage v_Q is then calculated using the Ohm's law $v_Q(x_Q) = R_{ch}(x_Q)i_Q(x_Q)$. The sequence of x_Q can be chosen to be evenly spaced on a linear or logarithmic scale, depending on how fast these functions vary with x_Q . We verified that steady states calculated by both methods are consistent with each other. The analytical method is used for discussions hereafter.

Figure 7A shows the steady-state loci of (x_Q, i_Q) calculated using Equation 9 for three different VO₂ device sizes, plotted as $x_Q(i_Q)$, since Mott memristors are current-controlled devices. At small currents, the fraction of the metallic phase x_Q remains negligibly small. x_Q starts to increase with current in a sublinear fashion once i_Q exceeds a size-dependent threshold level. The current threshold increases with the device size and is at μ A level for the shown device sizes.

Figure 7B shows the loci of the memristance function $R_{ch}(x_Q)$ vs i_Q , which reveal that $R_{ch}(x_Q)$ has similar crossover characteristics at the same i_Q thresholds. At small currents, $R_{ch}(x_Q)$ remains

elevated with negligible current dependence. Once i_Q exceeds a size-dependent threshold, $R_{ch}(x_Q)$ decreases rapidly with current in a nonlinear fashion. For the midsize VO₂ device ($r_{ch} = 36$ nm and $L_{ch} = 50$ nm), $R_{ch}(x_Q)$ decreases by more than three orders of magnitude from 122.8 k Ω to 97 Ω as i_Q increases from 0 to 1 mA.

Figure 7C shows the steady-state loci of (x_Q, v_Q) plotted as $v_Q(x_Q)$, which resemble the shape of a left handed cup. The open left handle is nearly vertical. In other words, at very small x_Q levels, a tiny change in x_Q will cause a large change in v_Q . Figure 7C (left inset) shows the plots of the extremely small x_Q region of the (x_Q, v_Q) loci on a log-log scale, which reveals that at a given device size, there is a corresponding asymptotic lower bound of steady-state v_Q as x_Q approaches 0. For the midsize VO₂ device ($r_{ch} = 36$ nm and $L_{ch} = 50$ nm), the v_Q lower bound turns out to be 0.0973 V (dashed line). Figure 7C (right inset) shows the plot of the halfway x_Q region in linear scale, illustrating that the $v_Q = 0.0973$ V horizontal line is tangent to the (x_Q, v_Q) locus at its trough, located at $Q_0 = (0.60628, 0.0973$ V) (marked as \times); this corresponds to the same semi-stable fixed point Q_0 identified in the DR analysis. A slight increase in v_Q would bifurcate Q_0 into a pair of fixed points on its left and right. The left inset also indicates that in this case, another fixed point would emerge at an extremely small x_Q level (at $v_Q = 0.2$ V, x_Q is only 10^{-63}), i.e., an insulating steady state exists

at a finite voltage. These observations corroborate our previous DR analysis shown in Figure 6. All three (x_Q, v_Q) loci have a sharp peak at $x_Q = 0.00567$ and a rounded trough at $x_Q = 0.60628$, resembling the shape of a cup. Notably, the x_Q coordinates of these two extrema are size-independent.

Figure 7D shows the steady-state loci of (i_Q, v_Q) plotted as $v_Q(i_Q)$. As current-controlled memristors, the (i_Q, v_Q) loci are “N”-shaped when plotted with current as the x -axis. They are symmetric with respect to the origin in the first and third quadrants. Therefore, one only needs to analyze the first-quadrant halves. Each (i_Q, v_Q) locus has three distinctive regions: a lower positive differential resistance (PDR) region from 0 to a critical current i_{c1} ; an NDR region between i_{c1} and the second critical current i_{c2} (see inset); and an upper PDR region for even higher currents. Therefore, i_{c1} and i_{c2} produce a local maximum and minimum in the (i_Q, v_Q) loci. For the shown device sizes, values of i_{c1} (i_{c2}) are 2.522 μA (269.77 μA), 9.077 μA (971.18 μA), and 14.122 μA (1510.73 μA), respectively. Figure 7D also shows that the steady state or DC loci of (i_Q, v_Q) always pass through the origin (0, 0), satisfying the zero-crossing property of memristors.

It should be noted that the volumetric enthalpy change in IMT Δh_{tr} appears only in the denominator of the kinetic function $f_x(x, i)$ via the coefficient E . Therefore, it has no effect in determining the steady-state (i_Q, v_Q) loci. The main effect of IMT on the shape of steady-state (i_Q, v_Q) is applied via coefficient B —the coefficient of the quadratic nonlinearity in the memristance function. Coefficient B is approximately the electrical resistivity ratio $\frac{\rho_{ins}}{\rho_{met}}$ between the insulating and metallic phases.

The sets of loci plotted in Figures 7A, C, D are 2D projections of the steady-state loci (x_Q, i_Q, v_Q) in the 3D state space. Figure 8 shows the locus of (x_Q, i_Q, v_Q) calculated for the midsize VO_2 device ($r_{ch} = 36$ nm and $L_{ch} = 50$ nm). It resembles a twisted handle of a binder clip. The two open legs of the clip are rotated out of the plane defined by the looped clip head. Figure 9 provides a zoomed-in view of Figure 8 to visualize the low-current region of the same (x_Q, i_Q, v_Q) locus, allowing its 2D projections onto the (i, x) , (v, x) , and (i, v) planes to be directly compared with the loci shown in Figures 7A, C, D, respectively.

4 Local analysis of an isolated Mott memristor

4.1 Linearization and small-signal analysis

Chua’s LA theory outlines an algorithmic analysis procedure on nonlinear dynamical electronic circuits using equivalent linearized circuits (Chua, 2005). The linearized LA analysis examines the locus of fixed points of the composite circuit, the fluctuations around these fixed points, and their Laplace transforms. To explore the complex phenomena of nonlinear dynamical circuits, one can simply apply the LA criteria to access the locally active parameter domain rather than applying a time-consuming trial-and-error search in the parameter space. A good illustration of this procedure is the memristive HH axon circuit model (Chua et al., 2012). In this study, we apply the local linearization analysis and the LA theory to an isolated VO_2 Mott memristor to gain insights into its behavior near fixed points.

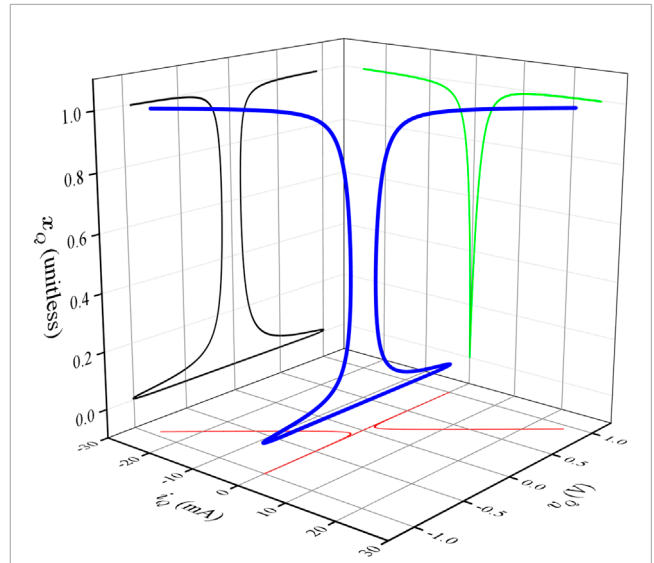


FIGURE 8 Locus of fixed points (x_Q, i_Q, v_Q) in the 3D state space of (x, i, v) calculated for the midsize VO_2 Mott memristor (blue line) and its 2D projections (green, black, and red lines).

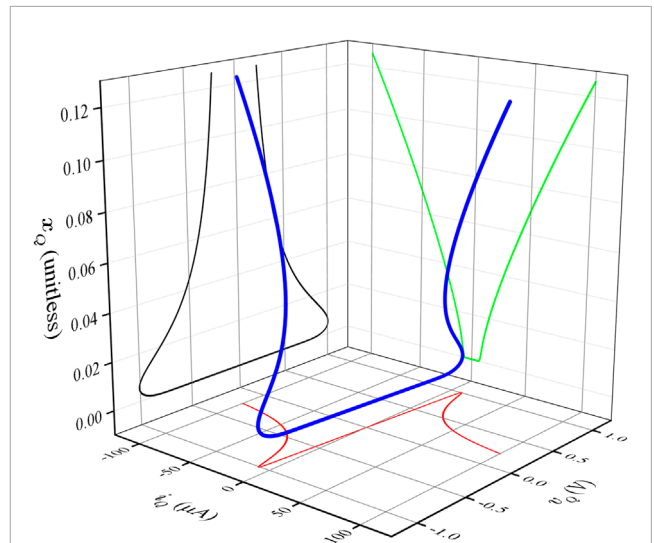


FIGURE 9 Zoomed-in view of Figure 8 to visualize the low-current region of the fixed-point locus (x_Q, i_Q, v_Q) calculated for the midsize VO_2 Mott memristor. Its 2D projections (green, black, and red lines) can be compared with the loci $i_Q(x_Q)$, $v_Q(x_Q)$, and (i_Q, v_Q) shown in Figure 7.

4.1.1 Linearization around a fixed point

Considering a fixed point Q with a coordinate (x_Q, i_Q) on the steady-state locus of an isolated Mott memristor, one can expand voltage v at the fixed point (x_Q, i_Q) in a Taylor series:

$$v(x_Q + \delta x, i_Q + \delta i) = v_Q + i_Q R'_{ch}(x_Q) \delta x + R_{ch}(x_Q) \delta i + \text{h.o.t.}, \quad (10)$$

where $R'_{ch}(x_Q) \triangleq \frac{dR_{ch}}{dx}|_Q$ and h.o.t. denotes higher-order terms in δx and δi . Neglecting h.o.t., in Equation 10 we obtain a linear

equation as follows:

$$\delta v = i_Q R'_{\text{ch}}(x_Q) \delta x + R_{\text{ch}}(x_Q) \delta i = a_{11}(Q) \delta x + a_{12}(Q) \delta i, \quad (11)$$

where coefficients $a_{11}(Q) \triangleq i_Q R'_{\text{ch}}(x_Q)$ and $a_{12}(Q) \triangleq R_{\text{ch}}(x_Q)$. Similarly, the kinetic function $f_x(x, i)$ can be expanded at the fixed point (x_Q, i_Q) in a Taylor series as follows:

$$f_x(x_Q + \delta x, i_Q + \delta i) = f_x(x_Q, i_Q) + \frac{\partial f_x(x, i)}{\partial x} \Big|_Q \delta x + \frac{\partial f_x(x, i)}{\partial i} \Big|_Q \delta i + \text{h.o.t.} \quad (12)$$

Note that $f_x(x_Q, i_Q) = 0$ since it is a fixed point (x_Q, i_Q) on the steady-state locus. Neglecting h.o.t., in Equation 12 we can recast the nonlinear state equation $\frac{dx}{dt} = f_x(x, i)$ into the following linear differential equation:

$$\frac{d}{dt}(\delta x) = \frac{\partial f_x(x, i)}{\partial x} \Big|_Q \delta x + \frac{\partial f_x(x, i)}{\partial i} \Big|_Q \delta i = b_{11}(Q) \delta x + b_{12}(Q) \delta i, \quad (13)$$

where coefficients $b_{11}(Q) \triangleq \frac{\partial f_x(x, i)}{\partial x} \Big|_Q$ and $b_{12}(Q) \triangleq \frac{\partial f_x(x, i)}{\partial i} \Big|_Q$. Applying Equations 2, 3, one can easily obtain the expressions for the following three linear-term coefficients:

$$a_{11}(Q) = -\frac{2Bi_Q x_Q}{A(1+Bx_Q^2)^2}, \quad (14)$$

$$a_{12}(Q) = R_{\text{ch}}(x_Q) = \frac{1}{A(1+Bx_Q^2)}, \quad (15)$$

$$b_{12}(Q) = \frac{4x_Q(\ln x_Q)^2 i_Q}{DA(1+Bx_Q^2)[1-x_Q^2+2x_Q^2 \ln x_Q+2E(x_Q \ln x_Q)^2]}. \quad (16)$$

To obtain the expression for $b_{11}(Q)$, we rewrite $f_x(x, i)$ as $f_x(x, i) = \frac{f^2 X(x)+Y(x)}{Z(x)}$, where the three auxiliary functions are defined as $X(x) = \frac{2x(\ln x)^2}{A(1+Bx^2)}$, $Y(x) = 2Cx \ln x$, and $Z(x) = D[1-x^2+2x^2 \ln x+2E(x \ln x)^2]$. Applying the quotient rule $\frac{d}{dx} \frac{X(x)}{Z(x)} = \frac{X'(x)Z(x)-X(x)Z'(x)}{Z(x)^2}$, we obtain

$$b_{11}(Q) = i_Q^2 \frac{X'(x)Z(x)-X(x)Z'(x)}{Z(x)^2} \Big|_Q + \frac{Y'(x)Z(x)-Y(x)Z'(x)}{Z(x)^2} \Big|_Q. \quad (17)$$

The formulas for $X'(x) \triangleq \frac{dX(x)}{dx}$, $Y'(x) \triangleq \frac{dY(x)}{dx}$, and $Z'(x) \triangleq \frac{dZ(x)}{dx}$ are $X'(x) = \frac{2 \ln x(2Bx^2-Bx^2 \ln x+\ln x+2)}{A(1+Bx^2)^2}$, $Y'(x) = 2C(\ln x+1)$, and $Z'(x) = 4Dx \ln x[1+E(\ln x+1)]$, respectively.

Figures 10A–D show the plot of the current dependence of the linear-term coefficients a_{11} , a_{12} , b_{11} , and b_{12} , calculated using Equations 14–17 for three different VO₂ device sizes. They show that coefficients a_{11} and b_{12} are odd functions of the driving current, while coefficients b_{11} and a_{12} are even functions of the driving current. a_{12} is the same as the memristance R_{ch} and is always positive. In contrast, b_{11} is always negative.

4.1.2 Complex-domain equivalent circuit

Many insights can be gained about an isolated Mott memristor through complex analysis. As the second step of the local analysis,

we can obtain its complex-domain equivalent circuit using the linear Laplace transform $\hat{f}(s) \triangleq \int_0^\infty f(t)e^{-st} dt$ that maps a function $f(t)$ in the time domain to a function $\hat{f}(s)$ in the complex domain \mathbb{C} , whose elements are complex frequencies $s = \sigma + i\omega$. The complex domain is also known as the s -domain. One direct benefit of the Laplace transform is that it converts a differential equation into an algebraic equation.

Taking the Laplace transforms of Equations 11, 13, we obtain

$$\hat{v}(s) = a_{11}(Q) \hat{x}(s) + a_{12}(Q) \hat{i}(s), \quad (18)$$

$$s\hat{x}(s) = b_{11}(Q) \hat{x}(s) + b_{12}(Q) \hat{i}(s), \quad (19)$$

where $\hat{x}(s)$, $\hat{v}(s)$, and $\hat{i}(s)$ denote the Laplace transforms of $\delta x(t)$, $\delta v(t)$, and $\delta i(t)$, respectively. Solving Equation 19 for $\hat{x}(s)$, we obtain

$$\hat{x}(s) = \frac{b_{12}(Q) \hat{i}(s)}{s - b_{11}(Q)}. \quad (20)$$

Substituting Equation 20 for $\hat{x}(s)$ in Equation 18 and solving for the impedance function $Z(s; Q) \triangleq \hat{v}(s)/\hat{i}(s)$, we obtain the s -domain impedance function as follows:

$$Z(s; Q) = \frac{a_{11}(Q)b_{12}(Q)}{s - b_{11}(Q)} + a_{12}(Q). \quad (21)$$

For a current-controlled memristor, the impedance function $Z(s; Q)$ in Equation 21 is the proper choice for its transfer function $H(s; Q)$. For a voltage-controlled memristor, admittance function $Y(s; Q)$ should be used. Chua pointed out that for a 1D system with just one-port state variable, its transfer function is also the scalar *complexity function* that forms the basis for the LA analysis (Chua, 2005). In Chua's original LA formulations for reaction-diffusion systems, a port state variable of a "reaction" cell (equivalent to a lumped circuit element) interacts with the neighboring cells via an energy or matter flow such as diffusion. On the other hand, a non-port state variable describes isolated internal dynamics and does not interact with other cells. The concept of LA is defined concerning only port state variables. Clearly, the state variable x in the Mott memristor model is a port state variable as it interacts with a coupled circuit element through the current (energy) flow.

Since the s -domain representation of a capacitor looks like a "resistance" $1/sC$, one can recast the small-signal impedance function $Z(s; Q)$ of a Mott memristor at a fixed point Q as an equivalent circuit that consists of three virtual elements: a capacitor C_1 in parallel with a resistor R_1 and both of them in series with a second resistor R_2 .

$$Z(s; Q) = \left(\frac{1}{sC_1} \right) R_1 + R_2, \quad (22)$$

where

$$R_1 \triangleq -\frac{a_{11}(Q)b_{12}(Q)}{b_{11}(Q)}, \quad (23)$$

$$R_2 \triangleq a_{12}(Q) = R_{\text{ch}}(x_Q), \quad (24)$$

$$C_1 \triangleq \frac{1}{a_{11}(Q)b_{12}(Q)}. \quad (25)$$

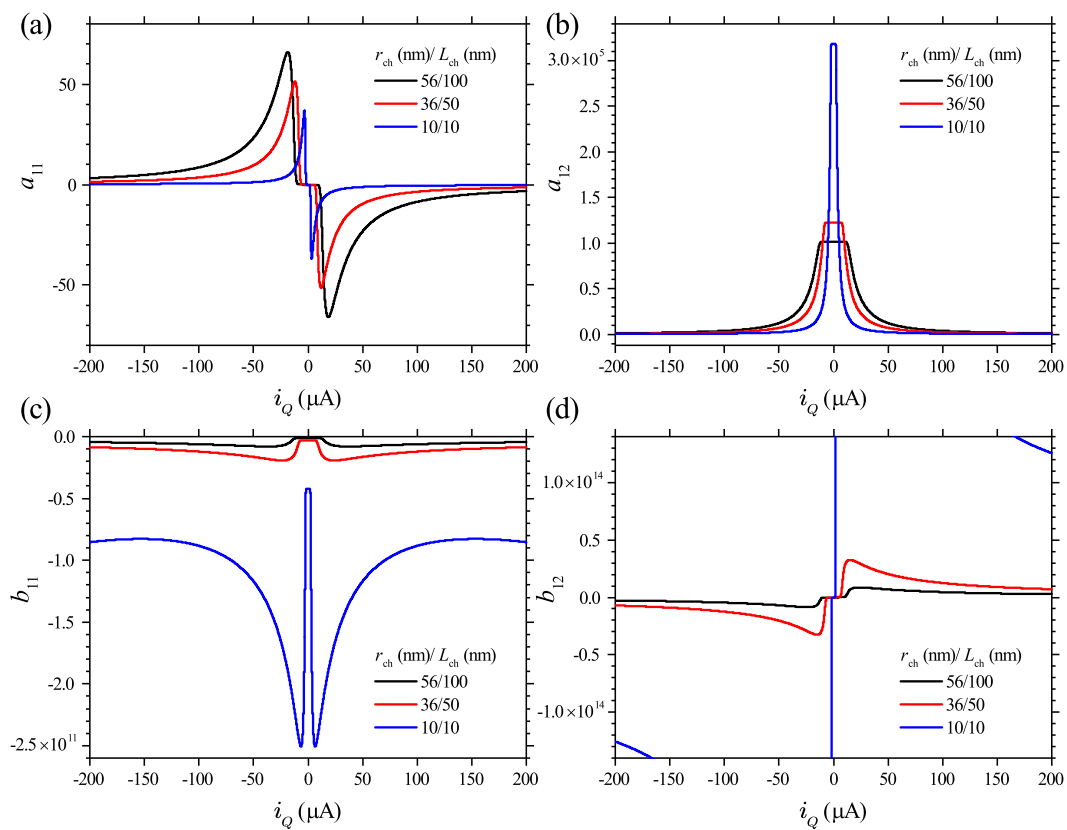


FIGURE 10 Current dependences of the linear-term coefficients (A) a_{11} , (B) a_{12} , (C) b_{11} , and (D) b_{12} in the linearized expressions of voltage v and the kinetic function $f_x(x, I)$ at a fixed point on the steady-state locus of three different-sized VO₂ Mott memristors, as labeled.

Figures 11A–C plot the current dependence of the three virtual circuit elements, namely, R_1 , R_2 , and C_1 , calculated using Equations 23–25, respectively, for three different VO₂ device sizes. They are all even functions of the driving current, so we only plot the positive x -axis halves. The first thing to notice is that R_1 and C_1 stay negative at any current for all three device sizes calculated. In contrast, R_2 remains positive at any current. Note that R_2 is the same as a_{12} and $R_{\text{ch}}(x_Q)$. Therefore, in the s -domain, a Mott memristor can be modeled as a nonlinear positive resistor in series with a composite reactive element consisting of a nonlinear negative capacitor and a nonlinear negative resistor placed in parallel. This small-signal equivalent circuit in the s -domain is shown in Figure 11B inset.

Since a negative capacitance value corresponds to a positive frequency-dependent inductive reactance, it indicates that a Mott memristor (or generally a current-controlled LAM) exhibits an apparent inductive reactance without involving a magnetic field. In physiology, an anomalous inductive reactance was observed as early as 1930s in voltage clamp measurements of the squid giant axon (Cole, 1941), but this perplexing phenomenon was not fully understood until Chua's memristive formulation for the potassium and sodium ion channels (Chua et al., 2012).

Figure 11D shows the plots of the current dependence for the sum of the two resistances ($R_1 + R_2$). At small currents, ($R_1 + R_2$) is positive and remains nearly constant. As the current increases, ($R_1 + R_2$) decreases abruptly and becomes negative once the current

exceeds a limit identical to the critical current i_{c1} for the lower PDR to NDR transition on the steady-state (i_Q, v_Q) loci (see Figure 7D) at 2.522 μA , 9.077 μA , and 14.122 μA , respectively, for the three device sizes. The negative ($R_1 + R_2$) then starts to increase with the current. Inset of Figure 11D shows that ($R_1 + R_2$) becomes positive again as the current exceeds a much larger limit identical to the critical current i_{c2} for the NDR to the upper PDR transition on the steady-state (i_Q, v_Q) loci (see Figure 7D inset) at 269.77 μA , 971.18 μA , and 1510.73 μA , respectively, for the same three devices. The one-to-one correspondence between the sign of ($R_1 + R_2$) and the sign of the slope on the steady-state (i_Q, v_Q) loci indicates that the three-element equivalent circuit shown in Figure 11B inset is the proper small-signal representation of a Mott memristor in the s -domain.

4.2 Pole–zero diagram and Chua's local activity theorem

4.2.1 Poles and zeros of the transfer function

For a dynamical system, the poles and zeros of its transfer function $H(s; Q)$ in the s -domain provide important insights into the system's response without requiring a complete solution of the differential equations. The first step of pole–zero analysis is to rewrite the s -domain small-signal transfer function $H(s; Q)$ as a rational function of s , i.e., a ratio of two polynomials. For the case of a

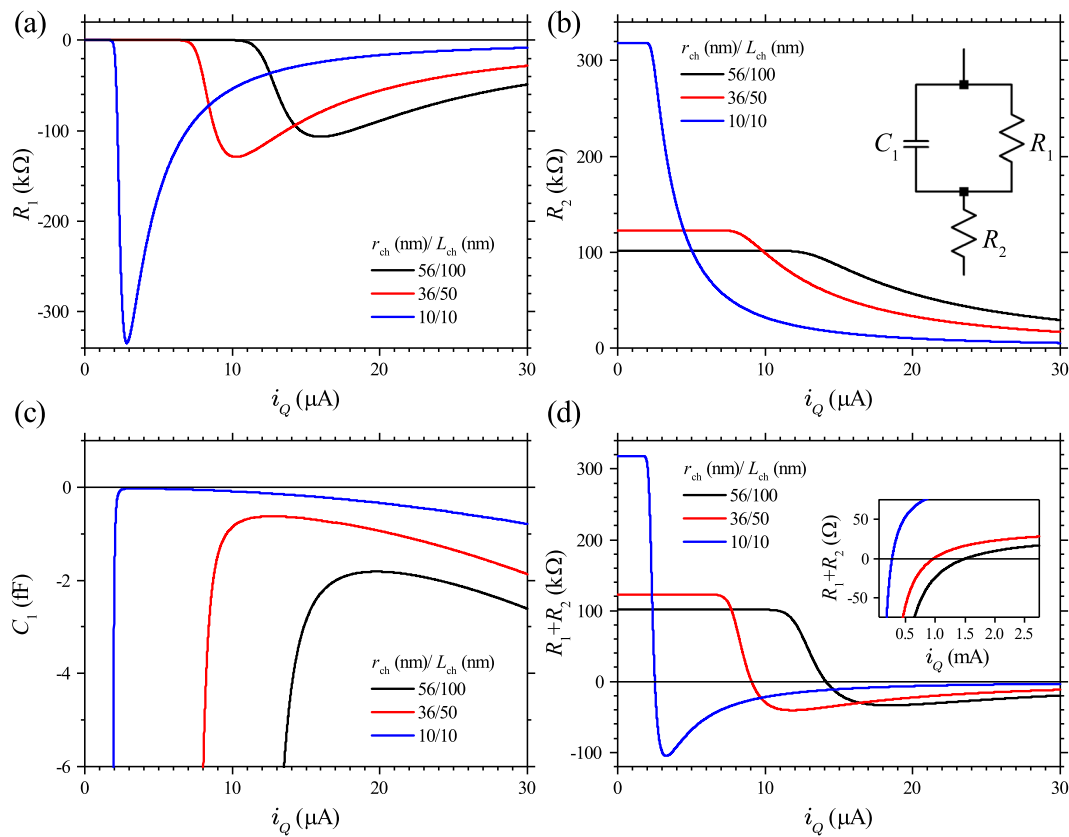


FIGURE 11

Current dependences of the three virtual circuit elements (A) R_1 , (B) R_2 , and (C) C_1 comprising the s -domain impedance function $Z(s; Q)$ at a fixed point on the steady-state (i_{Q, V_Q}) loci of three different-sized VO₂ Mott memristors, as labeled. R_1 and C_1 remain negative at any current for all three device sizes. (B) The inset shows the small-signal equivalent circuit in the s -domain. (D) Current dependence for the sum of the two resistances ($R_1 + R_2$). ($R_1 + R_2$) turns negative as the current exceeds a size-dependent limit. (D) The inset shows that ($R_1 + R_2$) becomes positive again when the current exceeds a much larger size-dependent limit. These two current limits are identical with the critical currents i_{c1} at the lower PDR to NDR and i_{c2} at the NDR to upper PDR transitions on the steady-state (i_{Q, V_Q}) loci, respectively (see Figure 7D and inset).

1D current-controlled Mott memristor, both the denominator and numerator s polynomials have a degree of $n = 1$. Therefore, its impedance function $Z(s; Q)$ is written as follows:

$$Z(s; Q) = \frac{b_1 s + b_0}{a_1 s + a_0}, \quad (26)$$

where all the coefficients of s polynomials in the denominator and numerator are real numbers. Using Equation 22, the expressions for these four coefficients are derived as follows:

$$a_0 = 1, \quad (27)$$

$$a_1 = R_1 C_1, \quad (28)$$

$$b_0 = R_1 + R_2, \quad (29)$$

$$b_1 = R_1 R_2 C_1. \quad (30)$$

Since a_0 is a constant and $b_0 = R_1 + R_2$ has already been discussed (see Figure 11D), we only need to examine $a_1 = R_1 C_1$ and $b_1 = R_1 R_2 C_1$. Both of them are even functions of the input current. Their

dependence on current is plotted in Figure 12 for three different VO₂ device sizes.

A rational transfer function can be further rewritten in a factored or pole-zero form by expressing the s polynomials in the denominator and numerator as products of linear factors. The roots of the denominator polynomial are the poles, and the roots of the numerator polynomials are the zeros. For any polynomial with real coefficients, its roots are either real or complex conjugate pairs.

For an isolated 1D Mott memristor, there is just one pole and one zero. To obtain the expressions for the zero and the pole of $Z(s; Q)$, Equation 26 is rewritten as follows:

$$Z(s; Q) = \frac{k(s - z)}{(s - p)}, \quad (31)$$

where $k = b_1/a_1 = R_2$ is a positive real coefficient and z and p denote, respectively, the zero and the pole of $Z(s; Q)$. The expressions for z and p are as follows:

$$z = -\frac{b_0}{b_1} = -\frac{R_1 + R_2}{R_1 R_2 C_1}, \quad (32)$$

$$p = -\frac{a_0}{a_1} = -\frac{1}{R_1 C_1} = b_{11}. \quad (33)$$

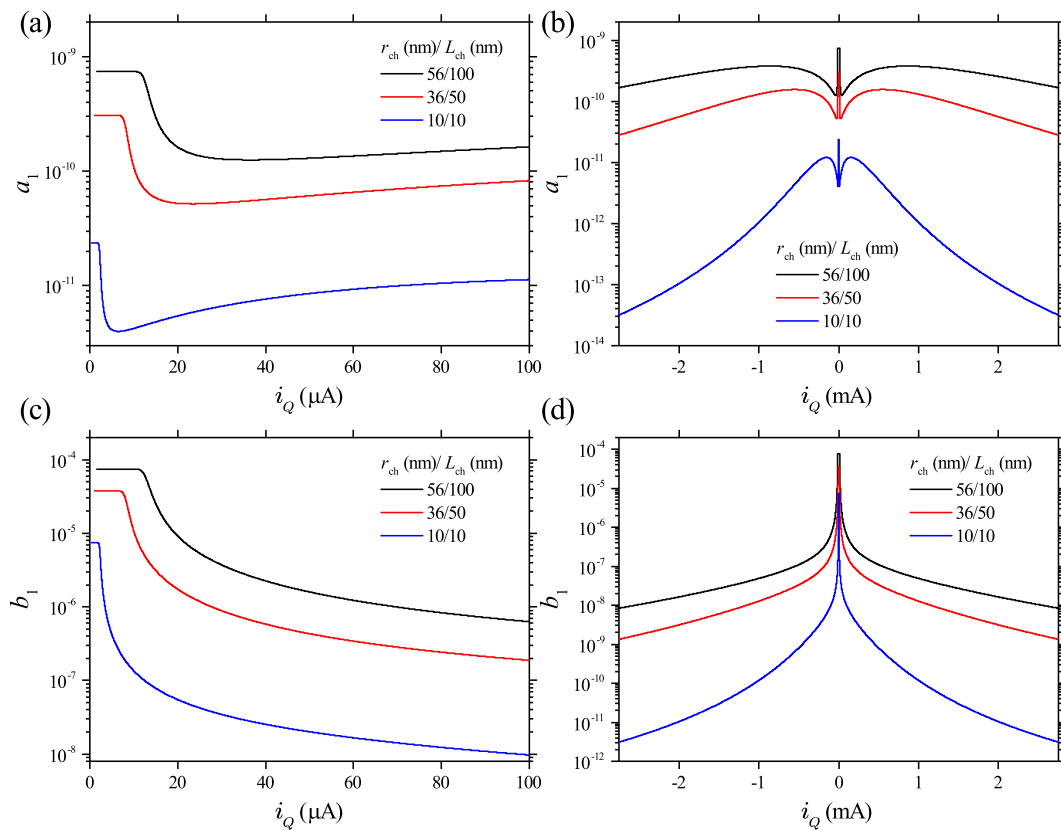


FIGURE 12

Current dependences for two of the four s -polynomial coefficients: (A) a_1 (low-current part), (B) a_1 (wide range), (C) b_1 (low-current part), and (D) b_1 (wide range) in the rational function representation of the impedance function $Z(s; Q)$ at a fixed point on the steady-state (i_Q, v_Q) locus of three different-sized VO₂ Mott memristors, as labeled. The other two coefficients are $a_0 = 1$ and $b_0 = R_1 + R_2$ (see Figure 11D).

Figure 13 show the loci of the zero z and the pole p versus input current for three different VO₂ device sizes calculated using Equations 32, 33. It is conspicuous that both z and p are located on the real axis in the complex plane, and both are even functions of current. It may be noted that p is already plotted in Figure 10C in the form of b_{11} . It is replotted in Figure 13B for a side-by-side comparison with z .

Since both the zero and the pole of $Z(s; Q)$ are located on the real axis, their signs can be examined to determine the local dynamical behaviors at a fixed point, as discussed in the next subsection. Generally speaking, for a 1D uncoupled Mott memristor, its pole p (or b_{11}) remains negative at any current level. In contrast, its zero z has two sign reversals at two distinctive input current levels. These characteristics are illustrated in Figure 14, which shows the current dependence of p and z of $Z(s; Q)$ calculated for the midsize VO₂ device ($r_{\text{ch}} = 36$ nm and $L_{\text{ch}} = 50$ nm).

Figures 14A, B show the loci of $p(i_Q)$ for the low-current part (up to 100 μA) and the broader range (up to 2 mA), respectively. p exhibits a non-monotonic dependence on current, but the condition $p < 0$ always holds true. Figure 14C shows that z is initially negative at small currents, and then, it turns positive when the current is higher than ≈ 9.077 μA , as indicated by a pair of nearby fixed points $\{Q_1, Q_2\}$ across zero. Their coordinates $[x_Q, i_Q, v_Q, \text{Re}(z)]$ are $[0.00566, 9.075 \mu\text{A}, 1.007 \text{ V}, -5.882 \times 10^6]$

for Q_1 and $[0.00567, 9.078 \mu\text{A}, 1.007 \text{ V}, 3.388 \times 10^6]$ for Q_2 , respectively. Figure 14D shows that z becomes negative again if the current exceeds ≈ 971.18 μA , as indicated by a pair of nearby fixed points $\{Q_3, Q_4\}$ across zero. Their coordinates are $[0.60628, 971.171 \mu\text{A}, 0.097 \text{ V}, 3.854 \times 10^4]$ for Q_3 and $[0.60629, 971.203 \mu\text{A}, 0.097 \text{ V}, -8.477 \times 10^4]$ for Q_4 , respectively. The two critical currents corresponding to sign reversals in z match exactly with those that delineate the NDR region from the lower and upper PDR regions on the steady-state (i_Q, v_Q) locus of the same device, as shown in Figures 14E, F. The coincidences are confirmed by examining the locations of the same two pairs of nearby fixed points $\{Q_1, Q_2\}$ and $\{Q_3, Q_4\}$ on the (i_Q, v_Q) locus.

4.2.2 Chua's local activity theorem

Chua's local analysis method established a practical set of criteria to classify the dynamics of an isolated or uncoupled nonlinear circuit element around its fixed points. To determine whether a linearized element is LP or locally active around a fixed point $Q = (x_Q, i_Q, v_Q)$, one must find out whether small input fluctuations lead to dissipating output fluctuations over time or, conversely, result in amplification. For the discussion, we choose the example of a 1D current-controlled memristor with current as the input and voltage as the output. Their roles are exchanged for a voltage-controlled memristor by duality. Mathematically,

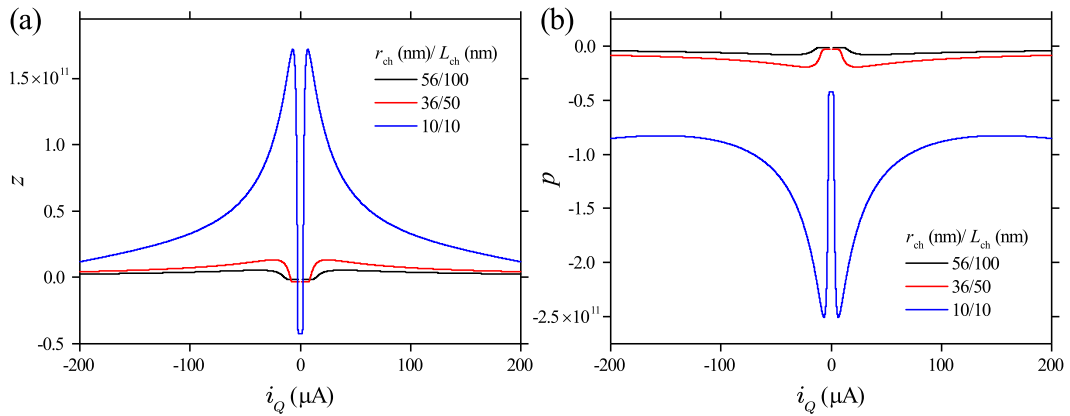


FIGURE 13 Current dependence of **(A)** the zero z and **(B)** the pole p of the s -domain impedance function $Z(s; Q)$ at a fixed point on the steady-state (i_Q, v_Q) locus of a VO₂ Mott memristor, calculated for three different device sizes as labeled.

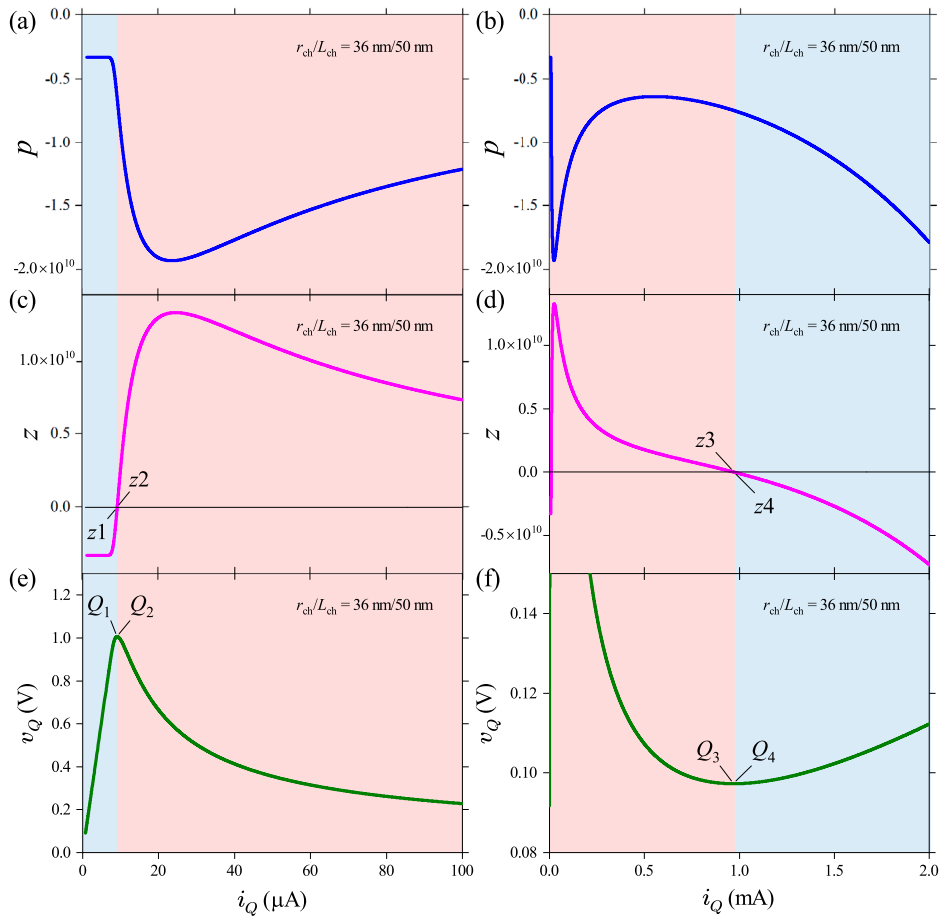


FIGURE 14 Current dependence of the pole p of $Z(s; Q)$ in **(A, B)** and the zero z in **(C, D)** for the midsize VO₂ Mott memristor. p remains negative at any current. For z , **(C)** $(-)$ \rightarrow $(+)$ sign reversal is observed at 9.077 μA , as indicated by a pair of nearby zeros $\{z_1, z_2\}$ with the opposite sign; **(D)** $(+)$ \rightarrow $(-)$ sign reversal is observed at 971.18 μA , as indicated by a pair of nearby zeros $\{z_3, z_4\}$ with the opposite sign. **(E, F)** Corresponding parts of the steady-state (i_Q, v_Q) locus of the same device. The crossovers between the NDR region (red) and the lower and upper PDR regions (blue) at the local voltage extrema coincide with the sign reversals in z , as indicated by the locations of $\{Q_1, Q_2\}$ and $\{Q_3, Q_4\}$ pairs of fixed points on the (i_Q, v_Q) locus.

with a homogeneous initial condition $(\delta x(0), \delta i(0), \delta v(0)) = \mathbf{0}$ (no fluctuation at $t = 0$), a linearized element is LP if and only if (iff) the fluctuation energy integrated over time remains positive:

$$\text{LP} \Leftrightarrow \int_0^{t'} \delta \mathbf{i}(t) \cdot \delta \mathbf{v}(t) dt \geq 0, \quad (34)$$

for any finite time interval $t' > 0$. The uncoupled element is locally active at a fixed point Q iff there exists an input fluctuation $\delta i(t)$ and a finite time $0 < T < \infty$ such that the integrated fluctuation energy becomes *negative*. For a multidimensional element, the fluctuation power to be integrated is a scalar “dot” product between the two vectors $\delta \mathbf{i}(t)$ and $\delta \mathbf{v}(t)$.

However, it is not practical to inspect the time-domain integral in Equation 34 for all possible input fluctuations. By applying the Laplace transform, Chua derived a mathematically equivalent yet more practical formula for the local passivity theorem in the complex domain. For the 1D scalar case, the necessary and sufficient condition for an uncoupled 1D circuit element to be LP is that its complexity function or transfer function $H(s; Q)$ is a positive real (PR) function, which satisfies both (1) $\text{Im}[H(s; Q)] = 0$ if $\text{Im}[s] = 0$ and (2) $\text{Re}[H(s; Q)] \geq 0$ if $\text{Re}[s] \geq 0$. Condition (1) is always satisfied since $H(s; Q)$ is a rational function. Condition (2) means that the closed right half plane (RHP) of s maps into the closed RHP of $H(s; Q)$. A simple example for a PR function is $H(s; Q) = a + bs + cs^{-1}$, where a, b , and $c \geq 0$.

Chua proved the following local passivity theorem as a practical test for the PR condition: an uncoupled 1D circuit element is LP at a fixed point iff all the following four criteria are satisfied.

- i) $H(s; Q)$ has no poles in the open RHP ($\text{Re}(s) > 0$).
- ii) $H(s; Q)$ has no higher-order poles (degree $n \geq 2$) on the imaginary axis (Im axis).
- iii) If $H(s; Q)$ has a simple pole $s = i\omega_p$ on the Im axis, then the residue of $H(s; Q)$ at $i\omega_p$ must be a PR number.
- iv) The Im axis (excluding poles) maps into the closed RHP of $H(s; Q)$, i.e., $\text{Re}[H(i\omega; Q)] \geq 0$ for all $\omega \in (-\infty, \infty)$, where $s = i\omega$ is not a pole.

The LA theorem is derived by negating any one of the abovementioned conditions. In other words, an uncoupled 1D circuit element is locally active at a fixed point *iff any one of the following four criteria is satisfied*.

- i) $H(s; Q)$ has a pole in the open RHP $\text{Re}(s) > 0$.
- ii) $H(s; Q)$ has a higher-order pole (degree $n \geq 2$) on the Im axis.
- iii) $H(s; Q)$ has a simple pole on the Im axis with negative-real or complex residue.
- iv) At least some points on the Im axis map into the open left half plane (LHP) of $H(s; Q)$, i.e., $\text{Re}[H(i\omega; Q)] < 0$ for some $\omega \in (-\infty, \infty)$.

For a system of higher dimensions, Chua proved a similar set of four test criteria for LA, where the complexity function $H(s; Q)$ for an 1D element is replaced by the complexity matrix for a multidimensional element.

As explained by Brown et al. (2022b), the local stability of a fixed point is a property that is independent of the local activity of dynamics around it. Near a fixed point, an isolated memristor may have four possible combinations of local stability and local activity

properties that can lead to persistent or decaying dynamics. Since the condition of being both LP and locally unstable is physically unrealizable, one generally only needs to consider three possible scenarios: LP and stable, locally active but asymptotically stable, which is termed as edge of chaos (EOC) by Chua, and locally active and unstable (LA\EOC).

For a 1D uncoupled memristor, if its transfer function has a positive coefficient ($k > 0$ in Equation 31), the classification of its dynamics around a fixed point is determined by the locations of the pole and zero of its transfer function in the complex plane, as specified below.

- i) Locally passive \Leftrightarrow pole in the open LHP ($\text{Re}(p) < 0$) and zero in the closed LHP ($\text{Re}(z) \leq 0$)
- ii) Edge of chaos \Leftrightarrow pole in the open LHP ($\text{Re}(p) < 0$) and zero in the open RHP ($\text{Re}(z) > 0$)
- iii) Locally active but unstable \Leftrightarrow pole in the closed RHP ($\text{Re}(p) \geq 0$)

Plots of $\text{Im}(p)$ versus $\text{Re}(p)$ and $\text{Im}(z)$ versus $\text{Re}(z)$, known as pole–zero diagram, thus, offer a graphical determination of local steady-state dynamics without resorting to time-domain integration.

As discussed previously, for a current-controlled Mott memristor both the pole and the zero are located on the real axis. The pole p of its impedance function $Z(s; Q)$ is always in the open LHP ($\text{Re}(p) < 0$); therefore, it does not possess the LA\EOC dynamics in (iii). On the other hand, the zero z of $Z(s; Q)$ can reside in either the closed LHP or the open RHP, depending on the input current amplitude. Figure 14 shows that $\text{Re}(z)$ flips its sign twice depending on the input current, and the two sign reversals in $\text{Re}(z)$ coincide with the crossovers between the NDR region and the lower and upper PDR regions on the steady-state (i_Q, v_Q) locus.

4.2.3 Pole–zero diagram

Figure 15 visualizes the evolution of p and z locations in the complex plane as functions of the input current for the current-controlled midsize VO_2 Mott memristor. Figure 15A shows that $\text{Re}(p) < 0$ is always satisfied. The coordinates $[x_Q, i_Q, v_Q, \text{Re}(p)]$ for the minimal and maximal calculated values of p , labeled as p_{\min} and p_{\max} , are $[0.998, 25.268 \text{ mA}, 0.935 \text{ V}, -9.543 \times 10^{13}]$ and $[1 \times 10^{-145}, 1.074 \mu\text{A}, 0.132 \text{ V}, -3.273 \times 10^9]$, respectively. As may be noted, p_{\min} and p_{\max} in our calculations are not the actual bounds of p since x_Q can approach to its asymptotes 0 and 1 very closely but will never reach them.

Figure 15B shows that the zero z is located in the LHP at zero current, and it shifts to the right as the current increases. z crosses the Im axis into the RHP at a critical current of $9.077 \mu\text{A}$, as indicated by a pair of nearby fixed points $\{z1, z2\}$ on the opposite side of the Im axis (the same ones as shown in Figure 14). z continues shifting to the right with current until it reaches a maximum value at z_{\max} with a coordinate of $[0.03549, 24.482 \mu\text{A}, 0.578 \text{ V}, 1.327 \times 10^{10}]$. Then, it reverses course and shifts to the left with current. z crosses the Im axis again and returns to the LHP at a second critical current of $971.18 \mu\text{A}$, as indicated by a pair of nearby fixed points $\{z3, z4\}$ on the opposite side of the Im axis (the same ones as shown in Figure 14). Continuously increasing the current will drive x_Q asymptotically toward 1 and further decrease z . We stop the calculation at z_{\min} with a coordinate of $[0.998, 25.268 \text{ mA}, 0.935 \text{ V}, -9.467 \times 10^{13}]$. We

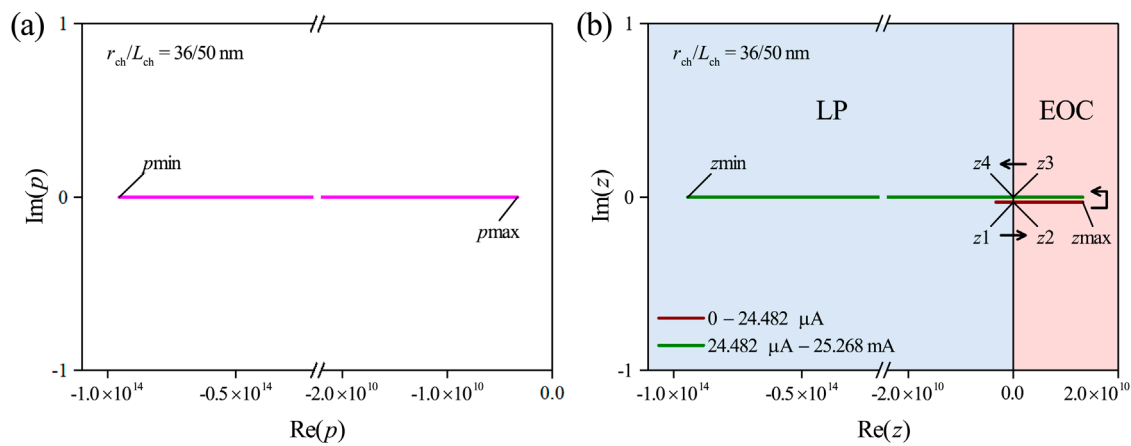


FIGURE 15

Locations of (A) the pole p and (B) the zero z in the complex plane as functions of the input current, calculated for the midsize VO₂ Mott memristor. Both p and z are located on the real axis. p remains in the LHP, with its minimal and maximal calculated values indicated by p_{\min} and p_{\max} , respectively. z is located in the LHP at $i_Q = 0$ and shifts to the right with current, crossing the imaginary axis into the RHP at 9.077 μA , as indicated by $\{z1, z2\}$. It continues to shift to the right until reaching z_{\max} at 24.482 μA , then shifts to the left with current, and reenters LHP at 971.18 μA , as indicated by $\{z3, z4\}$. The minimum of z is represented as z_{\min} . The part of z locus between 0 and 24.482 μA (brown) is shifted vertically for clarity. The LP and EOC regions are highlighted by blue and red colors, respectively.

use the same blue and red colors, as shown in Figure 14 to highlight the LP and EOC regions, respectively.

Applying the pole-zero diagram LA criteria specified above, we conclude that an uncoupled 1D Mott memristor at a fixed point either belongs to the LP class or the EOC class but can never belong to the LA\EOC class. For the midsize VO₂ device, the LP \rightarrow EOC transition occurs at $(x_Q, i_Q, v_Q) \approx (0.00567, 9.076 \mu\text{A}, 1.007 \text{V})$. The EOC \rightarrow LP transition occurs at $(x_Q, i_Q, v_Q) \approx (0.60629, 971.2 \mu\text{A}, 0.0973 \text{V})$.

4.3 Frequency response

An important question arises: for an uncoupled 1D Mott memristor that is current-biased in the EOC region (which coincides with its NDR region), will it remain to be locally active, capable of amplifying a small sinusoidal input fluctuation at arbitrarily high frequencies? Otherwise, is there a finite upper limit for the input fluctuation frequency, beyond which the element can no longer provide an AC signal gain? In this section, we shift the small-signal analysis to the frequency domain, which allows us to apply the fourth criterion in Chua's LA theorem to answers these questions.

For dynamical systems, it is useful to study the system's frequency response. In small-signal analysis, this is performed by applying a single-frequency sinusoidal fluctuation of current input $i(t) = I \sin \omega t$ with an angular frequency $\omega = 2\pi f$, where f is the frequency of the sine wave. The amplitude $I \ll 1$ is very small to satisfy the small-signal condition. For a 1D Mott memristor at a fixed point Q , substituting $s = i\omega$ for the complex frequency s in the small-signal impedance $Z(s; Q)$ in Equation 26 and rearranging into its real and imaginary parts, we obtain

$$Z(i\omega; Q) = \left[\frac{a_0 b_0 + a_1 b_1 \omega^2}{a_0^2 + a_1^2 \omega^2} \right] + i \left[\frac{(a_0 b_1 - a_1 b_0) \omega}{a_0^2 + a_1^2 \omega^2} \right]. \quad (35)$$

The functions $\text{Re}Z(i\omega; Q)$ and $\text{Im}Z(i\omega; Q)$ are the real and imaginary parts of the frequency response, respectively; these are expressed in terms of the small-signal impedance $Z(i\omega; Q)$, both of which are rational functions of ω :

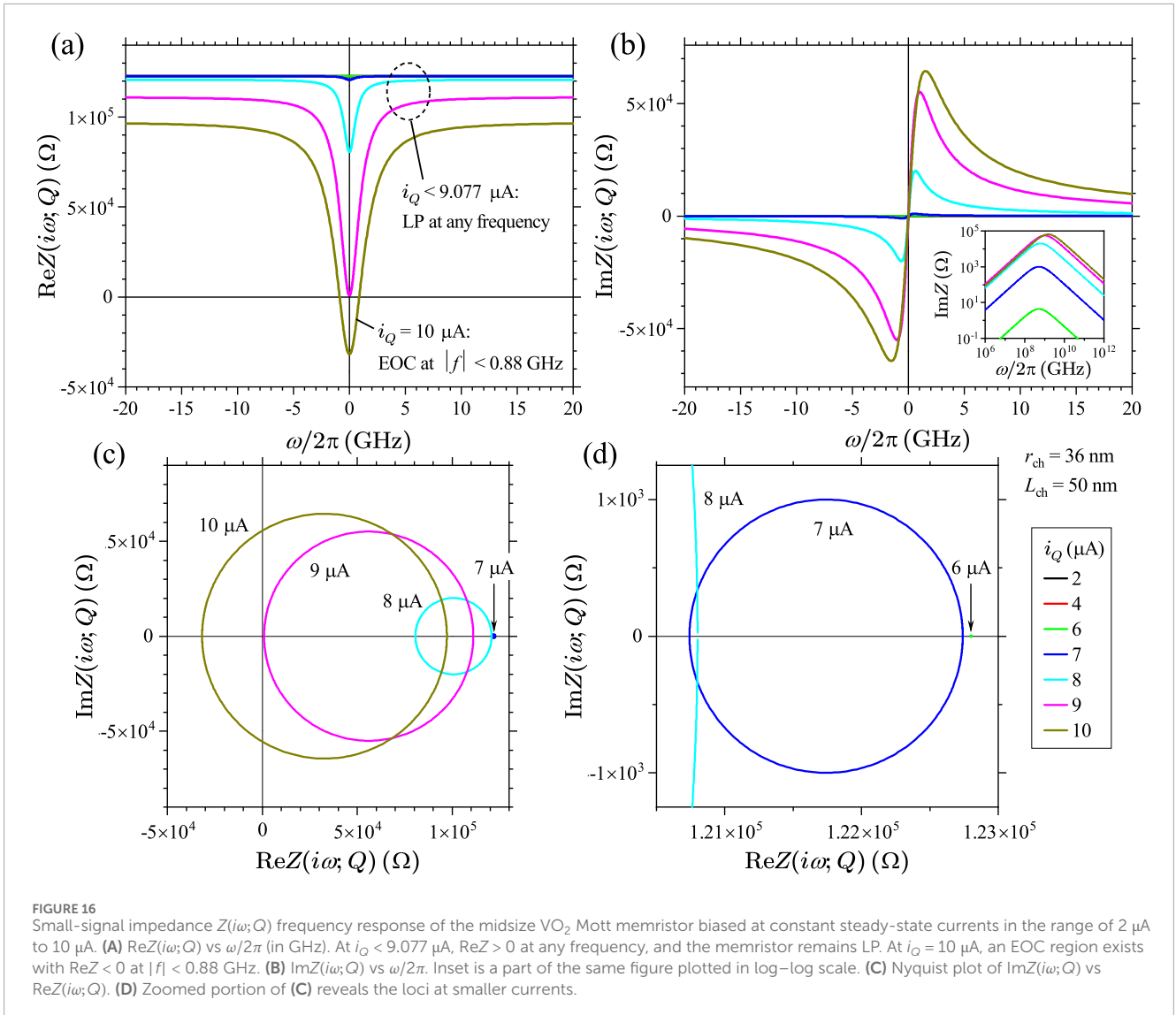
$$\text{Re}Z(i\omega; Q) = \frac{a_0 b_0 + a_1 b_1 \omega^2}{a_0^2 + a_1^2 \omega^2}, \quad (36)$$

$$\text{Im}Z(i\omega; Q) = \frac{(a_0 b_1 - a_1 b_0) \omega}{a_0^2 + a_1^2 \omega^2}, \quad (37)$$

where the coefficients a_0 , a_1 , b_0 , and b_1 are provided in Equations 27–30.

Figures 16A, B show the plot of the frequency dependence of $\text{Re}Z(i\omega; Q)$ and $\text{Im}Z(i\omega; Q)$ (also referred to as $\text{Re}Z$ and $\text{Im}Z$, respectively, hereafter) at different steady-state current levels between 2 μA and 10 μA for the midsize VO₂ Mott memristor calculated using Equations 36, 37. We replaced angular frequency ω with frequency f as the x -axis for engineering convenience. Notice that positive and negative frequencies refer to the opposite directions of rotation for the complex exponential $e^{i\omega t}$ vector in the complex plane. $\text{Re}Z$ is an even function of frequency, while $\text{Im}Z$ is an odd function of frequency. At small currents, $\text{Re}Z$ is in the order of $10^5 \Omega$ and shows very weak frequency dependence. Increasing current will "pull" it toward the negative direction and develop a dip centered at zero frequency. The higher the current is, the stronger the frequency dependence becomes.

Frequency response of $\text{Re}Z$ shows a dramatic change as the current increases from 9 μA to 10 μA . From the pole-zero diagram analysis, we already know that for the midsize VO₂ Mott memristor, the critical current at the LP (lower PDR) to EOC (NDR) crossover is $i_{c1} \approx 9.077 \mu\text{A}$. At $i_Q = 9 \mu\text{A}$, $\text{Re}Z$ still remains positive at any frequency, but its minimum at zero frequency is very close to the origin. At $i_Q = 10 \mu\text{A}$, $\text{Re}Z$ turns negative at frequencies lower than the limit $|f_{\max}| \approx 0.88 \text{ GHz}$, indicating that the element is locally active within certain frequency upper bound. This (+) \rightarrow



(–) sign reversal in $\text{Re}Z$ is yet another hallmark of the LP \rightarrow EOC transition and provides new information on *the boundary of the EOC region in the frequency domain*.

The value of f_{\max} can be derived from Chua's fourth LA criterion. For an uncoupled 1D current-driven memristor in the frequency domain, $\text{Re}Z(i\omega; Q) < 0$; for some finite angular frequencies, $\omega \in (-\infty, \infty)$ is a sufficient condition for it to be LA. From Equation 35, this means $a_0 b_0 + a_1 b_1 \omega^2 < 0$ or $\omega^2 < \frac{-a_0 b_0}{a_1 b_1}$. Therefore, a 1D uncoupled Mott memristor is locally active if the angular frequency is lower than the upper bound specified as follows:

$$|\omega| < \omega_{\max} = \sqrt{\frac{-a_0 b_0}{a_1 b_1}}, \quad (38)$$

which also requires that $\frac{a_0 b_0}{a_1 b_1} < 0$ so that ω_{\max} in Equation 38 is a real number.

At small currents, $\text{Im}Z$ is both very small and shows very weak frequency dependence. As the current increases, its amplitude and frequency dependence become more pronounced. The amplitude of $\text{Im}Z$ first increases rapidly with frequency before reaching a peak at a characteristic frequency f_p , and then, it decreases with frequency

and asymptotically approaches the x -axis. $|f_p|$ increases with the current and reaches 1.51 GHz at $i_Q = 10 \mu\text{A}$. Inset of Figure 16B presents the same frequency dependence of $\text{Im}Z$ plotted on a log–log scale, which shows that $\text{Im}Z$ is proportional to the frequency for $|f| < |f_p|$ and inversely proportional to the frequency for $|f| > |f_p|$.

4.3.1 Nyquist plot

It is instructive to plot the locus of $\text{Im}Z(i\omega; Q)$ vs. $\text{Re}Z(i\omega; Q)$ in Cartesian coordinates, with ω indicated as a parameter. Such a parametric plot is called a Nyquist plot, a graphical technique used to provide insights into the stability of a dynamical system.

Figure 16C shows the loci of the Nyquist plot for the same VO_2 device, as shown in Figures 16A, B. Figure 16D presents a zoomed-in portion of it to reveal those much smaller loci at $i_Q \leq 7 \mu\text{A}$. Ostensibly, the locus of small-signal $\text{Im}Z(i\omega; Q)$ vs $\text{Re}Z(i\omega; Q)$ at a finite steady-state current appears to be a circle centered on the x -axis. Increasing the current will inflate the radius of the circle and move its center toward the negative direction. Points in the upper half-plane correspond to positive frequencies, and those in

the lower half-plane correspond to negative frequencies. Increasing the frequency modulus will move a point in the right direction along the upper or lower arm of the locus. A closer look reveals that the left half of the locus intersects the x -axis at zero frequency. For the right half, the distance between the locus and the x -axis approaches 0 as $|f| \rightarrow \infty$, but there is no intersection at any finite frequency. In other words, the x -axis is a horizontal asymptote for the right half of the locus. Therefore, the locus of $\text{Im}Z(i\omega; Q)$ vs $\text{Re}Z(i\omega; Q)$ is actually an open set of points rather than a closed loop. At $i_Q \approx 9.077 \mu\text{A}$, the locus crosses the y -axis into the LHP, as illustrated by the two loci at $9 \mu\text{A}$ and $10 \mu\text{A}$. Therefore, the Nyquist plot provides another visualization of the LP \rightarrow EOC transition as the steady-state current increases.

Figure 17 is an annotated Nyquist plot for the $\text{Im}Z$ vs $\text{Re}Z$ locus of the same VO_2 device at $i_Q = 10 \mu\text{A}$, highlighting several key points on the locus. We use the same blue and red colors, as shown in Figures 14, 15 to represent the LP and EOC regions, respectively. Clearly, the lower half of the locus is a reflection of the upper half over the x -axis, by negating the values of $\text{Im}Z$ and frequency at the same $\text{Re}Z$ value. The solid dot (\bullet) at $\text{Re}Z \approx -3.17 \times 10^4$ represents the x -intercept of the locus at zero frequency, as indicated by a pair of nearby points at $f = 1 \text{ Hz}$ and $f = -1 \text{ Hz}$. The open circle (\circ) at $\text{Re}Z \approx 9.72 \times 10^4$ represents the x -asymptote of the locus as $|f| \rightarrow \infty$, as indicated by a pair of nearby points at $f = 1 \text{ THz}$ and $f = -1 \text{ THz}$. The two pairs of points at $f = \pm 0.871 \text{ GHz}$ and $f = \pm 0.895 \text{ GHz}$ indicate the crossover from the EOC (red) region to the LP (blue) region as frequency exceeds 0.88 GHz .

4.3.2 Frequency-domain equivalent circuit

The frequency-domain equivalent circuit of an isolated Mott memristor can be readily obtained by substituting a_0 , a_1 , b_0 , and b_1 in Formula 35 of $Z(i\omega; Q)$ with R_1 , R_2 , and C_1 using Equations 27–30. The real part of $Z(i\omega; Q)$ as shown in Formula 36, now defined as the frequency-domain resistance function, takes the form of

$$R_\omega(\omega, Q) \triangleq \text{Re}Z(i\omega; Q) = \frac{(R_1 + R_2) + (R_1 C_1)^2 R_2 \omega^2}{1 + (R_1 C_1)^2 \omega^2}, \quad (39)$$

which can be further rewritten by replacing C_1 with $-1/b_{11}R_1$ using Equation 33

$$R_\omega(\omega, Q) = \frac{b_{11}^2 (R_1 + R_2) + R_2 \omega^2}{b_{11}^2 + \omega^2}. \quad (40)$$

The sign of $R_\omega(\omega, Q)$ can be either positive or negative, depending on the (ω, Q) coordinate. $R_\omega(\omega, Q) \geq 0$ maps to the LP region, and $R_\omega(\omega, Q) < 0$ maps to the EOC region. The angular frequency in Formula 38 to satisfy Chua's fourth LA criterion now becomes

$$|\omega| < \omega_{\max} = -b_{11} \sqrt{\frac{-(R_1 + R_2)}{R_1}}. \quad (41)$$

Since the memristance R_2 is always positive, this indicates that $(R_1 + R_2)$ must be negative for ω_{\max} to be a real number. From the previous discussion of Figure 11D, $(R_1 + R_2) < 0$ maps into the NDR (EOC) region on the steady-state (i_Q, ν_Q) locus.

We now look at the imaginary part of $Z(i\omega; Q)$. By substituting a_0 , a_1 , b_0 , and b_1 in Formula 37 of $\text{Im}Z(i\omega; Q)$ with R_1 , R_2 , and C_1 , we rewrite $\text{Im}Z(i\omega; Q)$ as

$$\text{Im}Z(i\omega; Q) \triangleq L_\omega(\omega, Q) \omega = \left[\frac{-R_1^2 C_1}{1 + (R_1 C_1)^2 \omega^2} \right] \omega, \quad (42)$$

where $L_\omega(\omega, Q)$ is defined as the frequency-domain inductance function. Evidently, the sign of $L_\omega(\omega, Q)$ is determined by the sign of C_1 . Since C_1 remains negative at any fixed point Q (see discussion on Figure 11C), $L_\omega(\omega, Q)$ is always positive, regardless of the location of Q in the LP or EOC region. Therefore, the frequency-domain reactance of an isolated Mott memristor is always inductive, causing its voltage output to lead a sinusoidal current input in phase. $\text{Im}Z(i\omega; Q)$ can be further rewritten by replacing C_1 with $-1/b_{11}R_1$ as follows:

$$L_\omega(\omega, Q) \omega = \left(\frac{b_{11} R_1}{b_{11}^2 + \omega^2} \right) \omega. \quad (43)$$

Finally, the frequency-domain small-signal impedance function is expressed as

$$Z(i\omega; Q) = R_\omega(\omega, Q) + iL_\omega(\omega, Q) \omega. \quad (44)$$

Through Equations 39–44, we conclude that in the frequency domain, an uncoupled Mott memristor can be considered a positive inductor in series with a resistor that is negative up to a certain maximum frequency (the EOC region) and positive beyond it (the LP region) (Liang et al., 2022).

4.3.3 Phase diagram for complexity

The fourth criterion in Chua's LA theorem states that a negative real part of the complexity function of an uncoupled 1D circuit element at some finite frequencies is a sufficient condition for it to be locally active. For a current-driven memristor, its complexity function is the impedance function $Z(i\omega; Q)$. Since $Z(i\omega; Q)$ depends on both the angular frequency ω and the steady-state current i_Q , plotting $\text{Re}Z$ as a color scale with current and frequency as the (x, y) coordinate provides a visualization of the LP and EOC regions in the operating parameter space. The $\text{Re}Z = 0$ contour outlines the border between these regions. One could refer to such a 2D graphical representation of $\text{Re}Z$ a *phase diagram for complexity*.

Figure 18 shows the plot of the 2D color-scale map of $\text{Re}Z(i_Q, f)$ for the midsize VO_2 Mott memristor. Figure 18A presents the low-current region, plotted up to $20.8 \mu\text{A}$. It shows that at lower frequencies, the LP \rightarrow EOC transition occurs at a nearly frequency-independent critical current $i_{c1} \approx 9.077 \mu\text{A}$, as indicated by an almost vertical $\text{Re}Z = 0$ contour. At frequencies higher than $\sim 0.88 \text{ GHz}$, the critical current increases drastically, and consequently, the direction of the $\text{Re}Z = 0$ contour turns almost parallel to the current axis. Figure 18B shows the same color-scale $\text{Re}Z$ map, with a much wider current range up to 2 mA , revealing an EOC \rightarrow LP transition that occurs at a nearly constant critical current $i_{c2} \approx 971.18 \mu\text{A}$ at low frequencies. The direction of the $\text{Re}Z = 0$ contour shows a similar crossover from nearly vertical at frequencies lower than $\sim 0.88 \text{ GHz}$ to almost horizontal at higher frequencies.

To understand the scaling trend of the local activity region versus device size, we plotted the 2D color-scale map of $\text{Re}Z(i_Q, f)$ for

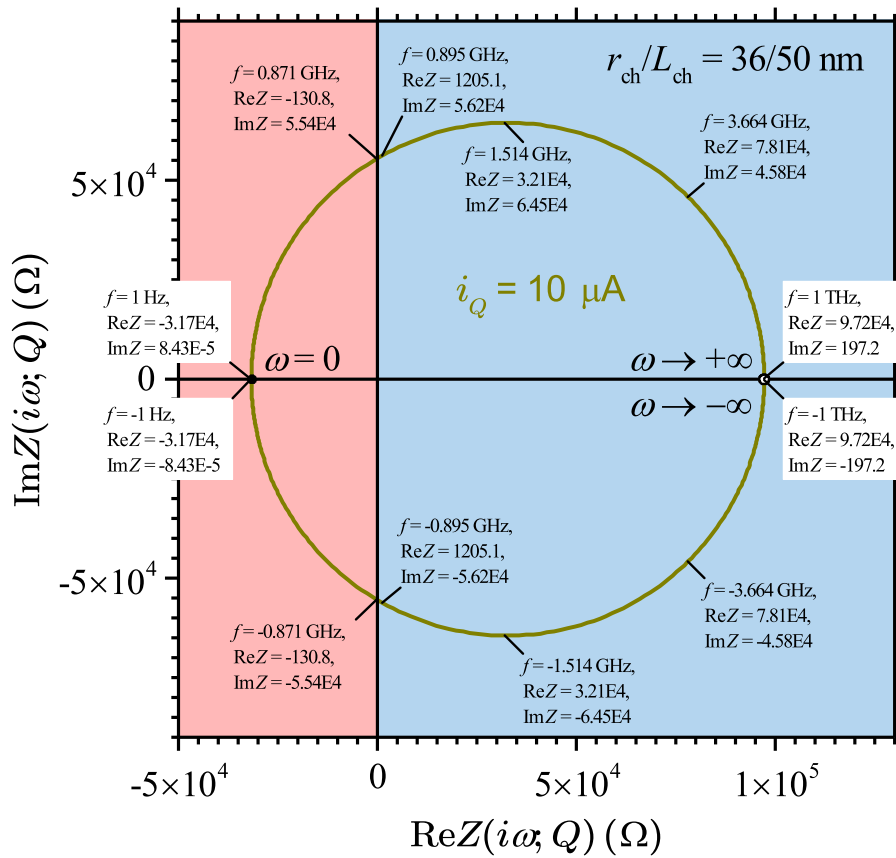


FIGURE 17 Nyquist plot of $\text{Im}Z(i\omega; Q)$ vs $\text{Re}Z(i\omega; Q)$ of the midsize VO_2 Mott memristor at a constant steady-state current $i_Q = 10 \mu\text{A}$. The LP and EOC regions are highlighted in blue and red colors, respectively.

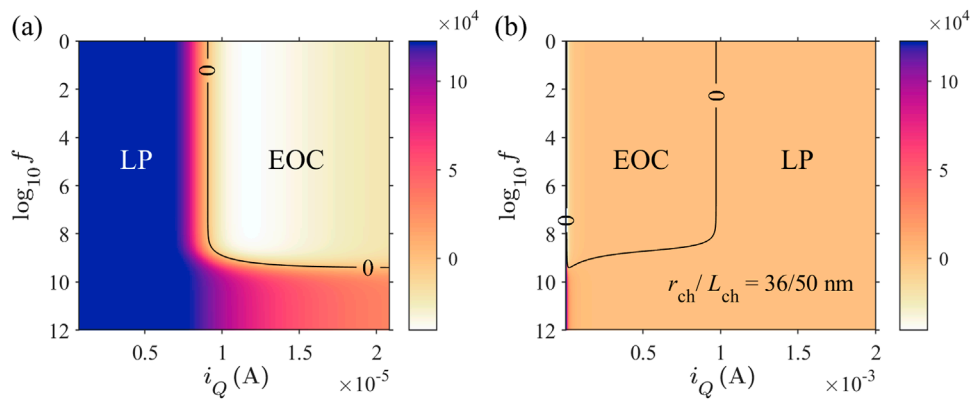


FIGURE 18 2D color-scale map of $\text{Re}Z(i_Q, f)$ for the midsize VO_2 Mott memristor as a visualization of the LP and EOC regions in the frequency and current parameter space, showing (A) its low-current region up to $i_Q = 20.8 \mu\text{A}$ and (B) a wide-range map plotted up to $i_Q = 2 \text{ mA}$. Frequencies are plotted on a logarithmic scale.

VO_2 Mott memristors with different combinations of r_{ch} and L_{ch} sizes. Figure 19 shows the main results of this analysis. We found that $\text{Re}Z$ is independent of the VO_2 channel length L_{ch} . This is not unexpected since the VO_2 compact model is essentially 2D in nature. Figure 19A presents a zoomed-in view of the $\text{Re}Z = 0$ contours for

VO_2 devices with r_{ch} in the range of 5–60 nm. The shaded area under each contour is the EOC region that satisfies $\text{Re}Z(i_Q, f) < 0$. The apex of each contour corresponds to the maximum frequency f_{max} at which the device remains locally active. Figure 19B shows that f_{max} increases super-exponentially as the VO_2 channel radius

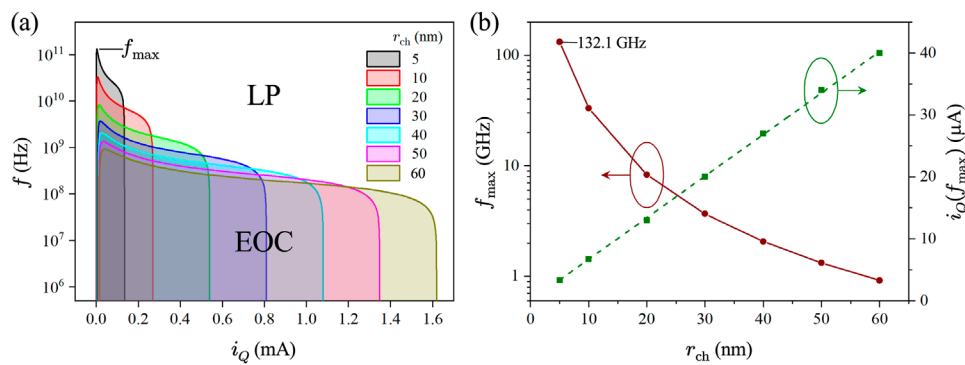


FIGURE 19

(A) Zoomed-in view of the $\text{Re}Z = 0$ contours for VO_2 Mott memristors with channel radius r_{ch} in the range of 5 nm–60 nm. Shaded areas under the contours are the EOC regions, where $\text{Re}Z(i_Q, f) < 0$. The apex of each contour at $f = f_{\text{max}}$ shows the maximum frequency of the EOC region. (B) Scaling of f_{max} (brown) and $i_Q(f_{\text{max}})$ (green) vs. r_{ch} . f_{max} increases super-exponentially as r_{ch} decreases. $i_Q(f_{\text{max}})$ scales linearly with r_{ch} . A linear regression (dashed line) yields a slope of 671 ± 3 (A/m) and a coefficient of determination $R^2 = 0.99988$.

r_{ch} shrinks. For a VO_2 device with r_{ch} as small as 5 nm, f_{max} reaches as high as 132.1 GHz. This favorable device scaling enhances the operational bandwidth for using Mott memristors as locally active components. It also reveals that the steady-state current at f_{max} is directly proportional to the radius of the conduction channel r_{ch} .

5 Local analysis of reactively coupled Mott memristors: two-dimensional relaxation oscillator

The topological constraint of an isolated 1D Mott memristor limits the dynamics it can exhibit, making damped or persistent oscillations impossible. However, this constraint may get lifted when the memristor is coupled to one or more reactive elements. The coupling may increase both the system's dimension and the complexity of its dynamics. For continuous dynamical systems, the Poincaré–Bendixson theorem states that chaos only arises in three or more dimensions.

For simplicity, we will limit our discussions to 2D cases. Experimentally, it is difficult to characterize an isolated memristor without inadvertently coupling it to one or more reactive elements. On the other hand, such couplings introduce interesting phenomena such as self-excited persistent oscillations or stable limit cycles. Limit cycles belong to an important category of attractors, alongside fixed points. A nonlinear system consisting of a Mott memristor coupled with reactive elements may exhibit a local Hopf-like bifurcation. As a bifurcation parameter is varied, its local stability abruptly switches between a fixed point and a limit cycle around it. Persistent oscillations that arise out of Hopf-like bifurcations are well-studied in the Hodgkin–Huxley and FitzHugh–Nagumo models of biological nerve cells (Hastings, 1974; Troy, 1978; Rinzel and Miller, 1980; Dogaru and Chua, 1998), and they are relevant for the intriguing neuronal signaling phenomena such as firing action potentials. However, finding the limit cycle solutions for a dynamical system is generally a very difficult mathematical problem. The unsolved second part of Hilbert's 16th problem is a well-known

example. The local analysis techniques that we have discussed so far are not sufficient, and one needs to resort to global nonlinear techniques such as nullcline analysis and Lyapunov stability theory. In this section, we apply local analysis to a simple example of a reactively coupled Mott memristor. In the next section, we take a cursory glance at global analysis using the same example to illustrate its usefulness.

5.1 Voltage-biased relaxation oscillator circuit

A voltage-biased Pearson–Anson (PA) relaxation oscillator circuit is a simple yet very useful example to illustrate the effect of such external couplings. As shown in Figure 20, if a Mott memristor M is connected to a capacitor C_p in parallel and both of them are connected to a resistor R_s placed in series, then together they form a composite circuit, which can be represented as $\{(M||C_p) + R_s\}$. In practice, one may inadvertently form such a circuit when attempting to test an individual memristor device without explicitly connecting C_p and R_s . C_p may arise from the geometric capacitance between the two electrodes of a thin-film metal-oxide-metal device or from the stray capacitance of coaxial cables. R_s may arise from the output resistance of a voltage source, the resistance of metal lead wires, and contact resistance at the metal–oxide interfaces. If a DC voltage bias V_{dc} is applied to one terminal of R_s , and the other terminal of R_s connected to the memristor is taken as the output node, the $\{(M||C_p) + R_s\}$ circuit forms a PA or relaxation oscillator. If the passive elements and voltage bias are appropriately valued, it exhibits persistent self-excited oscillations that will be elaborated below.

Over the past 100 years, the prototype $\{(M||C_p) + R_s\}$ relaxation oscillator circuit has been implemented by a variety of physical mechanisms for the locally active element M . The original PA oscillator, invented in 1921 (Pearson and Anson, 1921), used a gas-discharge neon bulb, which achieves the EOC region through glow discharge once the gas ionization breakdown threshold voltage is reached. In the silicon age, many types of voltage-controlled

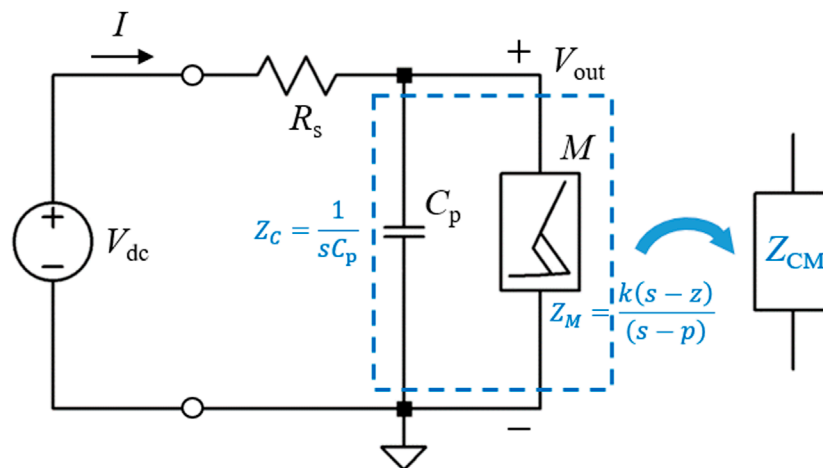


FIGURE 20

Circuit diagram of a DC voltage-biased Pearson–Anson relaxation oscillator formed by a Mott memristor M in parallel with a capacitor C_p and both connected in series with a resistor R_s . Formulas in blue are the s -domain impedances of M and C_p (with an initial condition $v(0) = 0$) used to derive the total impedance Z_{CM} (see Equations 45, 46).

oscillator (VCO) circuits have been developed for applications in digital and RF systems; among these, astable multivibrators based on relaxation oscillations offer certain benefits, such as guaranteed startup and the elimination of unscalable inductors (Newcomb and Sellami, 1999). Conceptually, an astable multivibrator is based on one energy storage element (a capacitor) and one hysteretic threshold switch, e.g., a Schmitt trigger that can be built with an operational amplifier comparator circuit. It produces a square wave output instead of the sawtooth output waveforms in LAM-based relaxation oscillators.

From the scalability perspective, it is desirable to reduce the circuit element count. An emitter-coupled Schmitt trigger can be built using two transistors connected in a positive feedback loop with typically five resistors to set the desired hysteresis thresholds. A single-transistor silicon relaxation oscillator can be realized by configuring a bipolar junction transistor (BJT) as a reverse-biased diode. For example, in the circuit shown in Figure 20, one can use an npn BJT as the element M by connecting its emitter to the positive node, its collector to the ground, and leaving its base terminal open. As the capacitor is charged up until its voltage reaches a threshold between 5 and 7 V, an avalanche breakdown is triggered across the emitter and collector, and the BJT suddenly conducts current, producing an NDR region. Including the voltage drop across the series resistor, a silicon BJT relaxation oscillator typically requires a supply voltage of at least 12 V, which is a clear disadvantage compared to a Mott memristor oscillator that can operate at a much lower supply voltage like 1 V. Another advantage of Mott memristor oscillators is their higher operating frequencies. Silicon multivibrators operate between a few kHz and a few hundred MHz, depending on the transistor technology. As shown in the previous section, the maximum frequency for the EOC region of a VO_2 Mott memristor increases super-exponentially as the device is miniaturized. Operating at 1–10 GHz is feasible using device sizes within the reach of modern lithography capability.

5.2 Small-signal analysis: the element combination approach

The $\{(M||C_p) + R_s\}$ Mott memristor PA circuit is a second-order system with two state variables, namely, charge q_C stored in the capacitor C_p (or equivalently voltage v across C_p and M) and fraction of the metallic phase x in the memristor M . This second-order system is described by two coupled differential equations. Its steady states or fixed points can be found using the global nullcline method, which are covered in the next section. For the sake of continuity in the discussion, we assume that fixed points of the PA oscillator have already been determined and focus, for now, on what can be inferred from local analysis. We can combine $(M||C_p)$ into a composite second-order nonlinear element (dashed box in Figure 20) and then apply the small-signal local analyses and Chua's LA criteria to the system consisting of the composite element in series with R_s .

To perform small-signal analysis, we first need to find out the transfer function of the composite circuit. In the s domain, impedance of a capacitor C_p is $1/sC_p$ when the initial condition $v(0) = 0$ is assumed. Impedance M in its pole-zero form is $Z_M(s; Q) = \frac{k(s-z)}{(s-p)}$ (Equation 31). One can derive the transfer function $H(s; Q)$ of the PA oscillator at a fixed point Q using the voltage divider formula as follows:

$$H(s; Q) = V_{\text{out}}/V_{\text{dc}} = Z_{CM}/(R_s + Z_{CM}), \quad (45)$$

where Z_{CM} is the total impedance of C_p in parallel with M such that

$$Z_{CM} = Z_C Z_M / (Z_C + Z_M) = \frac{k(s-z)}{kC_p s^2 + (1 - kC_p z)s - p}. \quad (46)$$

Substituting the expression of Z_{CM} in the transfer function formula, we obtain

$$H(s; Q) = \frac{k(s-z)}{kR_s C_p s^2 + (R_s + k - kR_s C_p z)s - (R_s p + kz)}. \quad (47)$$

One can see that $H(s; Q)$ of a Mott memristor PA oscillator has the same zero as an uncoupled memristor, but it has a pair of two poles instead of one pole for an uncoupled memristor.

To simplify the expression of $H(s; Q)$ in Equation 47, we define a time constant $\tau_0 \triangleq R_s C_p$ and a cutoff frequency $\omega_0 \triangleq (R_s C_p)^{-1}$. We also substitute k with the positive real memristance function R_{ch} and rewrite $H(s; Q)$ in the pole-zero form as follows:

$$H(s; Q) = \frac{k'(s-z)}{d_2 s^2 + d_1 s + d_0} = \frac{k'(s-z)}{(s-p_+)(s-p_-)}, \quad (48)$$

where

$$k' = \omega_0, \quad (49)$$

$$d_2 = 1, \quad (50)$$

$$d_1 = \frac{R_s + R_{ch} - R_{ch}\tau_0 z}{R_{ch}\tau_0} = \left(1 + \frac{R_s}{R_{ch}}\right)\omega_0 - z, \quad (51)$$

$$d_0 = \frac{-(R_s p + R_{ch} z)}{R_{ch}\tau_0} = -\frac{R_s}{R_{ch}}\omega_0 p - \omega_0 z. \quad (52)$$

Here, k' in Equation 49 is a positive real coefficient, p and z in Equations 51, 52 are the pole and zero of the memristor M . We then derive the pair of poles p_{\pm} in Equation 48 for the PA oscillator by finding the roots of the quadratic equation $d_2 s^2 + d_1 s + d_0 = 0$

$$p_{\pm} = \frac{-d_1 \pm \sqrt{d_1^2 - 4d_2 d_0}}{2d_2} = \frac{-d_1 \pm \sqrt{d_1^2 - 4d_0}}{2}. \quad (53)$$

The discriminant $d_1^2 - 4d_2 d_0$ of the quadratic equation is expressed as follows:

$$d_1^2 - 4d_2 d_0 = z^2 + 2\omega_0 z \left(1 - \frac{R_s}{R_{ch}}\right) + \left(1 + \frac{R_s}{R_{ch}}\right)^2 \omega_0^2 + 4\omega_0 p \left(\frac{R_s}{R_{ch}}\right). \quad (54)$$

If $d_1^2 - 4d_2 d_0 \geq 0$, then p_{\pm} are positive or negative real numbers. Otherwise, if $d_1^2 - 4d_2 d_0 < 0$, then p_{\pm} form a complex conjugate pair. Without loss of generality, we retain the standard expression for the discriminant of a quadratic equation instead of replacing d_2 with 1 (Equation 50) for the particular case of a Mott memristor PA circuit.

To understand the effects of parameters R_s , C_p , and V_{dc} on the dynamical behavior of a Mott memristor PA oscillator, we first calculated the values of the pair of poles p_{\pm} of its small-signal transfer function $H(s; Q)$, using Equation 53 by varying one parameter while keeping the other two parameters fixed. We then applied the parametric Nyquist plot technique to gain insights into the stability of the second-order system.

Let us first examine the effect of varying R_s while keeping C_p and V_{dc} fixed. Figure 21A shows the Nyquist plot of $\text{Im}(p_{\pm})$ vs $\text{Re}(p_{\pm})$ for the midsize VO₂ Mott memristor PA oscillator with $C_p = 1$ pF, $V_{dc} = 1.2$ V, and R_s stepped from 100 Ω to 27 k Ω at a 100 Ω interval. It reveals three distinctive regions as R_s increases: (1) when $R_s = 100 \Omega - 200 \Omega$, p_+ and p_- are negative real numbers. (2) When $R_s = 300 \Omega - 7.5$ k Ω , p_+ and p_- form a complex conjugate pair. (3) When $R_s = 7.6$ k $\Omega - 27$ k Ω , p_+ and p_- are positive real numbers. Figure 21B presents a zoomed-in view of Figure 19A, which reveals that increasing R_s from 3.3 k Ω to 3.4 k Ω flips the sign of $\text{Re}(p_{\pm})$

from negative to positive, i.e., the pair of poles crosses over from the LHP to the RHP. If we consider the second-order system an uncoupled one-port element and apply the first criterion of Chua's LA theorem the element is locally active and unstable (LA\EOC) at $R_s \geq 3.4$ k Ω since $H(s; Q)$ has a pair of poles in the open RHP. At $R_s \leq 3.3$ k Ω , both poles lie in the LHP, implying a local asymptotic stability. Since both the EOC and LP regions are locally stable, we need to use the fourth LA criterion (LA if $\text{Re}[H(i\omega; Q)] < 0$ for some finite ω) to examine the system's activity. It shows that the system is in the EOC region for $1135.4 \Omega \leq R_s \leq 3.3$ k Ω . At $R_s < 1135.4 \Omega$, the system is LP. The second-order system's EOC-LP crossover occurs when the oscillator's load line $V = V_{dc} - IR_s$ intersects the steady-state locus of the memristor M at the critical point $Q_0 = (i_0, v_0)$ between the NDR and upper PDR regions (see Figure 14F). For the midsize VO₂ memristor, $i_0 = 971.18$ μ A and $v_0 = 0.0973$ V. Note that this crossover coincides with the EOC-LP crossover for an isolated memristor M (see Section 4.2.3). Extracting $\text{Re}[H(i\omega; Q)]$ from Formula 47, one can derive the frequency limit for the EOC region as $f_{\max} = \frac{1}{2\pi} \sqrt{\frac{-(R_s z p + R_s z^2)}{R_s + R_2}}$. At a fixed V_{dc} , f_{\max} grows with R_s in a sublinear fashion. For the case of $V_{dc} = 1.2$ V, f_{\max} rises from 182.5 MHz at $R_s = 1.2$ k Ω to 653.7 MHz at $R_s = 3.3$ k Ω .

A similar crossover is observed by varying V_{dc} while keeping R_s and C_p fixed. Figure 21C shows the Nyquist plot of $\text{Im}(p_{\pm})$ vs $\text{Re}(p_{\pm})$ for the midsize VO₂ Mott memristor PA oscillator with $R_s = 3.4$ k Ω , $C_p = 1$ pF, and V_{dc} stepped from 0.55 V to 13.5 V at 50-mV interval. It reveals the following two distinctive regions as V_{dc} increases: (1) when $V_{dc} = 0.55$ V - 0.65 V, p_+ and p_- are positive real numbers. (2) When $V_{dc} = 0.7$ V - 13.5 V, p_+ and p_- form a complex conjugate pair. Figure 21D shows a zoomed-in view of Figure 21C, which reveals that increasing V_{dc} from 1.2 V to 1.25 V flips the sign of $\text{Re}(p_{\pm})$ from positive to negative, i.e., the pair of poles crosses over from the RHP to the LHP. Applying the first LA criterion in a similar manner, the system is LA\EOC at $V_{dc} \leq 1.2$ V since $H(s; Q)$ has a pair of poles in the open RHP. At $V_{dc} \geq 1.25$ V, the system is locally stable since both poles lie in the LHP. The fourth LA criterion can be used to determine the system's activity. It shows that the system is in the EOC region at 1.25 V $\leq V_{dc} \leq 3.3993$ V. At $V_{dc} > 3.3993$ V, the system is LP. Once again, the system's EOC-LP crossover occurs when the load line intersects the steady-state locus of M at Q_0 . At a fixed R_s , the frequency limit f_{\max} for the EOC region decreases with V_{dc} in a nonlinear fashion. For the case of $R_s = 3.4$ k Ω , f_{\max} drops from 649.6 MHz at $V_{dc} = 1.25$ V to 100.7 MHz at $V_{dc} = 3.35$ V.

Instead of using the sign of $\text{Re}(p_{\pm})$ in the Cartesian coordinate as a test for the first LA criterion, one can also use the argument (phase) of a pole in the polar coordinate. The p_+ pole is located in the first and second quadrants, including the Re and Im + axes. Its complex conjugate p_- is located in the third and fourth quadrants, including the Re and Im- axes. We only need to examine $\arg(p_+)$, argument of the p_+ pole of $H(s; Q)$, as a test for the first LA criterion. A crossover from LA\EOC to EOC occurs if $\arg(p_+)$ increases from below 90° to above 90°, i.e., p_+ moves from the first quadrant to the second quadrant by crossing the Im + axis.

At a fixed C_p parameter, one can thus visualize the LA and LP operating regions of a Mott memristor PA oscillator by plotting a 2D color-scale map of $\arg(p_+)$ with R_s and V_{dc} parameters as the x and y coordinates, respectively. The $\arg(p_+) = 90^\circ$ contour line separates the EOC and LA\EOC regions. Then

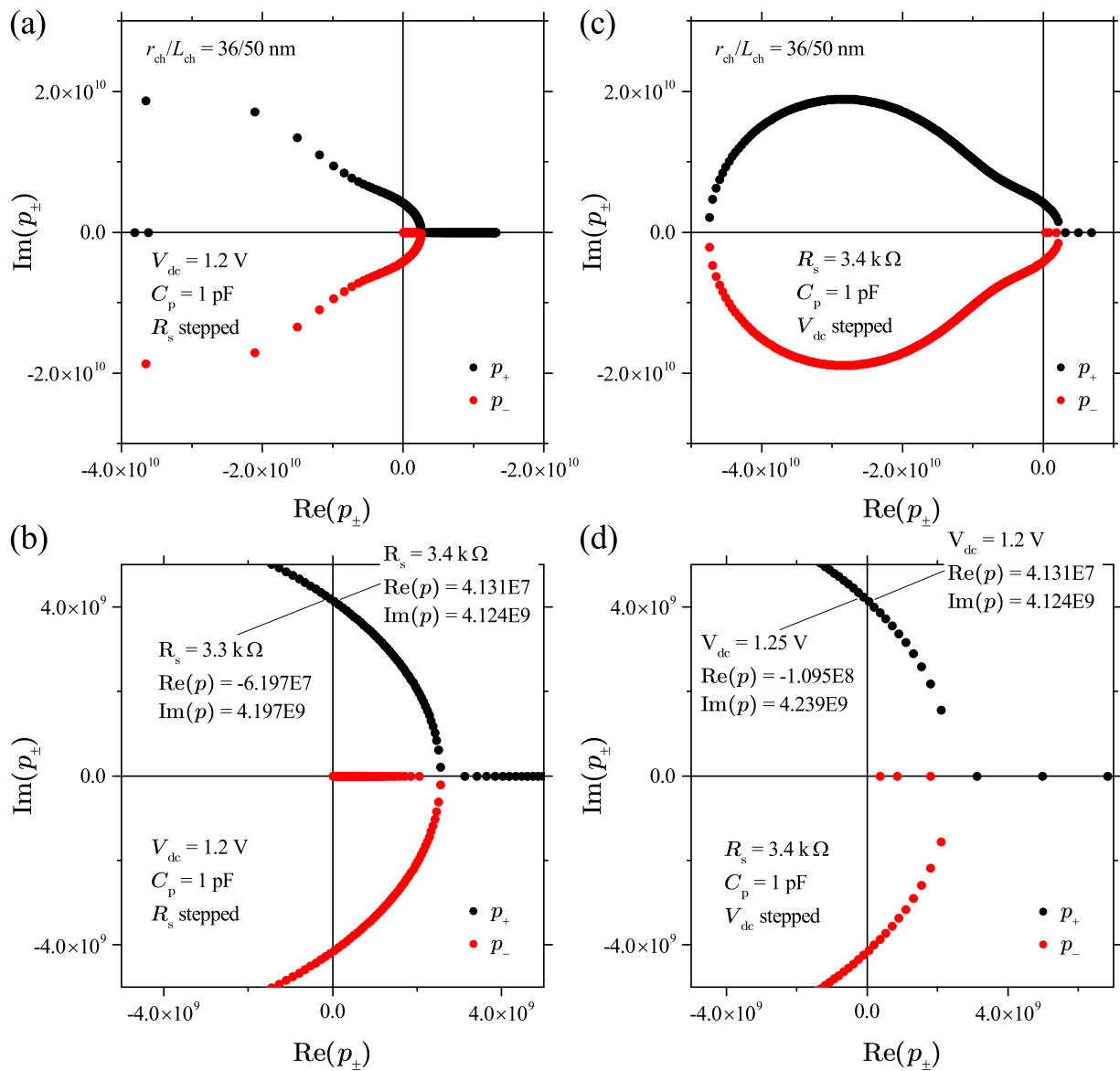


FIGURE 21

(A) Nyquist plot of $\text{Im}(p_{\pm})$ vs $\text{Re}(p_{\pm})$ for the pair of poles p_{\pm} of the small-signal transfer function $H(s; Q)$ of the midsize VO_2 Mott memristor PA oscillator with $C_p = 1$ pF, $V_{dc} = 1.2$ V, and R_s stepped from 100Ω to $27 \text{ k}\Omega$ at a $100\text{-}\Omega$ interval. (B) Zoomed-in view of (A), showing that increasing R_s from $3.3 \text{ k}\Omega$ to $3.4 \text{ k}\Omega$ turns $\text{Re}(p_{\pm})$ from negative to positive. (C) Nyquist plot of the same PA oscillator with $R_s = 3.4 \text{ k}\Omega$, $C_p = 1$ pF, and V_{dc} stepped from 0.55 V to 13.5 V at a 50-mV interval. (D) Zoomed-in view of (C), showing that increasing V_{dc} from 1.2 V to 1.25 V turns $\text{Re}(p_{\pm})$ from positive to negative.

the critical points from the load line analysis $V_{dc} = v_0 + i_0 R_s$ is superimposed to the color-scale map as the border line between the LP and EOC regions. Now, this 2D map can be referred to as a *phase diagram for complexity* for the second-order system. The procedure is then repeated at different C_p values to observe how the LA and LP regions evolve as C_p is adjusted. Figure 22 shows four 2D color-scale maps of $\arg(p_+)$ for the midsize VO_2 Mott memristor PA oscillator at $C_p = 0.1$ pF (a), 1 pF (b), 10 pF (c), and 100 pF (d), respectively.

We consider Figure 22A as an example to discuss their common characteristics. From the complex domain aspect, $\arg(p_+)$ has three distinctive regions if one navigates along the top right to bottom

left diagonal. At small V_{dc} and large R_s (the top-right pink region), $\arg(p_+) = 0^\circ$ and p_+ is a positive real number on the $\text{Re}+$ axis. At larger V_{dc} and smaller R_s , p_+ is a complex number (the middle colored region) in either the first quadrant (LA\EOC) or the second quadrant (EOC), divided by the 90° contour line. At even larger V_{dc} and smaller R_s , $\arg(p_+) = 180^\circ$ and p_+ is a negative real number on the $\text{Re}-$ axis. A notable feature is that all the borderlines between adjacent regions are straight lines that extend from the top left to the bottom right. Despite their appearance, they do not intersect at a common point if extrapolated toward the top-left direction. Note that the borderline separating the LP and EOC regions (dashed white line) does not vary with C_p .

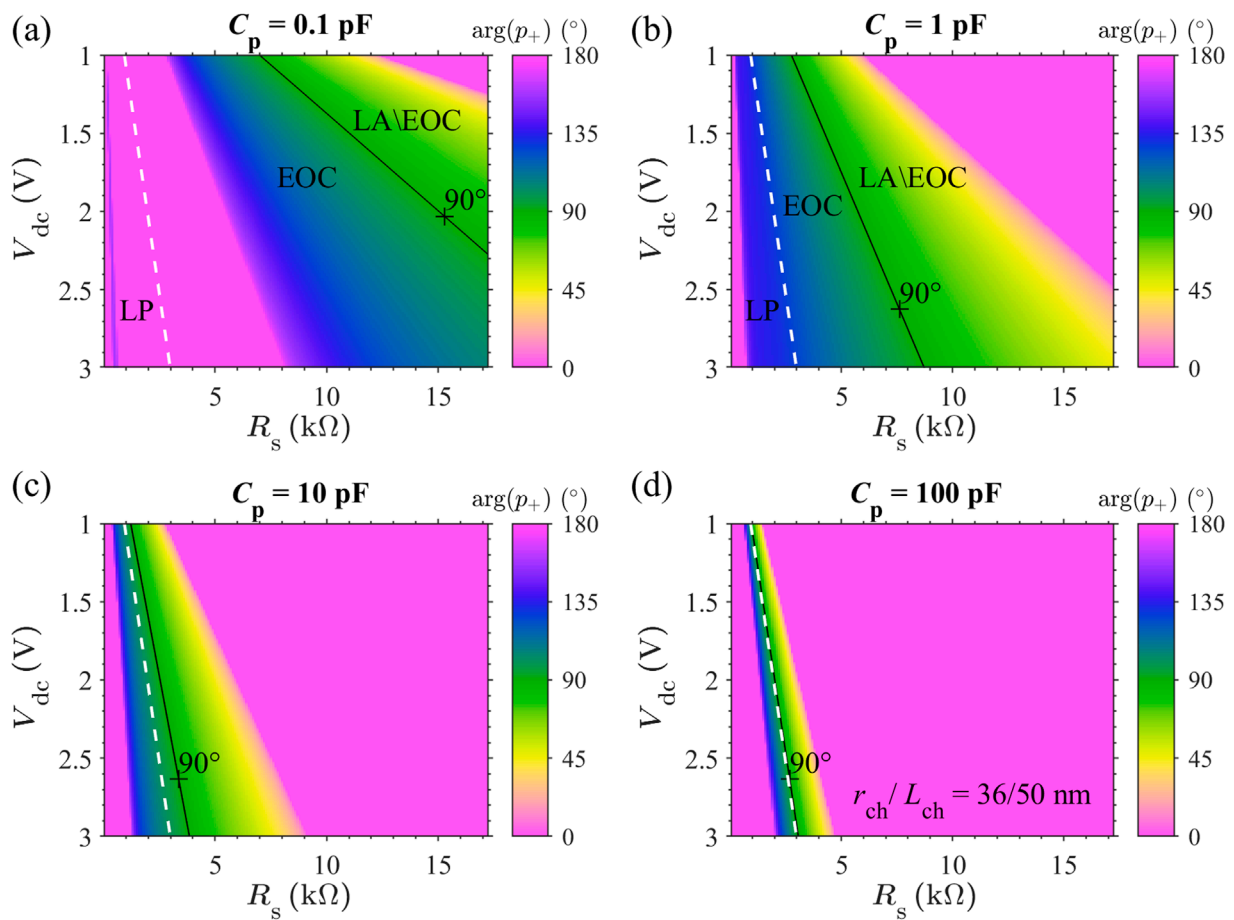


FIGURE 22 2D color-scale maps of $\arg(p_+)(R_s, V_{dc})$, argument of the p_+ pole of $H(s; Q)$, with R_s and V_{dc} as the x and y coordinates, respectively, for the midsize VO_2 Mott memristor PA oscillator at (A) $C_p = 0.1$ pF, (B) $C_p = 1$ pF, (C) $C_p = 10$ pF, and (D) $C_p = 100$ pF, respectively. In each plot, the LA\EOC region ($\text{Re}(p_+) > 0$) and the EOC region ($\text{Re}(p_+) < 0$ and meets the fourth LA criterion) are separated by the 90° contour line (solid black line marked by “+”). The LP region ($\text{Re}(p_+) < 0$ and fails the fourth LA criterion) and the EOC region are separated by the straight line $V_{dc} = v_0 + i_0 R_s$ derived from the load line analysis (dashed white line). Here $i_0 = 971.18 \mu\text{A}$ and $v_0 = 0.0973$ V. We use a cyclic color map with four distinct colors to allow four orientations or phase angles to be visualized. Both $\arg(p_+) = 0^\circ$ and $\arg(p_+) = 180^\circ$ are shown with the same color (pink).

The effect of C_p can be observed by comparing the four color-scale maps. As C_p increases from 0.1 pF to 10 pF, the $\arg(p_+) = 90^\circ$ borderline rotates clockwise, and the rotation stalls as C_p further increases to 100 pF. The $\arg(p_+) = 0^\circ$ (positive real) region at the top right corner continuously expands with an increase in C_p , while the complex region shrinks with an increase in C_p . The $\arg(p_+) = 180^\circ$ (negative real) region at the bottom left corner initially shrinks significantly as C_p increases from 0.1 pF to 1 pF, and then, it recovers a little as C_p further increases. The size of LP region remains unchanged as C_p increases, while the size of EOC region gets compressed. At $C_p = 100$ pF, the EOC region barely exists as the two borderlines almost merge.

Using the element combination approach, we have shown that when a Mott memristor is coupled to a capacitor, both the system's dimension and its dynamical complexity increases — a new LA\EOC region emerges to host instabilities and persistent oscillations. One can also examine the case of an inductively coupled Mott memristor, e.g., connecting an external inductor in parallel with a Mott memristor. It is found that the poles of the transfer

function of such a composite circuit remain in the LHP; thus, the composite circuit does not satisfy the LA criterion to exhibit instabilities or persistent oscillations (Brown et al., 2022b). This is not surprising since an isolated Mott memristor has an inherently inductive reactance.

5.3 Jacobian matrix method

For second or higher-order nonlinear systems, the Jacobian matrix method is a linearization technique that allows local stability analysis near a hyperbolic fixed point. As an introduction in a nutshell, consider an autonomous system of ODEs $\dot{\mathbf{x}} = \mathbf{f}(\mathbf{x})$, where $\dot{\mathbf{x}}$ is the component-wise time derivative for the set of state variables \mathbf{x} . \mathbf{x} corresponds to a point in an open subset of real n -space, $E \subset \mathbb{R}^n$. $\mathbf{f}: E \rightarrow \mathbb{R}^n$ is a differentiable function that describes the dynamics of \mathbf{x} . \mathbf{f} is also called a vector field since the mapping from \mathbf{x} to $\mathbf{f}(\mathbf{x})$ assigns a vector. For a 2D (planar) system described by $\frac{dx}{dt} = f(x, y)$ and $\frac{dy}{dt} = g(x, y)$, $\mathbf{f}(\mathbf{x}) = (f(x, y), g(x, y))$ can be visualized using

a vector based at the point (x, y) , whose x - and y -components are $f(x, y)$ and $g(x, y)$, respectively. The set of solutions $\phi(t, \mathbf{x}_0)$ of the initial value problem $\dot{\mathbf{x}} = \mathbf{f}(\mathbf{x})$, with $\mathbf{x}(0) = \mathbf{x}_0 \in E$, is called the flow of the ODE or the flow of the vector field \mathbf{f} . For each initial condition \mathbf{x}_0 , $\phi(t, \mathbf{x}_0)$ provides the trajectory of a unique solution of the ODE, which is called the orbit of \mathbf{x} under ϕ .

In autonomous systems, \mathbf{f} does not explicitly depend on time. If $\mathbf{f}(\mathbf{x}_Q) = 0$, i.e., its time derivative is 0, then \mathbf{x}_Q is a fixed point. The Jacobian matrix $D\mathbf{f}$, or simply Jacobian, is the matrix of all the first-order partial derivatives of $\mathbf{f}(\mathbf{x})$. The Hartman–Grobman theorem and the stable manifold theorem guarantee that the local qualitative behavior of a nonlinear system $\dot{\mathbf{x}} = \mathbf{f}(\mathbf{x})$ near a hyperbolic fixed point \mathbf{x}_Q is determined by a linear system $\dot{\mathbf{x}} = A\mathbf{x}$, where $A = D\mathbf{f}(\mathbf{x}_Q)$ is the Jacobian of \mathbf{f} at \mathbf{x}_Q . In other words, the flow of a nonlinear system is topologically conjugate to that of its linearized system in some neighborhood of a fixed point, provided the fixed point is hyperbolic. If the Jacobian is a square matrix and none of the eigenvalues of $D\mathbf{f}(\mathbf{x}_Q)$ is a pure imaginary number, then the fixed point is hyperbolic, and its stability can be told by the signs of the real parts of the eigenvalues, as will be elaborated later.

Next, we consider the Jacobian matrix approach to analyze the local stability of a Mott memristor PA oscillator. This second-order system is described by Equations 55–57.

$$v = R_{ch}(x) i_M, \tag{55}$$

$$\frac{dx}{dt} = f_x(x, i_M), \tag{56}$$

$$\frac{dv}{dt} = \frac{1}{C_p} \left(\frac{V_{dc} - v}{R_s} - i_M \right), \tag{57}$$

where $f_x(x, i_M)$ and $R_{ch}(x)$ are the kinetic and memristance functions of the memristor M , respectively. i_M is the current flowing through M . Substituting it with $v/R_{ch}(x)$, we obtain the two coupled ODEs (Equations 58, 59) that describe the system dynamics.

$$\frac{dx}{dt} \triangleq f(x, v) = f_x \left(x, \frac{v}{R_{ch}(x)} \right), \tag{58}$$

$$\frac{dv}{dt} \triangleq g(x, v) = \frac{1}{C_p} \left(\frac{V_{dc} - v}{R_s} - \frac{v}{R_{ch}(x)} \right). \tag{59}$$

In a vector form, the system is described as $\dot{\mathbf{x}} = \mathbf{f}(\mathbf{x})$. Here, $\mathbf{x} = [x, v]^T$ is the state variable vector, and $\mathbf{f}(\mathbf{x}) = [f(x, v), g(x, v)]^T$ is the differentiable function that describes the dynamics of \mathbf{x} . Around a fixed point Q with a coordinate (x_Q, v_Q) , the Jacobian matrix $D\mathbf{f}$ of the system is a 2×2 matrix of all the first-order partial derivatives of $\mathbf{f}(\mathbf{x})$ that takes the following form:

$$D\mathbf{f}|_Q = \begin{bmatrix} \xi_{11} & \xi_{12} \\ \xi_{21} & \xi_{22} \end{bmatrix} = \begin{bmatrix} \left. \frac{\partial f(x, v)}{\partial x} \right|_Q & \left. \frac{\partial f(x, v)}{\partial v} \right|_Q \\ \left. \frac{\partial g(x, v)}{\partial x} \right|_Q & \left. \frac{\partial g(x, v)}{\partial v} \right|_Q \end{bmatrix}. \tag{60}$$

The four elements of the Jacobian matrix are derived as follows:

$$\xi_{11} = \left. \frac{\partial f(x, v)}{\partial x} \right|_Q = b_{11}(Q) - \frac{b_{12}(Q) a_{11}(Q)}{R_{ch}(x_Q)}, \tag{61}$$

$$\xi_{12} = \left. \frac{\partial f(x, v)}{\partial v} \right|_Q = \frac{b_{12}(Q)}{R_{ch}(x_Q)}, \tag{62}$$

$$\xi_{21} = \left. \frac{\partial g(x, v)}{\partial x} \right|_Q = \frac{a_{11}(Q)}{R_{ch}(x_Q) C_p}, \tag{63}$$

$$\xi_{22} = \left. \frac{\partial g(x, v)}{\partial v} \right|_Q = - \left(\frac{1}{R_s C_p} + \frac{1}{R_{ch}(x_Q) C_p} \right). \tag{64}$$

The eigenvalues of the Jacobian around a fixed point Q derived through Equations 60–64 are calculated by solving its characteristic equation that can be expanded to a quadratic polynomial.

$$(D\mathbf{f} - \lambda I)|_Q = \lambda^2 - \text{tr}(D\mathbf{f})\lambda + \det(D\mathbf{f}) \\ = \lambda^2 - (\xi_{11} + \xi_{22})\lambda + (\xi_{11}\xi_{22} - \xi_{12}\xi_{21}), \tag{65}$$

where I is the identity matrix. $\text{tr}(D\mathbf{f})$ is the trace of the Jacobian matrix, and $\det(D\mathbf{f})$ is its determinant. For simplicity, we use tr and \det to represent them hereafter. Their expressions are derived as follows:

$$\text{tr} = - \left[\omega_1 \left(1 + \frac{R_1}{R_{ch}} \right) + \omega_0 \left(1 + \frac{R_s}{R_{ch}} \right) \right], \tag{66}$$

$$\det = \omega_1 \omega_0 \left(1 + \frac{R_1}{R_{ch}} + \frac{R_s}{R_{ch}} \right), \tag{67}$$

where we define another cutoff frequency $\omega_1 \triangleq (R_1 C_1)^{-1}$, in addition to the previously defined cutoff frequency $\omega_0 = (R_s C_p)^{-1}$, to simplify the expressions.

The two roots λ_+ and λ_- of the characteristic equation (Equation 65) are

$$\lambda_{\pm} = \frac{\text{tr} \pm \sqrt{\text{tr}^2 - 4\det}}{2}. \tag{68}$$

Note that $\lambda_+ + \lambda_- = \text{tr}$ and $\lambda_+ \lambda_- = \det$, i.e., trace is the sum of eigenvalues, and determinant is the product of them. The discriminant $\text{tr}^2 - 4\det$ of the characteristic equation in the expanded form is

$$\text{tr}^2 - 4\det = \omega_1^2(1 + \gamma_1)^2 + \omega_0^2(1 + \gamma_s)^2 - 2\omega_1\omega_0[(1 - \gamma_1)\gamma_s + (1 + \gamma_1)], \tag{69}$$

where we define two dimensionless resistance ratios $\gamma_1 \triangleq \frac{R_1}{R_{ch}}$ and $\gamma_s \triangleq \frac{R_s}{R_{ch}}$ to simplify the expression.

5.4 Trace–determinant plane classification

For a 2D homogeneous linear system $\dot{\mathbf{x}} = A\mathbf{x}$, the parameter space of a trace–determinant (tr–det) plane allows the qualitative classification of its fixed points. In this study, a homogeneous linear system is defined in contrast to a nonhomogeneous linear system $\dot{\mathbf{x}} = A\mathbf{x} + \mathbf{h}(t)$, which includes a vector of functions $\mathbf{h}(t)$ that are independent of solutions and their derivatives. For a 2D nonlinear system, after linearization, one needs to be cautious when applying the tr–det plane method since linearization may change the nature of its fixed points, especially along the borderlines on the tr–det plane. Here, we examine the tr–det plane method on a linearized Mott memristor PA oscillator to check whether one can gain some insights into the original nonlinear system.

TABLE 3 Trace–determinant (tr–det) plane classification of fixed points for 2D linear homogeneous systems. In the tr–det plane, the only stable region is the closed second quadrant, i.e., $\text{tr} \leq 0$ and $\text{det} \geq 0$.

Determinant	Trace	Eigenvalues	Stability and class	ID
$\text{det} < 0$	Any	$\lambda_+ > 0 > \lambda_-$	Unstable saddle point	1
$\text{det} = 0$	$\text{tr} < 0$	$\lambda_+ = 0, \lambda_- < 0$	Stable line of fixed points	2
	$\text{tr} = 0$	$\lambda_+ = \lambda_- = 0$	Parallel lines or entire plane	3
	$\text{tr} > 0$	$\lambda_+ > 0, \lambda_- = 0$	Unstable line of fixed points	4
$\text{det} > 0$	$\text{tr} < -\sqrt{4\text{det}}$	$0 > \lambda_+ > \lambda_-$	Stable node (sink)	5
	$\text{tr} = -\sqrt{4\text{det}}$	Repeated	Stable degenerate node	6 and 7
		$\lambda_{\pm} = \text{tr}/2 < 0$	(6) or stable star (7)	
	$-\sqrt{4\text{det}} < \text{tr} < 0$	Complex conjugate	Stable spiral sink	8
		$\text{Re}(\lambda_{\pm}) < 0$		
	$\text{tr} = 0$	Complex conjugate	Stable center	9
		$\text{Re}(\lambda_{\pm}) = 0$	(Not asymptotically stable)	
	$0 < \text{tr} < \sqrt{4\text{det}}$	Complex conjugate	Unstable spiral source	10
		$\text{Re}(\lambda_{\pm}) > 0$		
	$\text{tr} = \sqrt{4\text{det}}$	Repeated	Unstable degenerate node	11 and 12
$\lambda_{\pm} = \text{tr}/2 > 0$		(11) or unstable star (12)		
$\text{tr} > \sqrt{4\text{det}}$	$\lambda_+ > \lambda_- > 0$	Unstable node (source)	13	

In a tr–det plane, a coordinate (tr, det) corresponds to a Jacobian matrix with trace tr and determinant det. The location of this point relative to the parabola curve $\text{tr}^2 - 4\text{det} = 0$ determines the geometry of the phase portrait. The sign of the discriminant $\text{tr}^2 - 4\text{det}$ in Equation 69 divides the eigenvalues of Df into the following regions.

- a) If $\text{tr}^2 - 4\text{det} > 0$, λ_+ and λ_- are real and distinct.
- b) If $\text{tr}^2 - 4\text{det} < 0$, λ_+ and λ_- are complex conjugates with a nonzero imaginary part.
- c) If $\text{tr}^2 - 4\text{det} = 0$, λ_+ and λ_- are real and repeated (identical).

Within each of these three regions, the tr–det plane further classifies the dynamics and stability of isolated or non-isolated fixed points as enumerated below. The numbers within () that appear out of order are class identifiers (IDs), provided in Table 3, which is a tabulated summary of the tr–det plane classification. It is notable that the only stable region in the tr–det plane is the closed second quadrant, i.e., $\text{tr} \leq 0$ and $\text{det} \geq 0$. If a fixed point is stable, its eigenvalues λ_+ and λ_- must both be negative real: $(\lambda_+, \lambda_-) \leq 0$ or they are complex conjugates with a negative real part: $\text{Re}(\lambda_{\pm}) \leq 0$.

Region (a) with two real and distinct eigenvalues $\lambda_+ \neq \lambda_-$

- (1) $\lambda_+ > 0 > \lambda_-$: unstable saddle point
- (2) $\lambda_+ = 0, \lambda_- < 0$: stable line of non-isolated fixed points
- (4) $\lambda_+ > 0, \lambda_- = 0$: unstable line of non-isolated fixed points
- (5) $0 > \lambda_+ > \lambda_-$: stable sink

- (13) $\lambda_+ > \lambda_- > 0$: unstable source

Region (b) with a pair of complex conjugate eigenvalues $\lambda_{\pm} = \alpha \pm \beta i, \beta \neq 0$

- (8) $\text{Re}(\lambda_{\pm}) < 0$: stable spiral sink
- (9) $\text{Re}(\lambda_{\pm}) = 0$: stable center (not asymptotically stable)
- (10) $\text{Re}(\lambda_{\pm}) > 0$: unstable spiral source

A center is a non-hyperbolic fixed point since it has a pair of pure imaginary eigenvalues; therefore, the Hartman–Grobman theorem is not applicable. It is stable (or Lyapunov stable) but not asymptotically stable. A solution that starts near a center remains close to it but never converges over time since non-zero pure imaginary eigenvalues correspond to periodic solutions that oscillate without damping.

Region (c) with real and repeated eigenvalues: $\lambda_{\pm} = \lambda$

- (3) $\lambda = 0$: parallel lines of non-isolated fixed points or the entire plane
- (6) $\lambda < 0$ and is incomplete: stable degenerate sink
- (7) $\lambda < 0$ and is complete: stable star sink
- (11) $\lambda > 0$ and is incomplete: unstable degenerate source
- (12) $\lambda > 0$ and is complete: unstable star source

Here, a nonzero real and repeated eigenvalue is considered complete if it has two linearly independent eigenvectors, making the fixed point (star) a proper node. Otherwise, if the eigenvalue is

incomplete (has only one eigenvector), the fixed point is classified as a degenerate or improper node.

For a linearized 2D nonlinear system, the tr-det plane predictions are always accurate for classes 1, 5, 8, 10, and 13. While predictions for the other eight classes may not be accurate, they correctly determine the stability of classes 6, 7, 11, and 12. Prediction for class 9 is accurate if the system is conservative.

Now, we apply the tr-det plane analysis for the 2D nonlinear system of the VO₂Mott memristor PA oscillator. This system has been analyzed previously using an element combination approach by considering a Mott memristor M_{and} and a capacitor C_p in parallel as a composite second-order nonlinear element Z_{CM} , which is connected to a resistor R_s in series. The small-signal transfer function of this 2D nonlinear system has two poles p_{\pm} that form a pair of complex conjugate in part of the circuit parameter space. The Nyquist plots in Figures 21A, B show the evolution of the positions of p_{\pm} as R_s is varied while keeping $C_p = 1$ pF and $V_{\text{dc}} = 1.2$ V unchanged. Increasing R_s from 3.3 k Ω to 3.4 k Ω flips the sign of $\text{Re}(p_{\pm})$ from negative to positive and produces a crossover from EOC to LA\EOC as per Chua's LA theorem.

Instead of element combination, we now apply the tr-det plane analysis of the Jacobian linearized 2D PA oscillator system. We show that the 2D tr-det plane method elucidates the nature of this crossover in local activity to be a bifurcation, which changes the stability of an isolated fixed point. Figure 23A plots the (tr, det) plane that is geometrically divided into different regions by the tr- and det-axes and the $\text{det} = \text{tr}^2/4$ parabola. Each of them is labeled by the class IDs, as listed in Table 3. It shows a locus of (tr, det) calculated from the Jacobian matrix of the midsize VO₂ Mott memristor PA oscillator around its fixed points by fixing $C_p = 1$ pF, $V_{\text{dc}} = 1.2$ V, and stepping R_s from 100 Ω to 17.2 k Ω at 100 Ω interval. The (tr, det) points for $100 \Omega \leq R_s \leq 600 \Omega$ outside the plotted area are all located above the $\text{det} = \text{tr}^2/4$ parabola within the same stable spiral sink (class 8) region. The trajectory of (tr, det) formed by varying R_s is nonlinear and convex-shaped. Increasing R_s moves (tr, det) toward the region of an unstable spiral source (class 10) in the first quadrant and produces a bifurcation as it crosses the positive det axis. At $R_s > 7.5$ k Ω , (tr, det) of the fixed point crosses the $\text{det} = \text{tr}^2/4$ parabola into the unstable source (class 13) region, but its stability remains unchanged. Therefore, R_s is clearly a bifurcation parameter for the 2D PA oscillator.

Figure 23B is a zoomed-in view of (a). It shows that increasing R_s from 3.3 k Ω to 3.4 k Ω produces a stability-change bifurcation from a stable spiral sink (class 8) to an unstable spiral source (class 10), both belonging to Region (b) of $\text{tr}^2 - 4\text{det} < 0$ that has complex conjugate Jacobian eigenvalues. At a critical value of $R_s^* = 3359.5 \Omega$, (tr, det) is located exactly on the $\text{tr} = 0$ axis as the borderline between the unstable first quadrant and stable second quadrant. The tr-det plane predicts that the fixed point is a stable center (class 9). We have learned that predictions about a spiral sink (class 8) and a spiral source (class 10) are always correct for 2D nonlinear systems, but the prediction about a center (class 9) is unproven since a 2D PA oscillator is not a conservative system.

In Figure 23C, we plot the (tr, det) locus for the Jacobian of the same PA oscillator around its fixed points, this time by fixing $R_s = 3.4$ k Ω , $C_p = 1$ pF, and stepping V_{dc} from 1 V to 3 V at a 10-mV interval. It shows a similarly shaped convex trajectory of (tr, det) as the case for stepping R_s . However, the effect of V_{dc} is opposite to that

of R_s a larger V_{dc} moves (tr, det) toward the stable spiral sink (class 8) region in the second quadrant. Figure 23D is a zoomed-in view of (c), showing that increasing V_{dc} from 1.21 V to 1.22 V produces a stability-change bifurcation from an unstable spiral source (class 10) to a stable spiral sink (class 8). At a critical value of $V_{\text{dc}}^* = 1.21355$ V, (tr, det) is located exactly on the $\text{tr} = 0$ axis. Therefore, V_{dc} is also a bifurcation parameter for the 2D PA oscillator. The fact that the critical values of bifurcation parameters R_s and V_{dc} , as determined by the tr-det plane analysis, closely match with those obtained from the small-signal Nyquist plot analysis using the element combination approach (see Figure 21) corroborates the validity of both methods.

The parallel capacitor C_p also functions as a bifurcation parameter if R_s and V_{dc} are fixed and C_p is adjusted. Figure 24A shows the plots of four loci of the Jacobian (tr, det) for the midsize VO₂ Mott memristor PA oscillator, with $V_{\text{dc}} = 1.2$ V and R_s fixed at 3 k Ω , 5 k Ω , 7 k Ω , and 9 k Ω , respectively. For each locus, we step up C_p in the sequence of 10 fF, 20 fF, 50 fF, 0.1 pF, 0.2 pF, 0.5 pF, 1 pF, 2 pF, 5 pF, and 10 pF. Similar to the case of varying R_s , increasing C_p also moves (tr, det) from the stable second quadrant into the unstable first quadrant. However, the (tr, det) locus is linear instead of convex-shaped. Equations 66, 67 together predict a slope of $-\omega_1 [1 + R_1 / (R_{\text{ch}} + R_s)]$ for the (tr, det) locus if C_p is varied, which matches exactly with the linear regression slopes of the four loci. Equation 67 also predicts that (tr, det) asymptotically approaches the positive tr axis as one continuously increases C_p but never reaches it. Open symbols highlight the critical C_p^* values for the stability-change bifurcation as the (tr, det) loci intercept the positive det axis. It can be observed that a larger fixed R_s would shift the (tr, det) locus upward and decrease its critical C_p^* value. Figure 24B shows the plots of the dependence of critical C_p^* on R_s in a log-log fashion for three different V_{dc} settings at 1.0 V, 1.2 V, and 1.4 V. One can infer that $C_p^*(R_s)$ follows a power law with an exponent close to -2.5 . For the trace at $V_{\text{dc}} = 1.2$ V, we added the point of $R_s = 3359.5 \Omega$. The power law predicts a $C_p^* = 1$ pF, which is consistent with the critical (R_s^*, C_p) value for the same bifurcation in the case of varying R_s at a fixed $C_p = 1$ pF (see Figure 23B).

6 Global analysis of reactively coupled Mott memristors: two-dimensional relaxation oscillator

6.1 Nullclines and direction field

The local analysis techniques we have discussed so far require a foreknowledge of the fixed points for a 2D nonlinear system. Global analyses, such as nullclines in the phase space of state variables, can be used to analyze a nonlinear system of ODEs and locate its fixed points. For a 2D or planar system, the x - (or y -) nullcline is defined as the set of points in the phase plane of (x, y), where the time derivative of x (or y) vanishes. Therefore, the vector field is vertical on the x -nullcline and horizontal on the y -nullcline. Together, they partition \mathbb{R}^2 into different open regions, each characterized by differences in the signs of their time derivatives. One can then determine the direction of the vector field in each region. The intersections of the x - and y -nullclines yield the fixed points. A direction field (also called a slope field) is the scaled version of a vector field, with all the vector

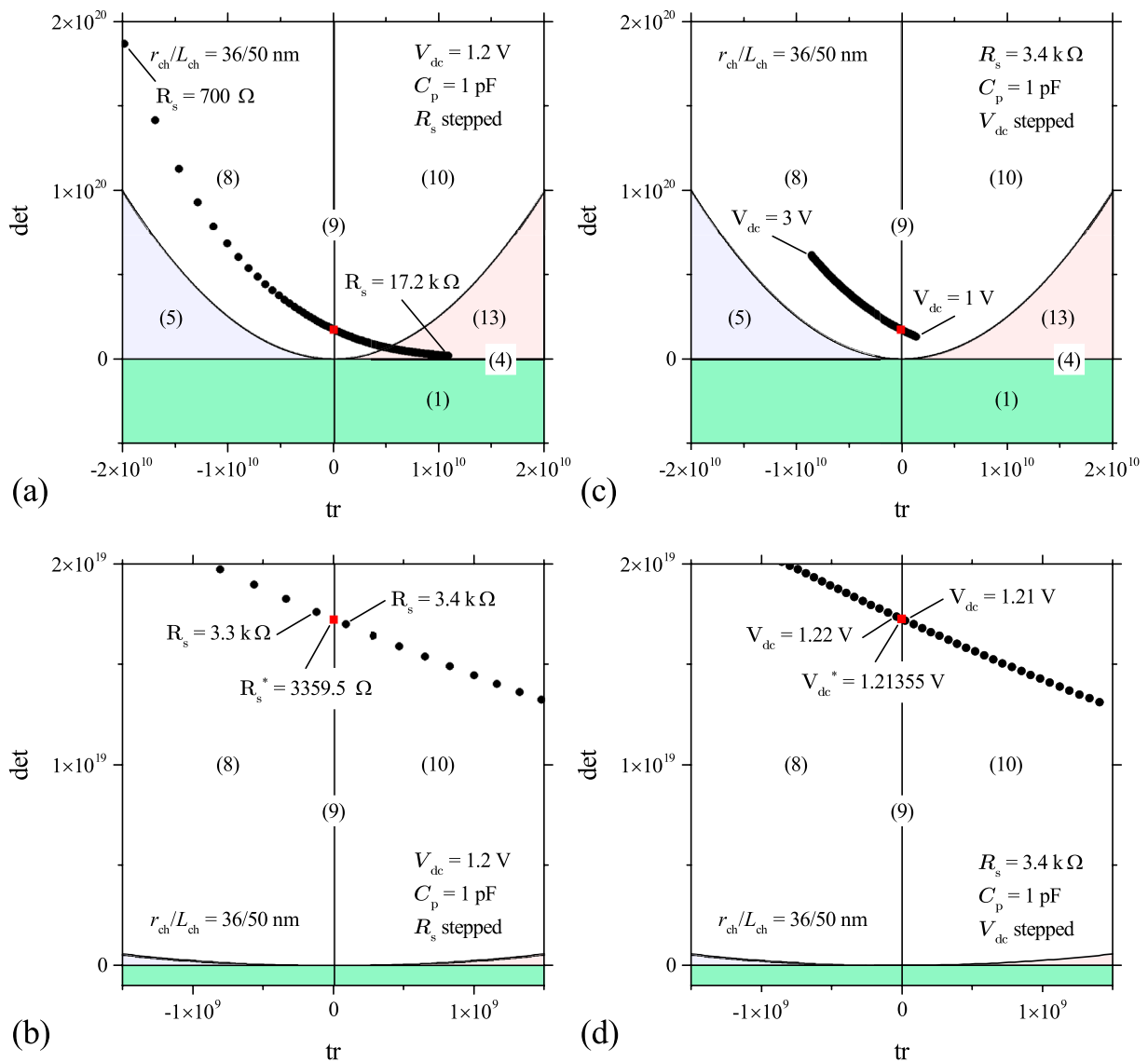


FIGURE 23 (A) Trace–determinant plane showing the (tr, det) locus for the Jacobian of the midsize VO_2 Mott memristor PA oscillator with $C_p = 1$ pF, $V_{dc} = 1.2$ V, and bifurcation parameter R_s stepped from 100Ω to 17.2 k Ω at a $100\text{-}\Omega$ interval. (B) Zoomed-in view of (A), showing that increasing R_s from 3.3 k Ω to 3.4 k Ω results in a bifurcation from a stable spiral sink (class 8) to an unstable spiral source (class 10). At $R_s^* = 3359.5 \Omega$, the fixed point is a stable center (class 9) located on the $tr = 0$ axis. (C) The (tr, det) locus for the Jacobian of the same PA oscillator, with $R_s = 3.4$ k Ω , $C_p = 1$ pF, and bifurcation parameter V_{dc} stepped from 1 V to 3 V at a 10-mV interval. (D) Zoomed-in view of (C), showing that increasing V_{dc} from 1.21 V to 1.22 V produces a bifurcation from an unstable spiral source (class 10) to a stable spiral sink (class 8). At $V_{dc}^* = 1.21355$ V, the fixed point is a stable center (class 9) located on the positive det axis.

lengths normalized to unity. In the 2D phase plane, superimposing the x - and y -nullclines onto the direction field reveals fixed points and provides insights into their dynamical classification and the orbits of solutions.

For the case of a 2D Mott memristor PA oscillator, the x -nullcline (x_0, v_0) is the locus of points, where the time derivative of the state variable x for the memristor M vanishes

$$f(x_0, v_0) = f_x \left(x_0, \frac{v_0}{R_{ch}(x_0)} \right) = 0, \tag{70}$$

which can be rewritten as

$$v_0 = \left[-A(1 + Bx_0^2) \frac{\ln x_0}{C} \right]^{-0.5}. \tag{71}$$

Since (x_0, v_0) are steady states of M , the x -nullcline only depends on the internal characteristics of M and is independent of the external circuit parameters including R_s , C_p , and V_{dc} . It remains the same as that of an isolated M (see Figure 7C).

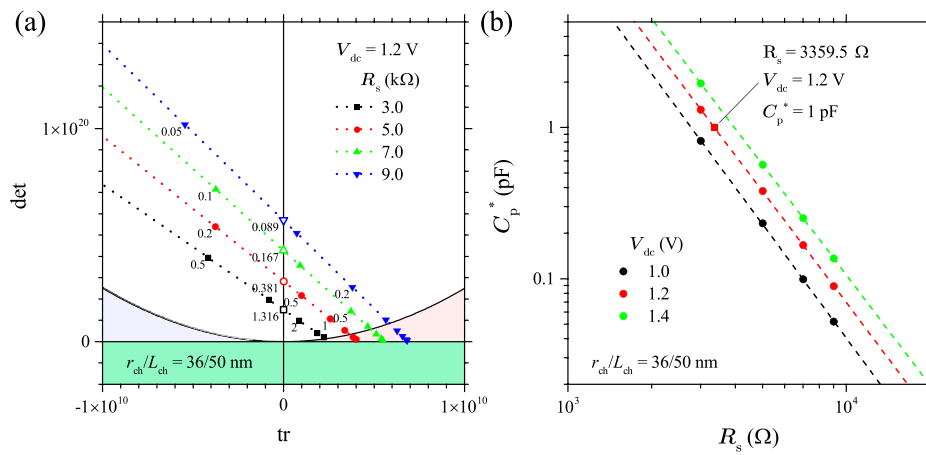


FIGURE 24 (A) Trace–determinant plane showing four (tr, det) loci for the Jacobian of the midsize VO₂ Mott memristor PA oscillator with $R_s = 3\text{ k}\Omega$, $5\text{ k}\Omega$, $7\text{ k}\Omega$, and $9\text{ k}\Omega$, respectively, all at $V_{dc} = 1.2\text{ V}$. For each locus, increasing C_p (from 10 fF to 10 pF in the present case) moves the Jacobian (tr, det) along a linear trajectory from the stable second quadrant into the unstable first quadrant, which then asymptotically approaches the positive tr axis. The open symbol that intercepts the positive det axis shows the critical C_p^* for the source–sink bifurcation. (B) Log–log plot of the critical C_p^* vs R_s for three cases of $V_{dc} = 1.0\text{ V}$, 1.2 V and 1.4 V . Dashed lines are power-law fits $C_p^* = aR_s^b$, with an exponent $b \approx -2.5$. The square (red) shows that $C_p^* = 1\text{ pF}$ if $R_s = 3359.5\ \Omega$, which is consistent that shown in Figure 23B.

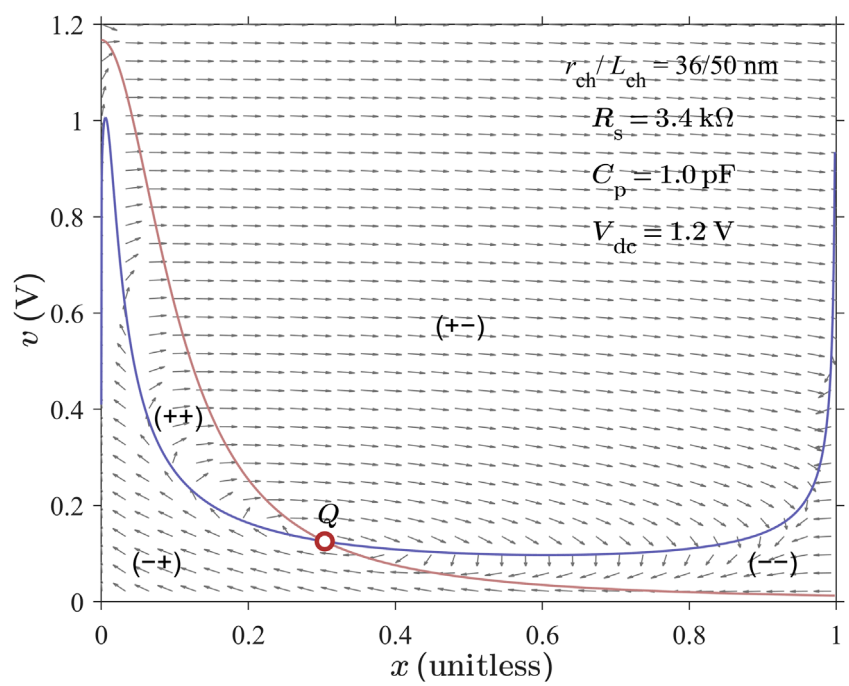


FIGURE 25 Nullclines and direction field (arrowheads) in the phase plane of the midsize VO₂ Mott memristor PA oscillator with $R_s = 3.4\text{ k}\Omega$, $C_p = 1.0\text{ pF}$, and $V_{dc} = 1.2\text{ V}$. Under these conditions, the 2D nonlinear system has one fixed point $(x_Q, v_Q) = (0.30396, 0.12564)$ at the single intersection of the x - (blue-violet line) and v - (brown line) nullclines. Based on the signs of dx/dt and dv/dt , the x - and v -nullclines partition the \mathbb{R}^2 plane into four open regions labeled as (+ +), (+ -), (- +), and (- -), respectively.

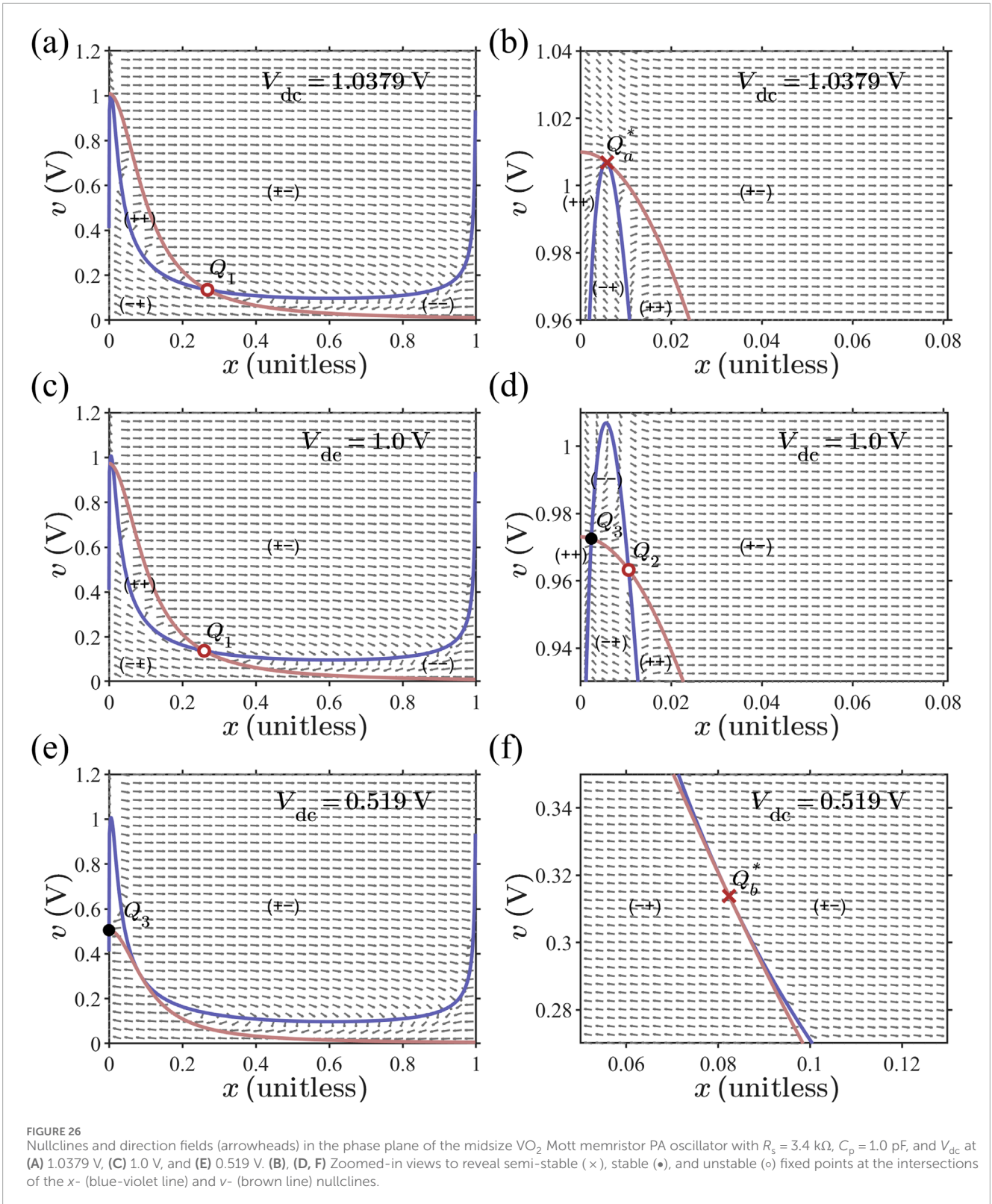
The v -nullcline (x_1, v_1) is the locus of points where the time derivative of the state variable v vanishes.

$$g(x_1, v_1) = \frac{1}{C_p} \left(\frac{V_{dc} - v_1}{R_s} - \frac{v_1}{R_{ch}(x_1)} \right) = 0, \tag{72}$$

which can be rewritten as

$$v_1 = \frac{V_{dc}}{1 + R_s A (1 + Bx_1^2)}. \tag{73}$$

Since v is the voltage across the capacitor C_p and M in parallel, the charge stored on the capacitor does not change over time; thus, there



is no current flowing through it. Therefore, R_s in series with M forms a voltage divider. The v -nullcline depends on V_{dc} and R_s , but it is independent of C_p .

The intersections of the x - and y -nullclines derived through Equations 70–73 are the fixed points Q of the 2D system, where both x - and v -derivatives vanish.

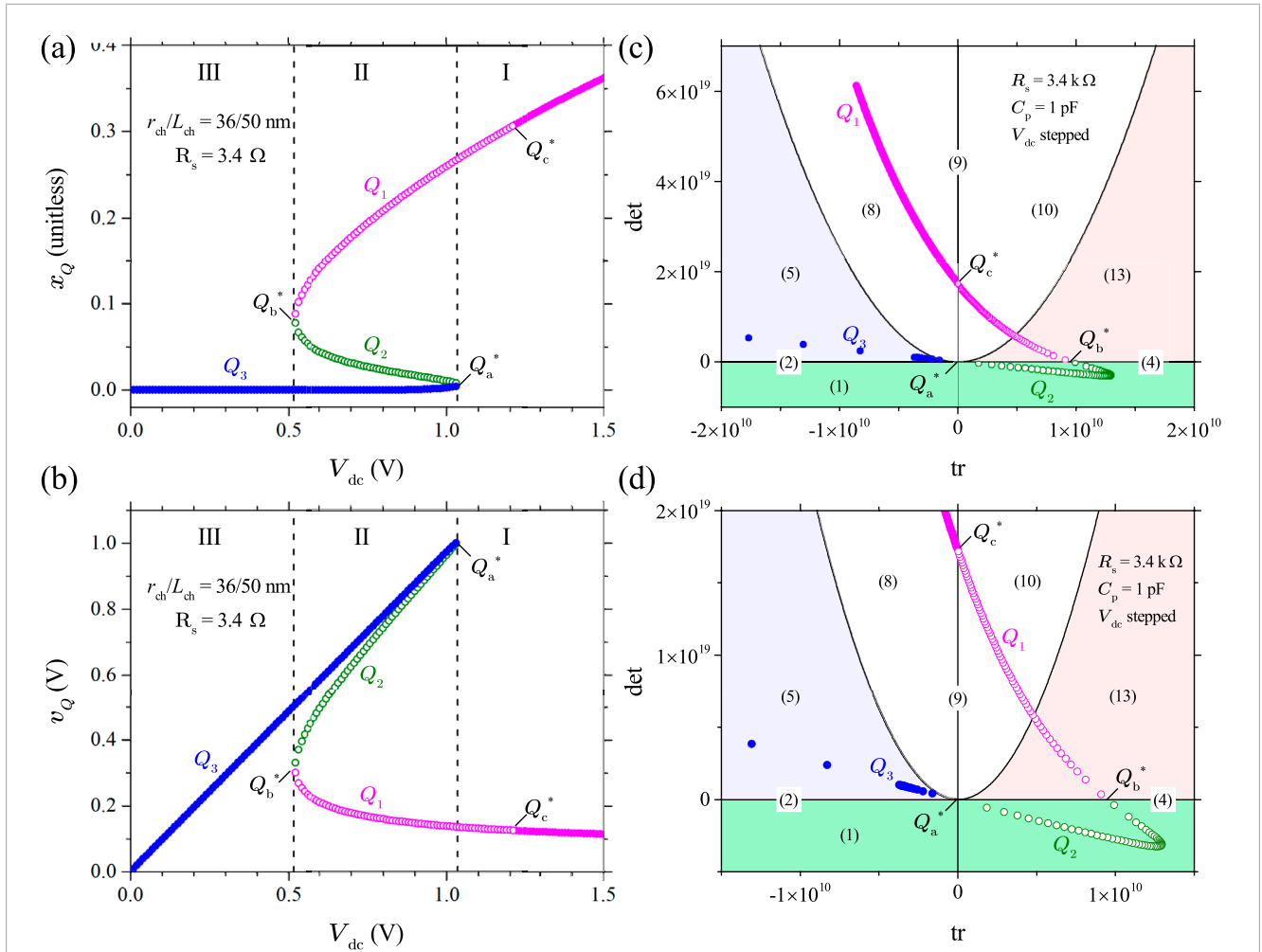


FIGURE 27 Bifurcation diagrams showing V_{dc} dependences of **(A)** x_Q and **(B)** v_Q of the fixed point (x_Q, v_Q) for the midsize VO₂ Mott memristor PA oscillator, as determined by the nullclines method. $R_s = 3.4 \text{ k}\Omega$ and C_p is arbitrary. Stable (unstable) fixed points are represented by solid (open) circles. As V_{dc} is stepped from 3 V to 0 V at a 0.01 V interval (plotted up to 1.5 V for clarity), initially (region I), the 2D system has only one fixed point Q_1 , which undergoes a stability-change bifurcation at $V_{dc} = 1.21355 \text{ V}$ (Q_c^*). A saddle-node bifurcation at $V_{dc} = 1.0379 \text{ V}$ (Q_a^*) creates a pair of fixed points Q_2 and Q_3 in region II. At $V_{dc} = 0.519 \text{ V}$ (Q_b^*), another bifurcation occurs as Q_1 and Q_2 coalesce and annihilate each other. For even lower V_{dc} (region III), only one fixed point Q_3 exists. **(C)** (tr, det) loci for the Jacobian of the same fixed points, as shown in **(A, B)**, calculated with $C_p = 1.0 \text{ pF}$. **(D)** Zoomed-in view of **(C)**, showing that Q_a^* is located on the negative tr axis very close to the origin, Q_b^* is on the positive tr axis, and Q_c^* is on the positive det axis.

$$f(x_Q, v_Q) = f_x \left(x_Q, \frac{v_Q}{R_{ch}(x_Q)} \right) = 0, \tag{74}$$

$$g(x_Q, v_Q) = \frac{1}{C_p} \left(\frac{V_{dc} - v_Q}{R_s} - \frac{v_Q}{R_{ch}(x_Q)} \right) = 0. \tag{75}$$

Figure 25 shows the plots of the x - and v -nullclines and direction field in the phase plane of the midsize VO₂ Mott memristor PA oscillator with $R_s = 3.4 \text{ k}\Omega$ and $V_{dc} = 1.2 \text{ V}$. Note that the direction field depends on C_p and is plotted for the case of $C_p = 1.0 \text{ pF}$. Under these conditions, the 2D nonlinear system has just one fixed point $(x_Q, v_Q) = (0.30396, 0.12564)$ at the single intersection of the x -nullcline (blue-violet line) and v -nullcline (brown line) satisfying Equations 74, 75. The x - and v -nullclines partition the phase plane into four open regions, depending on the signs of time derivatives for x and v , labeled as $(++)$, $(+-)$, $(-+)$, and $(--)$, respectively. The direction field (arrowheads) shows a distinct clockwise rotational

pattern around Q , suggesting that the orbit of a solution $(x(t), v(t))$ with an initial condition close to Q would rotate around it in a clockwise manner. Intuitively, if Q were a stable spiral sink, $(x(t), v(t))$ would spiral inward toward it. If Q were an unstable spiral source, $(x(t), v(t))$ would spiral outward. However, it is also possible that $(x(t), v(t))$ forms an isolated periodic orbit, continuously rotating around Q . Additional analyses are required in addition to the studies on the nullclines and direction field to determine whether such a case exists.

Since the location of the v -nullcline varies with V_{dc} and R_s , decreasing V_{dc} will shift it downward with respect to the x -nullcline, which may change the number of intersections between them. To investigate this, Figure 26 presents the three sets of x - and v -nullclines along the direction field for the same model PA oscillator at V_{dc} values of 1.0379 V, 1.0 V and 0.519 V, respectively. Figure 26A and its zoomed-in view (Figure 26B) show the case of $V_{dc} = 1.0379 \text{ V}$. At this critical value of V_{dc} , the v -nullcline becomes tangent

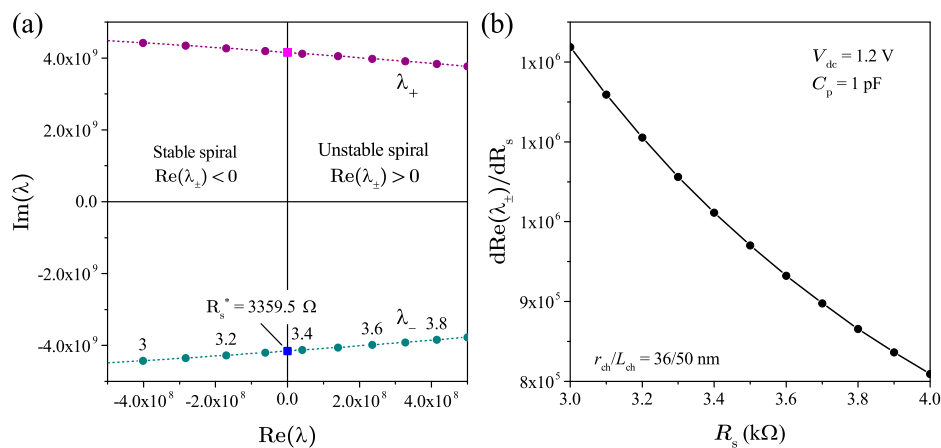


FIGURE 28

Examination of the non-hyperbolicity and transversality conditions for the Hopf bifurcation theorem. **(A)** Loci of the conjugate pair of eigenvalues $\lambda_{\pm}(R_s)$ in the complex plane for the Jacobian of the midsize VO_2 Mott memristor PA oscillator with $C_p = 1 \text{ pF}$, $V_{dc} = 1.2 \text{ V}$, and bifurcation parameter R_s stepped at a 100Ω interval (labeled as k Ω for several λ_{\pm} points). The Jacobian matrix has a stable spiral for $\text{Re}(\lambda_{\pm}) < 0$ and an unstable spiral for $\text{Re}(\lambda_{\pm}) > 0$. At $R_s^* = 3359.5 \Omega$, λ_{\pm} are pure imaginary, and the fixed point is a non-hyperbolic center located on the $\text{tr} = 0$ axis. **(B)** Calculated $d\text{Re}(\lambda_{\pm})/dR_s$ vs R_s , showing that its value is finite and positive for R_s , which ranges from 3.0 k Ω to 4.0 k Ω .

with the x -nullcline near its peak at the PDR-to-NDR crossover $Q_a^* = (0.00589, 1.00681)$, increasing the number of fixed points from one to two.

Further reducing V_{dc} will split Q_a^* into a pair of unstable (Q_2) and stable (Q_3) fixed points, which move apart from each other as V_{dc} further decreases. This is a characteristic of a 2D saddle-node bifurcation. We are already familiar with the 1D case for an isolated Mott memristor (see Figure 6). To illustrate, Figure 26C and its zoomed-in view (Figure 26D) show the case of $V_{dc} = 1.0 \text{ V}$. Now, there are three intersections between the v - and x -nullclines. In addition to the original fixed point $Q_1 = (0.25937, 0.13823)$ located in the NDR region of M , two new fixed points $Q_2 = (0.01064, 0.96326)$ and $Q_3 = (0.00243, 0.97254)$ emerge at very small x values. As a result, the \mathbb{R}^2 plane is now partitioned into six open regions instead of four. The two additional regions are $(++)$ within the PDR region of M and $(--)$ near the PDR-to-NDR transition of M . The direction field reveals that Q_2 is an unstable node, while Q_3 is a stable node at an intersection in the PDR region (insulating state) of M .

Q_1 and Q_2 approach each other as V_{dc} further decreases. Figure 26E and its zoomed-in view (Figure 26F) show that at another critical value of $V_{dc} = 0.519 \text{ V}$, the v -nullcline becomes tangent to the x -nullcline in its NDR region as Q_1 and Q_2 merge into one fixed point Q_b^* . This fixed point disappears if V_{dc} continues to decrease. At $V_{dc} < 0.519 \text{ V}$, only one stable fixed point Q_3 exists in the insulating state of M .

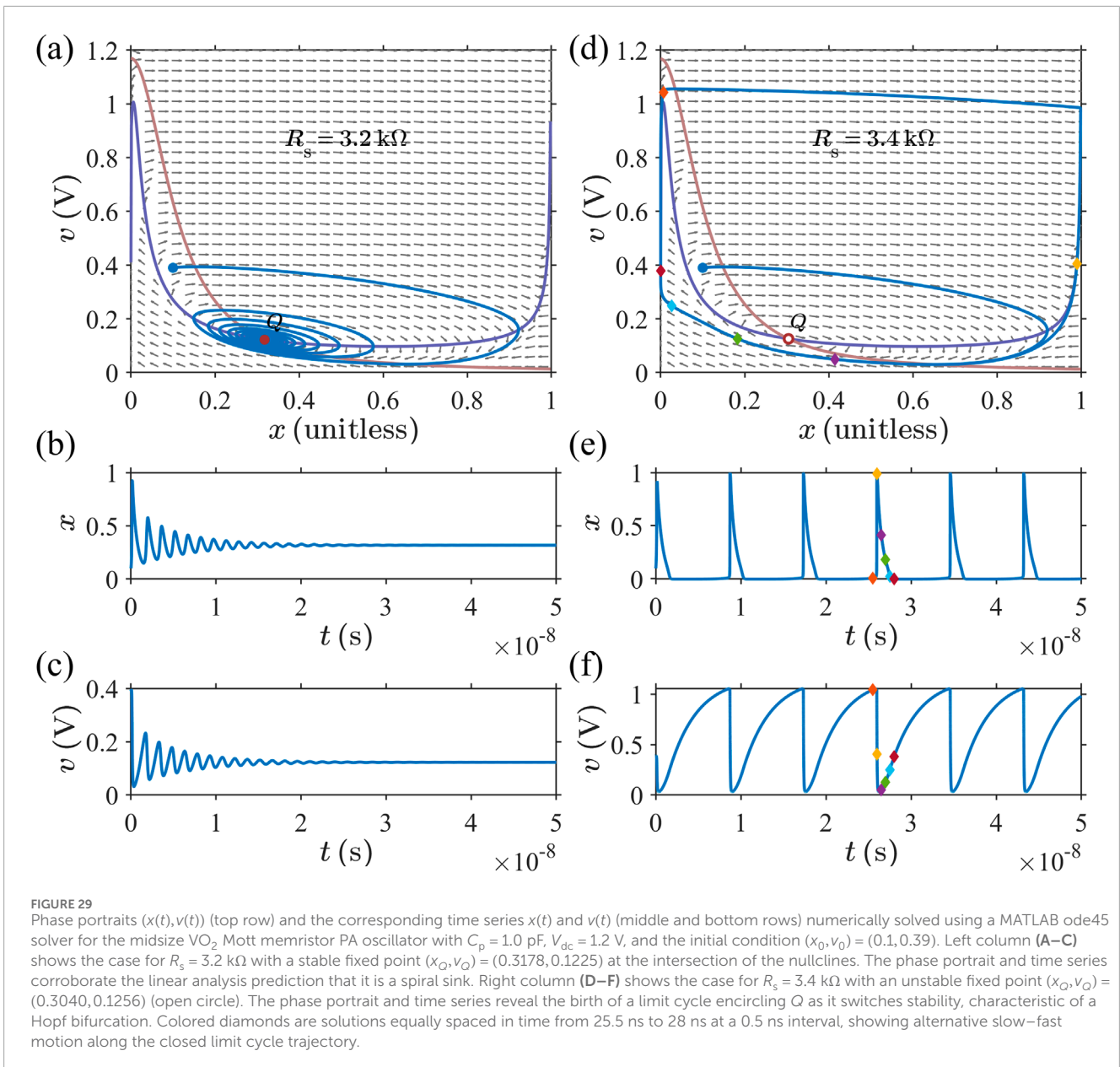
6.2 2D saddle-node bifurcations by varying V_{dc}

Plotting nullclines and direction fields at different values of V_{dc} allowed us to identify two bifurcations, both appear to be 2D saddle-node bifurcations. Next, we apply the bifurcation diagram and tr - det plane methods to clarify their nature. We step the

bifurcation parameter V_{dc} from 3.0 V to 0 V at an interval of 0.01 V while keeping the other parameters unchanged and solve the fixed points (x_Q, v_Q) by finding all the intersections of x - and v -nullclines. Figures 27A, B show the bifurcation diagrams for x_Q and v_Q , respectively. Solid (open) circles are used for stable (unstable) fixed points. There exist three distinctive regions (I, II, and III) according to the number of fixed points at a specific V_{dc} . In region I ($V_{dc} > 1.0379 \text{ V}$), there is only one fixed point Q_1 . The tr - det plane analysis (Figure 23D) reveals that Q_1 has a stability-change bifurcation at $V_{dc} = 1.21355 \text{ V}$ (labeled as Q_c^*) and switches from a stable spiral sink to an unstable spiral source as V_{dc} decreases below 1.21355 V.

At $V_{dc} = 1.0379 \text{ V}$, a new fixed point Q_a^* emerges at $(0.00589, 1.00681)$. It then splits into two fixed points Q_2 (unstable) and Q_3 (stable), which move away from each other as V_{dc} further decreases. These characteristics resemble a 2D saddle-node bifurcation. In region II ($0.519 \text{ V} < V_{dc} < 1.0379 \text{ V}$), the 2D system has three fixed points (stable Q_3 , unstable Q_1 , and Q_2). As V_{dc} continues to decrease, another bifurcation occurs at $V_{dc} = 0.519 \text{ V}$, where Q_1 and Q_2 coalesce into Q_b^* at $(0.08240, 0.31379)$ and annihilate each other. This corresponds to the v -nullcline becoming tangent to the x -nullcline in its NDR region before separating. The system only has one stable fixed point Q_3 in region III ($0 \text{ V} < V_{dc} < 0.519 \text{ V}$) as the v -nullcline only intersects with the x -nullcline in the insulating region of the Mott memristor.

To further understand the bifurcations at Q_a^* and Q_b^* , in Figure 27C, we plot the (tr, det) loci for the Jacobian of all the fixed points shown in (a) and (b). Since two of the Jacobian elements are functions of C_p , the calculations are performed at $C_p = 1.0 \text{ pF}$ to match Figure 26. The (tr, det) locus of Q_1 was already shown in Figures 23C, D and is re-plotted here with a much wider range of V_{dc} . At $V_{dc} > 1.21355 \text{ V}$, it is in the second quadrant above the $\text{det} = \text{tr}^2/4$ parabola as a stable spiral. At $V_{dc} = 1.21355 \text{ V}$, it crosses the positive det axis at Q_c^* as a center into the first quadrant



and switches stability. For $0.519 \text{ V} < V_{dc} < 1.21355 \text{ V}$, Q_1 remains unstable, first as an unstable spiral, and then as an unstable node after crossing the $\det = \text{tr}^2/4$ parabola, before vanishing at $V_{dc} = 0.519 \text{ V}$.

At $V_{dc} = 1.0379 \text{ V}$, a saddle-node bifurcation creates a new fixed point Q_a^* . Figure 27D as a zoomed-in view of Figure 27C shows that Q_a^* is located on the negative tr axis very close to the origin (at $\text{tr} = -2.23772 \times 10^8$). It then splits into a pair of fixed points, Q_2 and Q_3 . The (tr, \det) locus of Q_2 follows a V-shaped trajectory and resides entirely within the fourth quadrant, indicating that Q_2 is an unstable saddle point (class 1). The (tr, \det) locus of Q_3 is entirely within the second quadrant below the $\det = \text{tr}^2/4$ parabola, indicating that Q_3 is a stable sink (class 5). As V_{dc} decreases from 1.0379 V, Q_1 and Q_2 approach each other until they coalesce into Q_b^* as V_{dc} reaches 0.519 V, indicating that another saddle-node bifurcation occurs. Q_b^* is located on the positive tr axis. It vanishes at even lower V_{dc} values, and the only fixed point left is Q_3 in the second quadrant. Interestingly, the saddle-node bifurcation at Q_b^* involves

two unstable fixed points Q_1 and Q_2 , rather than a pair of stable and unstable fixed points as in typical cases.

It is worth mentioning that the linearized tr - \det plane predictions on the borderline classes (class 2 and 4 on the tr axis) are incorrect since Q_a^* and Q_b^* are non-hyperbolic semi-stable fixed points rather than a stable or unstable line of fixed points. It also cannot determine the occurrence of a possible Hopf bifurcation associated with the non-hyperbolic fixed point Q_c^* (class 9 on the \det axis). Therefore, we will revisit this topic in Subsection 6.7.

6.3 2D supercritical Hopf-like bifurcation by varying R_s

The tr - \det plane analysis of a linearized VO_2 Mott memristor PA oscillator showed that its fixed point can be a non-hyperbolic center as the R_s or C_p parameter passes through a critical value.

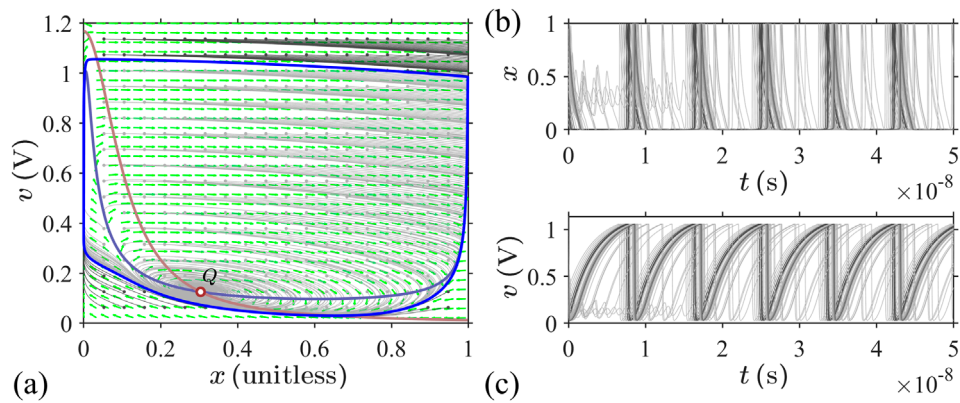


FIGURE 30

(A) Phase portrait and (B, C) the corresponding time series $x(t)$ and $v(t)$ numerically solved using a MATLAB ode45 solver for the midsize VO₂ Mott memristor PA oscillator with $C_p = 1.0$ pF, $V_{dc} = 1.2$ V, and $R_s = 3.4$ k Ω . The system has an unstable fixed point $(x_Q, v_Q) = (0.3040, 0.1256)$ (open circle) at the intersection of the nullclines. A total of 324 orbits are solved with their initial conditions (solid dots) located on a regular grid of (x_0, v_0) , with 18 x_0 levels evenly spaced from 0.05 to 0.95 and 18 v_0 levels ranging from 0.06 V to 1.14 V. Orbits that start from within and outside the limit cycle are shown in light and dark gray colors, respectively. Every $(x(t), v(t))$ trajectory converges onto the same limit cycle (blue orbit) encircling Q , regardless of the initial condition location. The $x(t)$ and $v(t)$ time series show different oscillation phases depending on the initial condition, but all share the same period. The mean (standard deviation) of the oscillation period is 8.621 ns (5 ps).

Stability and qualitative behavior of nonlinear systems near a non-hyperbolic fixed point are complex and require further theoretical treatment. Here, using R_s as the bifurcation parameter, we illustrate an example of a 2D local Hopf-like bifurcation. For nonlinear systems of dimension two or higher, a local Hopf bifurcation, also called Poincaré–Andronov–Hopf bifurcation, is the local creation or annihilation of a periodic solution around a fixed point as it switches stability. The bifurcating periodic solution is called a limit cycle, which is an isolated periodic orbit (closed trajectory) with no nearby periodic orbits, such that at least a nearby trajectory spirals into it either as time approaches infinity or as time approaches negative infinity. The orbital stability of a limit cycle is opposite to that of the fixed point it encircles. If a stable limit cycle appears around an unstable fixed point, it is a supercritical Hopf bifurcation. Otherwise, if an unstable limit cycle appears around a stable fixed point, then it is a subcritical Hopf bifurcation. The example we will discuss has supercritical orbital stability.

6.4 Hopf bifurcation theorem

For a nonlinear system near a non-hyperbolic fixed point in its linear part, the center manifold theorem states that its qualitative behavior can be determined by the behavior on the center manifold. The Jacobian matrix of the linearized system defines three main subspaces according to the real part of its eigenvalues. The center subspace is spanned by eigenvectors corresponding to eigenvalues with zero real parts. A center manifold is an invariant manifold that has the same dimension as the center subspace and is tangent to it. The stability problem is, therefore, reduced to lower dimensions. A direct application of the center manifold theorem is the Hopf bifurcation theorem, which allows *analytical* prediction on the existence of limit cycles. A version of the Hopf bifurcation theorem that is generalized to \mathbb{R}^n is briefly introduced here (Marsden and McCracken, 1976; Guckenheimer and Holmes, 1983). Consider a nonlinear system $\dot{\mathbf{x}} = \mathbf{f}(\mathbf{x}; \mu)$, $\mathbf{x} \in \mathbb{R}^n$, $\mu \in \mathbb{R}$, where μ is a bifurcation

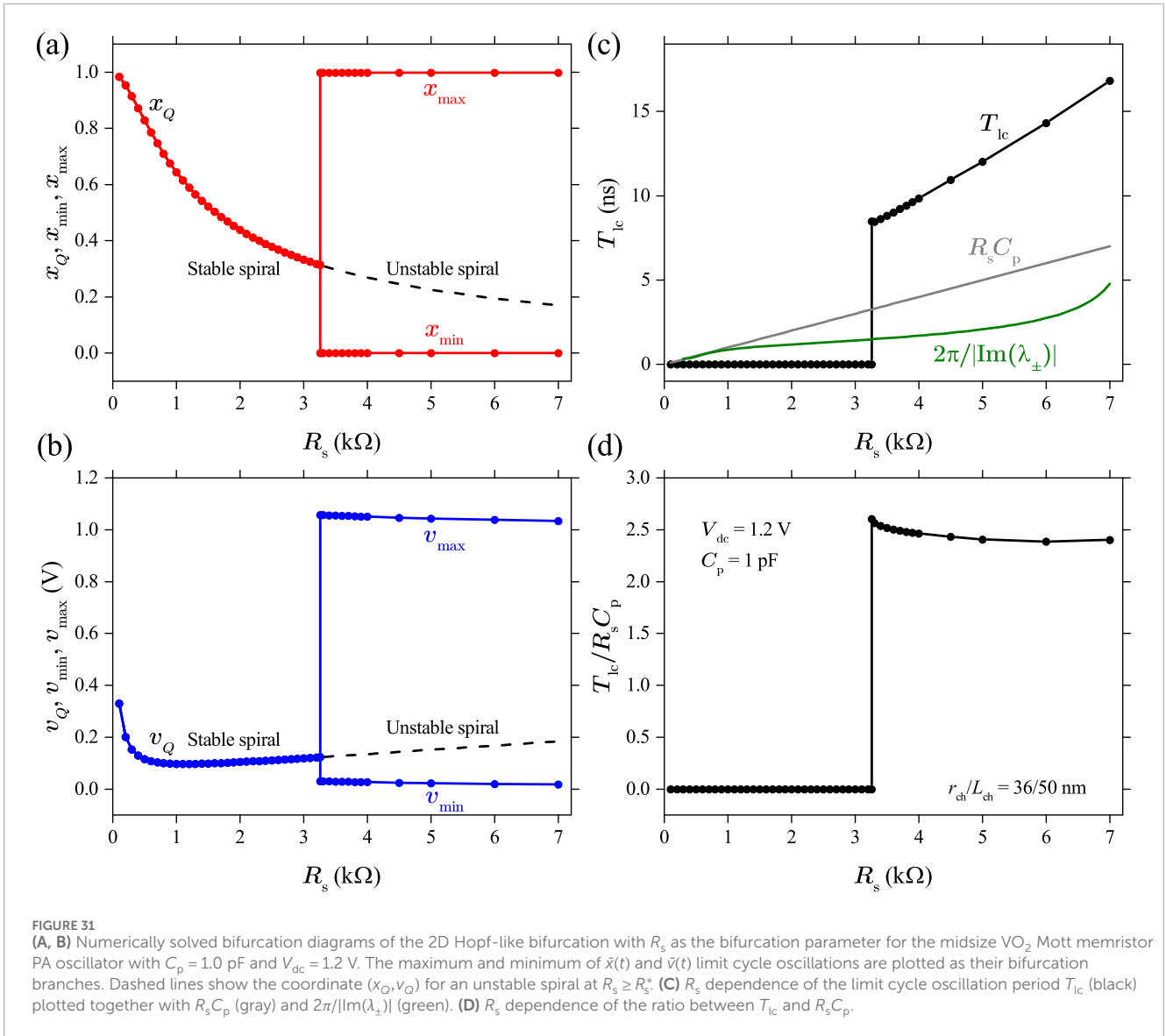
parameter. Assume that it has a fixed point $(\mathbf{x}_0; \mu)$ so that $\mathbf{f}(\mathbf{x}_0; \mu) = 0$. The eigenvalues of the linearized system $\dot{\mathbf{x}} = D\mathbf{f}(\mathbf{x}; \mu)$ at this fixed point are $\lambda_{\pm}(\mu) = \alpha(\mu) \pm \beta(\mu)i$. If both the following conditions are satisfied at $\mu = \mu_0$:

- $\alpha(\mu_0) = 0$ and $\beta(\mu_0) \neq 0$ (non-hyperbolicity condition), i.e., there is a pair of simple, conjugate pure imaginary eigenvalues and other pure imaginary eigenvalues are not present and
- $\left. \frac{d\alpha(\mu)}{d\mu} \right|_{\mu=\mu_0} = d \neq 0$ (transversality condition), i.e., the eigenvalues cross the imaginary axis with finite speed,

Then there is a unique center manifold passing through $(\mathbf{x}_0; \mu_0)$ in $\mathbb{R}^n \times \mathbb{R}$.

The third condition (genericity condition) is about the first Poincaré–Lyapunov constant $L_1(\mu_0)$, which is the coefficient of cubic terms if the system is transferred to the normal form. If $L_1(\mu_0) \neq 0$, then a surface of periodic solutions exists in the center manifold. Approximated to the second order, this surface is a paraboloid tangent to the eigenspace associated with $\lambda_{\pm}(\mu_0)$. The region for periodic solutions to appear (either as μ moves into $\mu < \mu_0$ or into $\mu > \mu_0$) and the stability of periodic solutions are determined by the signs of $L_1(\mu_0)$ and d (Marsden and McCracken, 1976). For the case of $d > 0$ that is relevant to our example, if $L_1(\mu_0) < 0$, then Hopf bifurcation is supercritical, i.e., a stable limit cycle bifurcates from an unstable fixed point into the region $\mu > \mu_0$. If $L_1(\mu_0) > 0$, then Hopf bifurcation is subcritical, i.e., an unstable limit cycle bifurcates from a stable fixed point into the region $\mu < \mu_0$.

The calculation of $L_1(\mu_0)$ can be a substantial effort as it involves the second- and third-order derivatives of the system at the bifurcation point. For the sake of brevity, we do not derive the first Poincaré–Lyapunov constant $L_1(\mu_0)$ for a Mott memristor PA oscillator and only examine whether it satisfies the non-hyperbolicity and transversality conditions. Figure 28A shows the complex-plane loci of the pair of simple, conjugate eigenvalues $\lambda_{\pm}(R_s)$, calculated using Equation 68 for the Jacobian of the midsize VO₂ Mott memristor PA oscillator that has been analyzed by



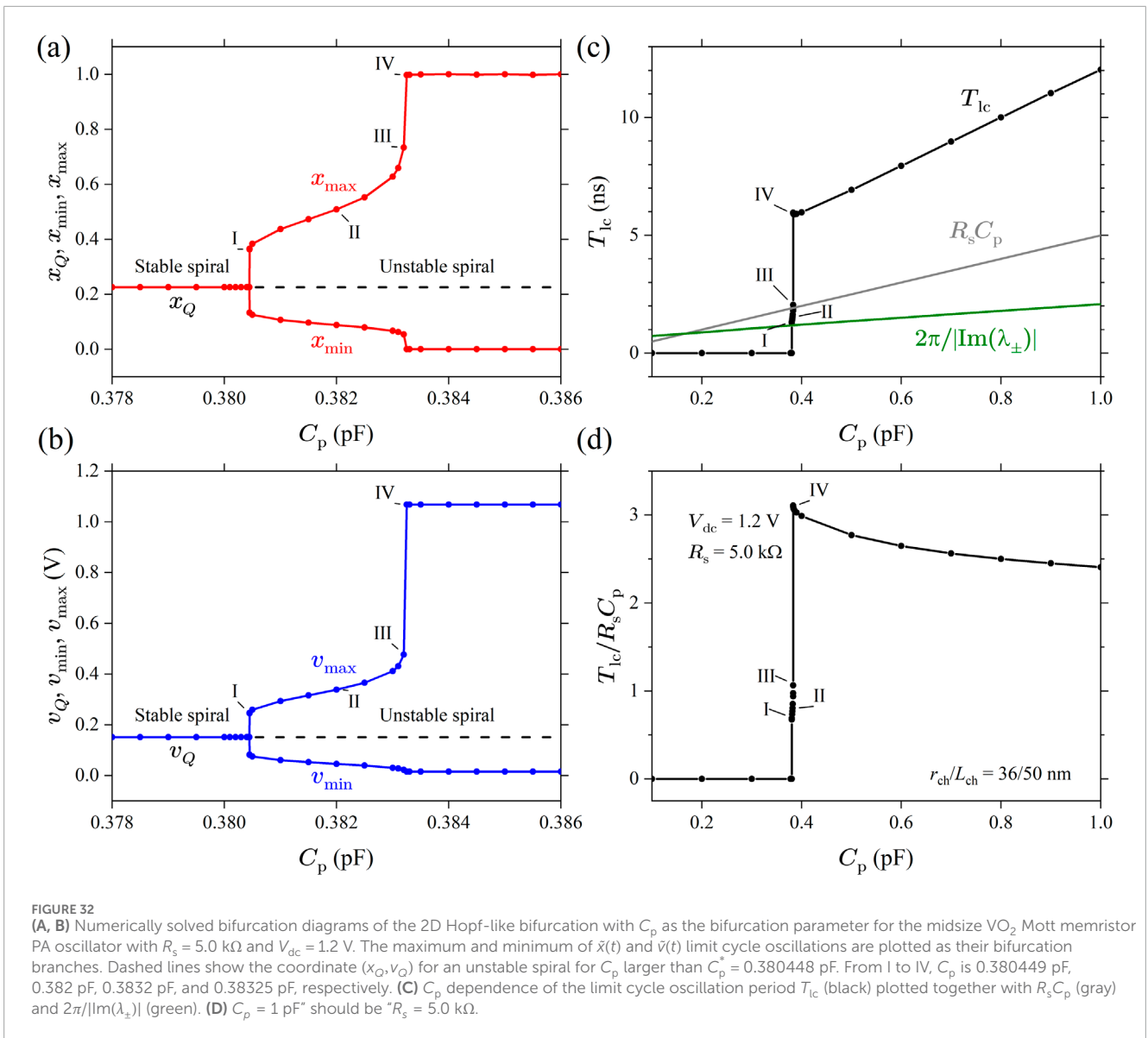
the tr-det plane method (see Figure 23). Fixing C_p and V_{dc} and increasing the bifurcation parameter R_s , the fixed point of the linearized system evolves from a stable spiral ($\text{Re}(\lambda_{\pm}) < 0$) to a non-hyperbolic center ($\text{Re}(\lambda_{\pm}) = 0$) at $R_s^* = 3359.5 \Omega$ and then to an unstable spiral ($\text{Re}(\lambda_{\pm}) > 0$). At $R_s = R_s^*$, the system satisfies the non-hyperbolicity condition for a Hopf bifurcation. Figure 28B shows the plots of $d\text{Re}(\lambda_{\pm})/dR_s$ vs R_s calculated from $\lambda_{\pm}(R_s)$, which shows that the derivative of the real part of eigenvalues with respect to the bifurcation parameter R_s is finite and positive at the non-hyperbolic center ($R_s = R_s^*$) and its nearby region. Thus, the transversality condition for a Hopf bifurcation is also satisfied.

6.5 Phase portrait analysis of limit cycles

In this section, we check the abovementioned analytical prediction against numerical calculations. A local Hopf bifurcation

can be revealed by numerically solving the coupled ODEs with an arbitrary initial condition (x_0, v_0) and then inspecting the orbit of the solution $(x(t), v(t))$ in the phase plane, which is pre-loaded with nullclines and direction field. Such a plot is called a phase portrait. Plotting the time series $x(t)$ and $v(t)$ of the numerical solution helps reveal whether there are damped oscillations toward a stable fixed point or persistent self-excited oscillations characteristic of a limit cycle.

Figure 29 shows the comparison of two sets of phase portraits and the corresponding time series for the midsize VO₂ Mott memristor PA oscillator with $C_p = 1.0$ pF, $V_{dc} = 1.2$ V, and initial condition $(x_0, v_0) = (0.1, 0.39)$, numerically solved using a MATLAB ode45 solver (Hong, 2022). Figures 29A–C (left column) show the case for $R_s = 3.2$ kΩ. At this value of R_s , there is a single fixed point $(x_Q, v_Q) = (0.3178, 0.1225)$ at the intersection of the nullclines. The linear tr-det plane analysis predicts that it is a stable spiral sink (see Figure 23B and text). The phase portrait corroborates this prediction, showing that the orbit of the solution (purple trace)

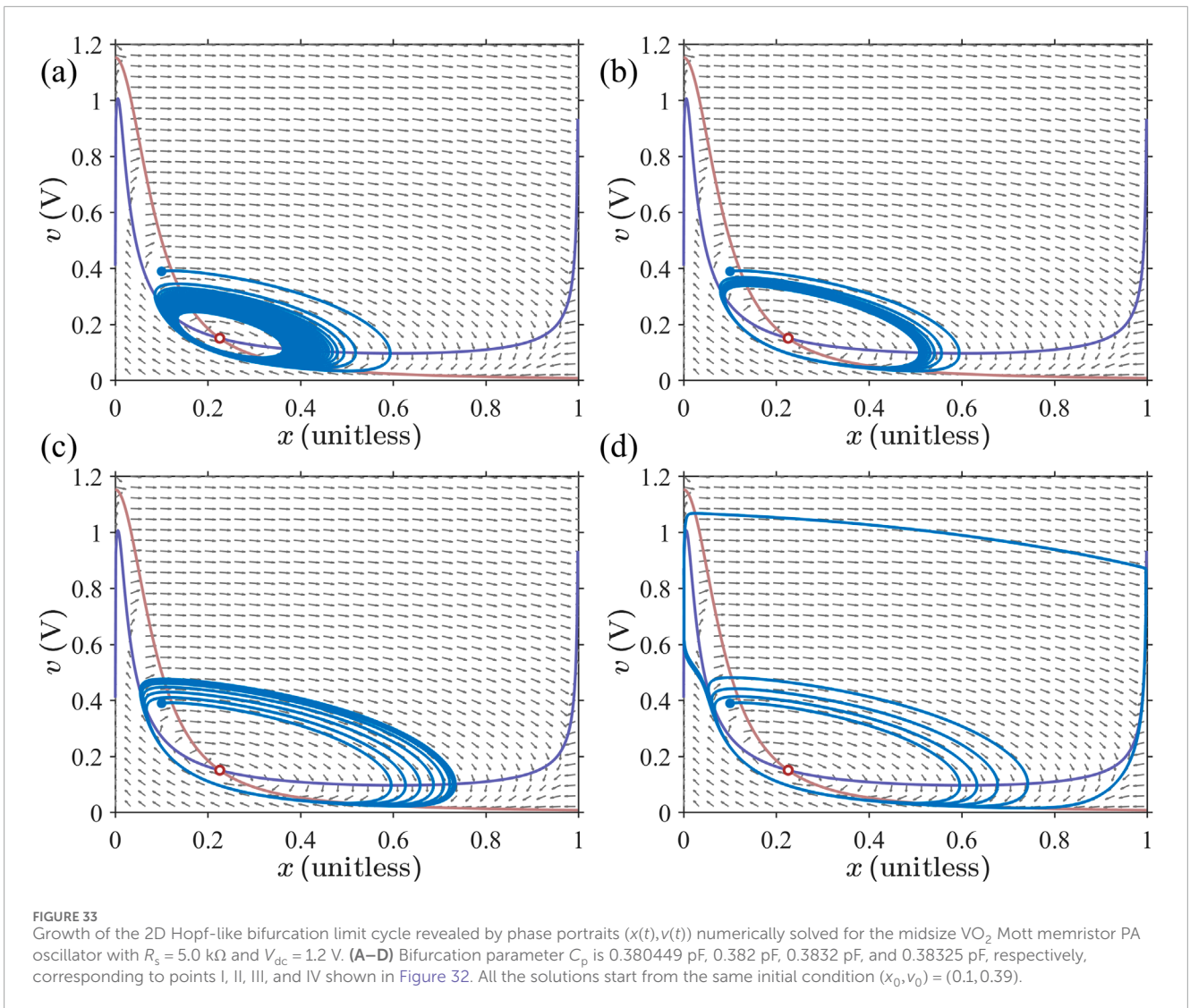


converges to Q along a clockwise spiral trajectory. The clockwise rotation of the system state over time is determined by the direction field. The time series $x(t)$ and $v(t)$ shown in the bottom rows exhibit fast damped oscillations that come to rest at (x_Q, v_Q) within approximately 20 ns.

Figures 29D–F (right column) show the case for $R_s = 3.4 \text{ k}\Omega$. Such a small increase in R_s (by 200Ω) results in a tiny shift in the location of Q to $(x_Q, v_Q) = (0.3040, 0.1256)$. The linear tr–det analysis predicts that Q switches its stability and becomes an unstable spiral source. The orbit initially resembles the case of Figure 29A, but it does not finish even one loop around Q before morphing into a periodic orbit that rotates clockwise about Q with a distorted rectangular shape. The corresponding time series $x(t)$ and $v(t)$ shown in the bottom rows exhibit periodic oscillations—a pulse train $\bar{x}(t + T_{lc}) = \bar{x}(t)$ and a sawtooth wave $\bar{v}(t + T_{lc}) = \bar{v}(t)$, both launched after a very short transient period. Here, T_{lc} is the period of the limit cycle. The appearance of a stable limit cycle around a fixed point as it

switches from a stable sink to an unstable source is the hallmark of a supercritical Hopf bifurcation. We added several colored diamonds to represent solutions $x(t)$ and $v(t)$ equally spaced in time from 25.5 ns to 28 ns at a 0.5-ns interval. Their locations on the closed trajectory of the limit cycle are clearly unevenly spaced, revealing the alternative slow-fast motion along it as a hallmark for relaxation oscillations.

To convince ourselves that the periodic orbit revealed by Figures 29D–F is both isolated and stable, i.e., a stable limit cycle, we numerically calculated 324 solutions of the same system with the initial condition (x_0, v_0) , distributed on a regularly spaced (18×18) grid that spans across almost the entire allowable (x, v) phase space. x_0 is evenly spaced from 0.05 to 0.95, and v_0 ranges from 0.06 V to 1.14 V. Orbits that start from within and outside the limit cycle are in light and dark gray colors, respectively. The results are shown in Figure 30. The phase portrait in Figure 30A shows a sampled view of the flow of this 2D nonlinear system. It shows that,



regardless of its initial condition location, the $(x(t), v(t))$ orbit always settles on the same limit cycle $(\tilde{x}(t), \tilde{v}(t))$ (the blue orbit) after a transient movement. If (x_0, v_0) is very close to Q , the transient part of the orbit can form many turns of a clockwise spiral following the direction field, but the orbit always manages to “escape” from Q and becomes a limit cycle encircling it. The time series in Figure 30B reveals that the time elapsed in the transient stage until $x(t)$ (or $v(t)$) becomes periodic varies across individual solutions, depending on the initial condition (x_0, v_0) . The distinctive transient time causes the oscillation waveforms to be asynchronous across individual orbits, which is equivalent to having different oscillation phases. However, all the time series settle as oscillations sharing the same period. To be precise, the mean (standard deviation) of the oscillation period is 8.621 ns (5 ps), with a coefficient of variation as small as 0.06%. The minimum and maximum oscillation periods are 8.6 ns and 8.626 ns, respectively. The robustness of a limit cycle against the initial transient may explain why life is full of relaxation oscillators, including the heartbeat (van der Pol and van der Mark, 1928).

Figures 31A, B show the plot of the numerically solved bifurcation diagrams of the 2D Hopf-like bifurcation, with R_s as

the bifurcation parameter. We noticed that the critical value $R_s^* = 3258.00799$ Ω found by numerical calculations is approximately 3% different from the analytical value of 3359.5 Ω (see Figure 28), possibly due to rounding or truncation errors. Both $x_Q(R_s)$ and $v_Q(R_s)$ are smooth functions of R_s . For $R_s < R_s^*$ (with a difference as small as 10 $\mu\Omega$), there is a single fixed point (x_Q, v_Q) , which is a stable spiral according to the linearization analysis. At $R_s \geq R_s^*$, instead of just switching its stability to an unstable spiral (dashed lines), the fixed point bifurcates to a limit cycle. Since a limit cycle is a collection of periodic points $(\tilde{x}(t), \tilde{v}(t))$, we use the maximum and minimum of $\tilde{x}(t)$ and $\tilde{v}(t)$ oscillations to represent their bifurcation branches, with the ranges between maximum and minimum serving as a measure of the bifurcation amplitude. This definition is not unique. One can borrow the concepts from celestial mechanics and define the unstable spiral as a focus; then, the periapsis (minimum) and apoapsis (maximum) distances between a point in the limit cycle orbit and the focus can also be used to represent the bifurcation amplitude.

A prominent feature of the Mott memristor PA oscillator model is the abrupt appearance or “hard transition” of a stable

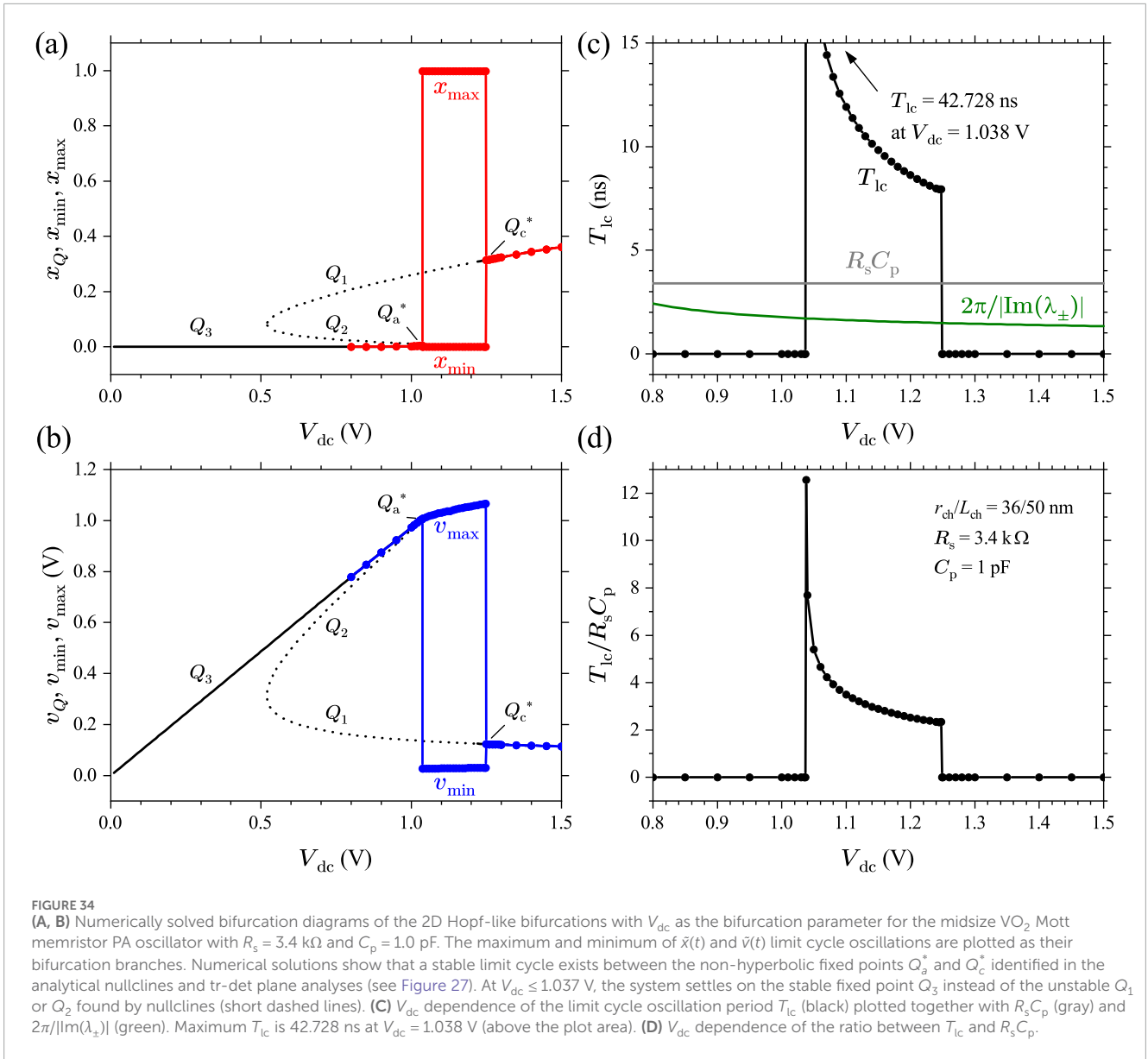


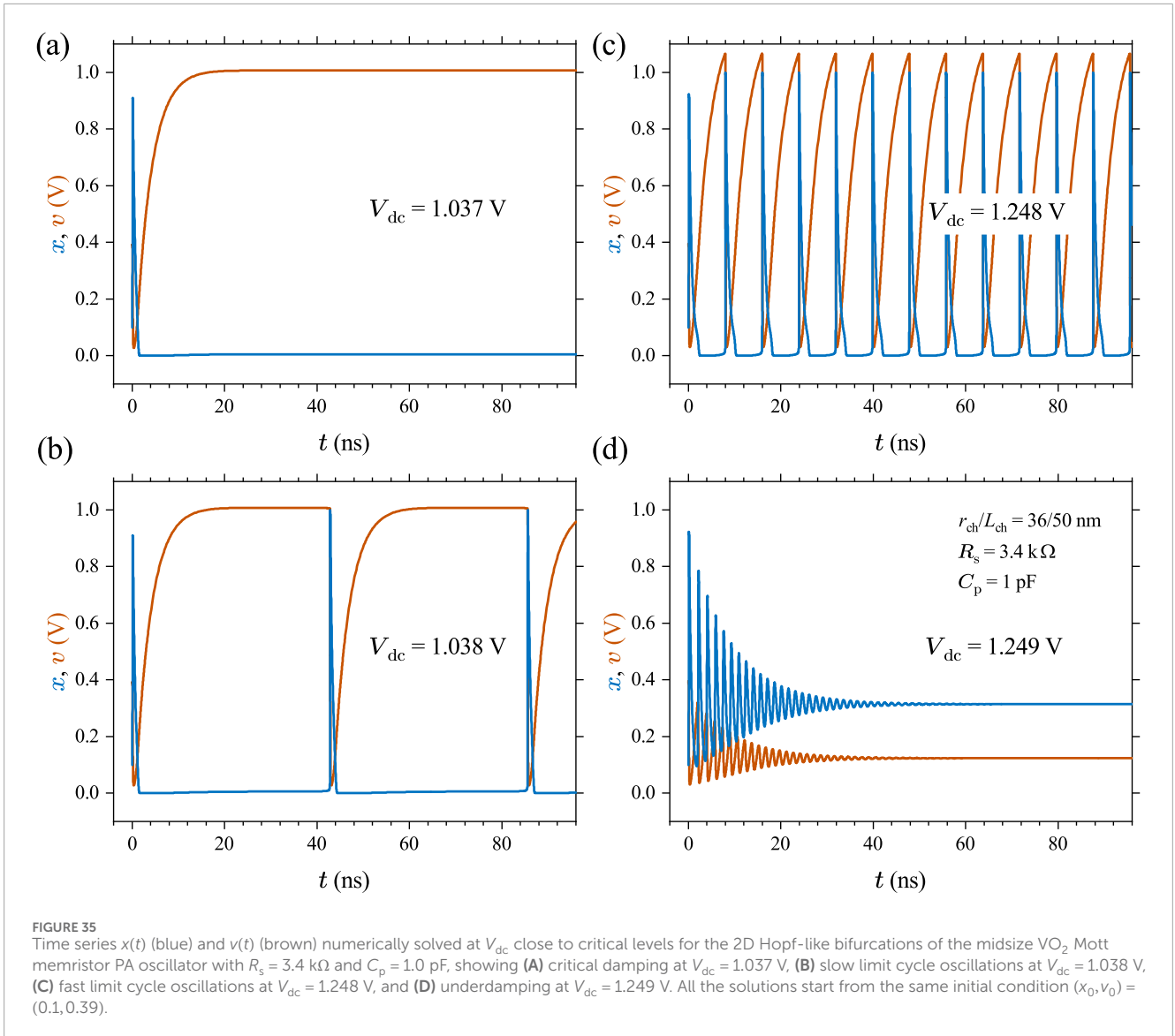
FIGURE 34

(A, B) Numerically solved bifurcation diagrams of the 2D Hopf-like bifurcations with V_{dc} as the bifurcation parameter for the midsize VO₂ Mott memristor PA oscillator with $R_s = 3.4$ k Ω and $C_p = 1.0$ pF. The maximum and minimum of $\bar{x}(t)$ and $\bar{v}(t)$ limit cycle oscillations are plotted as their bifurcation branches. Numerical solutions show that a stable limit cycle exists between the non-hyperbolic fixed points Q_a^* and Q_c^* identified in the analytical nullclines and tr-det plane analyses (see Figure 27). At $V_{dc} \leq 1.037$ V, the system settles on the stable fixed point Q_3 instead of the unstable Q_1 or Q_2 found by nullclines (short dashed lines). (C) V_{dc} dependence of the limit cycle oscillation period T_{lc} (black) plotted together with $R_s C_p$ (gray) and $2\pi/|\text{Im}(\lambda_{\pm})|$ (green). Maximum T_{lc} is 42.728 ns at $V_{dc} = 1.038$ V (above the plot area). (D) V_{dc} dependence of the ratio between T_{lc} and $R_s C_p$.

limit cycle that is completely unfolded over an extremely thin bifurcation parameter interval. The amplitude of a classical Hopf bifurcation for smooth systems increases like $\sqrt{|\mu - \mu_0|}$, i.e., the oscillation amplitude is infinitesimal as $\mu \rightarrow \mu_0$. However, in the present case, the oscillations in $\bar{x}(t)$ and $\bar{v}(t)$ almost immediately switch to full swing as long as R_s surpasses R_s^* , and then, their amplitudes remain essentially unchanged as R_s further increases. The abrupt appearance of a stable limit cycle was observed in piecewise-linear systems that have a cut-off or saturation region, e.g., a Wien bridge oscillator (Kriegsmann, 1987; Freire et al., 1999). For the present Mott memristor model, the fact that the kinetic function diverges toward negative infinity as x approaches 1.0 (see Figure 3 inset) reveals that there is an *implicit saturation* in the model. A sudden formation of relaxation oscillations, termed a “canard explosion,” has been observed in chemical and biological systems and analyzed thoroughly in the context of Liénard systems, e.g., a van der Pol oscillator (Krupa and Szmolyan, 2001;

Rotstein et al., 2012). The hard transition in relaxation oscillations forms the basis for understanding the all-or-nothing spike firings in biological neurons that can be considered reaction-diffusion systems of coupled relaxation oscillators, which has been experimentally demonstrated in Mott memristor-based neuromorphic neurons [for examples, see Figure 3 in Pickett et al. (2013) and Figure 5 in Yi et al. (2018)].

Figure 31C shows the dependence of the limit cycle oscillation period T_{lc} on R_s . For $R_s < R_s^*$, T_{lc} is 0 since there is no oscillation. At $R_s \geq R_s^*$, T_{lc} emerges like a step function and then increases almost linearly with R_s . For comparison, the $R_s C_p$ time constant as a function of R_s is also plotted (gray line). Figure 31D shows the ratio between T_{lc} and $R_s C_p$, which remains almost flat in the bifurcation region, with an initial overshoot to 2.6, followed by a gradual descent toward 2.4. Generally, the oscillation period of a Hopf bifurcation approaches $2\pi/|\text{Im}(\lambda_{\pm})|$ as $\mu \rightarrow \mu_0$. However, in the present case, the calculated $2\pi/|\text{Im}(\lambda_{\pm})|$ curve (green)



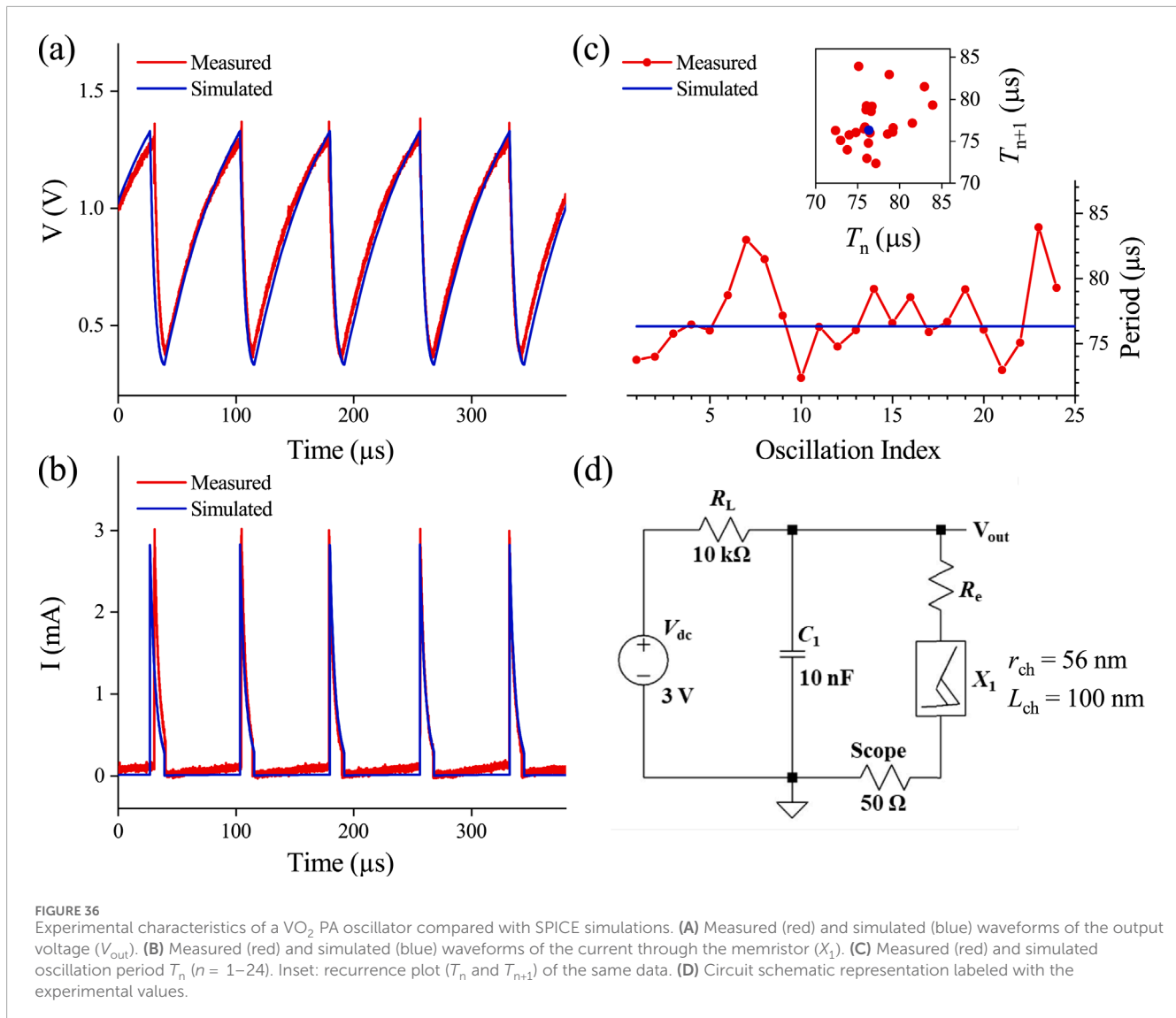
is approximately 1.5 ns at $R_s \approx R_s^*$, which is much smaller than $T_{lc} \approx 8.5 \text{ ns}$.

6.6 2D supercritical Hopf-like bifurcation by varying C_p

From the tr-det plane analysis of a linearized VO_2 Mott memristor PA oscillator (see Figure 24 and text), we know that C_p is also possibly a bifurcation parameter as the system's fixed point becomes a non-hyperbolic center as C_p passes through a critical value. Now, we apply the numerical phase portrait method to examine whether C_p is a bifurcation parameter that triggers a 2D local Hopf-like bifurcation.

We numerically solved phase portraits and the corresponding time series for the midsize VO_2 Mott memristor PA oscillator with $R_s = 5.0 \text{ k}\Omega$, $V_{dc} = 1.2 \text{ V}$, and initial condition $(x_0, v_0) = (0.1, 0.39)$. C_p is varied from 0.1 pF to 1 pF. Figures 32A, B show the plots

of the numerically solved bifurcation diagrams of the 2D Hopf-like bifurcation, with C_p as the bifurcation parameter, which reveal a critical value $C_p^* = 0.380448 \text{ pF}$ to trigger the bifurcation. This value is approximately 0.3% different than the analytical value of 0.381469 pF (see Figure 24), possibly due to rounding or truncation errors. For $C_p < C_p^*$ (with a difference as small as 1 attofarad), there is a single fixed point (x_Q, v_Q) , which is a stable spiral according to the linearization analysis. Both $x_Q(R_s)$ and $v_Q(R_s)$ are independent of C_p , as described by the nullcline analysis. At $C_p \geq C_p^*$, instead of just switching its stability to an unstable spiral (dashed lines), the fixed point bifurcates to a limit cycle. Compared with the case of R_s -induced Hopf-like bifurcation with abrupt unfolding, there is a striking difference in the C_p -induced Hopf-like bifurcation. Within a narrow range of C_p (between C_p^* and $\sim 0.3832 \text{ pF}$), the bifurcation amplitude increases more gradually and resembles the general prediction of $\sqrt{|\mu - \mu_0|}$, albeit it still has an abrupt switch on; thus, the oscillation amplitude is not infinitesimal as $\mu \rightarrow \mu_0$. To illustrate the gradual increase in the 2D Hopf-like bifurcation



limit cycle, in Figure 33, we plot the numerically solved phase portraits ($x(t), v(t)$) at points I, II, III, and IV, corresponding to C_p at 0.380,449 pF, 0.382 pF, 0.3832 pF, and 0.38325 pF, respectively. One can observe that the gradual increase in the Hopf-like bifurcation gives way to abrupt unfolding upon a further increase in C_p beyond 0.3832 pF.

Figure 32C shows the dependence of the limit cycle oscillation period T_{lc} on C_p . At $C_p \approx C_p^*$, the calculated $2\pi/|\text{Im}(\lambda_{\pm})|$ curve (green) is approximately 1.18 ns, which is very close to $T_{lc} \approx 1.28$ ns (point I). This confirms that the oscillation period of C_p -induced Hopf-like bifurcation approaches the general prediction of $2\pi/|\text{Im}(\lambda_{\pm})|$ as $\mu \rightarrow \mu_0$. At the upper limit of the gradual growth stage (point III), the oscillation period $T_{lc} \approx 2.0$ ns is close to the $R_s C_p$ time constant. Then, it abruptly increases to 6 s at point IV as the limit cycle expands to full swing. Figure 32D shows the ratio between T_{lc} and $R_s C_p$. In the initial gradual growth stage, this ratio hovers around unity (increases from 0.68 at point I to 1.07 at point III). In the full-swing bifurcation stage, the trend of this ratio versus the bifurcation parameter is similar to the case of R_s , with a larger initial overshoot to 3.1, followed by a gradual descent toward 2.4.

6.7 2D supercritical Hopf-like bifurcation by varying V_{dc}

In this section, we revisit the case of varying V_{dc} as the bifurcation parameter using the numerical phase portrait method. In Subsection 6.2, we identified two saddle-node bifurcations using the analytical nullclines and linearized tr-det plane analyses. However, these techniques cannot determine whether there exists a Hopf bifurcation or limit cycle around a non-hyperbolic fixed point, such as Q_c^* shown in Figure 27. To clarify, numerical phase portrait calculations are needed.

We numerically solved the phase portraits and the corresponding time series for the midsize VO₂ Mott memristor PA oscillator with $R_s = 3.4$ k Ω , $C_p = 1.0$ pF, and initial condition $(x_0, v_0) = (0.1, 0.39)$. Figures 34A, B show the plot of the numerically solved bifurcation diagrams (solid dots). The calculations reveal a stable limit cycle associated with a supercritical Hopf-like bifurcation if V_{dc} is within a range bounded by the two non-hyperbolic fixed points Q_a^* and Q_c^* , both identified by the analytical methods (see Figure 27). The numerically determined critical V_{dc}

at Q_a^* falls between 1.037 V and 1.038 V, which matches with the analytical result of 1.0379 V. For Q_c^* , it is between 1.248 V and 1.249 V, which is approximately 2.9% higher than the analytical result of 1.21355 V. At $V_{dc} \leq 1.037$ V, the system is critically damped. After a fast transient response, $x(t)$ and $v(t)$ return to the stable steady state Q_3 without oscillation. See Figure 35A for the case of $V_{dc} = 1.037$ V. The system never settles on either one of the unstable Q_1 or Q_2 fixed points (short dashed lines), which are identified by the nullclines. At $V_{dc} \geq 1.249$ V, the system is underdamped, with $x(t)$ and $v(t)$ oscillating with decaying amplitude to the stable steady state Q_1 . See Figure 35D for the case of $V_{dc} = 1.249$ V. The system has persistent limit cycle oscillations for $1.038 \text{ V} \leq V_{dc} \leq 1.248 \text{ V}$ (see Figures 35B, C for the cases of 1.038 V and 1.248 V, respectively). Similar to the case of varying R_s , there is an abrupt unfolding in the bifurcation amplitude at both Q_a^* and Q_c^* .

Figure 34C shows the V_{dc} dependence of the limit cycle oscillation period T_{lc} . As V_{dc} increases through the lower bound Q_a^* of the limit cycle region, the persistent oscillation is initially extremely slow, i.e., T_{lc} significantly overshoots. T_{lc} is 12.6 times the $R_s C_p$ time constant (42.7 ns vs. 3.4 ns) or 25 times $2\pi/|\text{Im}(\lambda_{\pm})|$ (42.7 ns vs. 1.7 ns). As V_{dc} increases, T_{lc} decreases super-exponentially. Figure 34D shows that near the upper bound Q_c^* of the limit cycle region, the ratio between T_{lc} and $R_s C_p$ decreases to 2.34 (7.95 ns vs. 3.4 ns), which is at the same level as the cases of varying R_s (Figure 31D) or C_p (Figure 32D).

We conclude this section with a comparison between experimental characteristics of a VO_2 PA oscillator circuit and SPICE model simulations built upon the model Equations 1, 2, using parameters listed in Tables 1, 2. Details on the implementation of the Mott memristor model in SPICE can be found in the supplementary materials of Pickett and Williams (2012). Figure 36D shows the circuit schematic labeled with the experimental values. The VO_2 nano-crossbar memristor (X_1) has a square junction area of $100 \times 100 \text{ nm}^2$ and oxide film thickness of 100 nm, equivalent to a circular channel radius $r_{ch} = 56 \text{ nm}$ and length $L_{ch} = 100 \text{ nm}$ in the model. $R_e = 370 \Omega$ is the measured series resistance of metal electrodes. A parallel shunt resistance of 20 k Ω (not shown) is included in simulations to account for the parasitic insulating-phase conductance present in the VO_2 device. The oscillator output voltage V_{out} is probed by an input channel of an oscilloscope with high input impedance. The current flowing through X_1 is monitored by a second input channel with 50 Ω input impedance. Figure 36A shows the comparison of the measured (red) and simulated (blue) V_{out} waveforms, both showing the hallmark sawtooth relaxation oscillations. Figure 36B shows the comparison of the measured and simulated current waveforms. In both (a) and (b), we found excellent agreements between the measured and simulated results. Figure 36C shows the period T_n of 24 consecutive oscillation peaks. The measured oscillation period irregularly fluctuates within a range from 72.4 μs to 83.9 μs , while the simulated period is nearly a constant at 76.3 μs . Inset of (c) is the recurrence plot (Poincaré plot or return map) of adjacent oscillation periods (T_n and T_{n+1}), showing the irregularities of experimental relaxation oscillations. The randomness in measured oscillation periods manifests that these nanoscaled Mott memristors are intrinsically stochastic, which has been demonstrated in stochastic phase-locked firing (skipping) of neuromorphic neurons built with higher-dimensional VO_2 Mott memristor circuits (Yi et al., 2018).

7 Concluding remarks

In our view, the implications of locally active memristors extend far beyond signal amplification or biological nerve impulse emulation. These scalable nonlinear dynamical elements enable a high degree of complexity at the network-building-block level. From the perspective of neuronal dynamics, one can borrow the concept of logical depth and measure the degree of complexity of a neuron model by approximating the number of floating point operations needed to simulate its dynamics for 1-millisecond duration on a digital computer (Bennett, 1988). The biologically plausible HH model requires 1200 FLOP/ms and has the highest degree of complexity among 11 neuron models (Izhikevich, 2004). The degree of complexity of a Mott memristor neuron is at least as high as that of the HH model, given that both exhibit similar range of neurocomputational properties. Architecturally simple yet dynamically rich neuron nodes may allow computationally efficient, small adaptive neural networks suited for edge computing scenarios, which require real-time causal reasoning based on the time-series data from unlabeled samples. These use cases remain particularly challenging for today's artificial intelligence systems, which rely on machine learning and computationally expensive offline training in the cloud. As the network scales up, more interesting complexity phenomena may emerge at the mesoscopic level of neuron populations due to the collective interactions of constituent nodes, such as chaotic attractor itinerancy, self-organization, and synchronization. Understanding these phenomena is crucial for replicating the perception and cognition capabilities of the brain.

Data availability statement

The original contributions presented in the study are included in the article/supplementary material; further inquiries can be directed to the corresponding author.

Author contributions

WY: Conceptualization, Data curation, Formal Analysis, Funding acquisition, Investigation, Methodology, Project administration, Resources, Software, Supervision, Validation, Visualization, Writing – original draft, Writing – review and editing.

Funding

The author(s) declare that financial support was received for the research, authorship, and/or publication of this article. This work was funded by HRL Laboratories, LLC.

Acknowledgments

The author is very grateful to the leaders and colleagues of Sensors and Electronics Laboratory for their unwavering support of this research. Kenneth K. Tsang, James M. Chappell, Stephen K. Lam, Xiwei Bai, Jack A. Crowell, and Elias A. Flores are

acknowledged for their contributions to the experimental data (see Figures 1, 36) presented in this article. W.Y. is thankful to the referees for their constructive feedback and valuable suggestions.

Conflict of interest

Author WY was employed by HRL Laboratories, LLC.

References

- Amsinck, C. J., Di Spigna, N. H., Nackashi, D. P., and Franzone, P. D. (2005). Scaling constraints in nanoelectronic random-access memories. *Nanotechnology* 16, 2251–2260. doi:10.1088/0957-4484/16/10/047
- Andrews, J. L., Santos, D. A., Meyyappan, M., Williams, R. S., and Banerjee, S. (2019). Building brain-inspired logic circuits from dynamically switchable transition-metal oxides. *Trends Chem.* 1, 711–726. doi:10.1016/j.trechm.2019.07.005
- Ascoli, A., Demirkol, A. S., Tetzlaff, R., and Chua, L. O. (2022a). Edge of chaos explains prigogine's instability of the homogeneous. *IEEE J. Em. Sel. Top.* 12, 804–820. doi:10.1109/JETCAS.2022.3221156
- Ascoli, A., Demirkol, A. S., Tetzlaff, R., and Chua, L. O. (2022b). Edge of chaos is sine qua non for Turing instability. *IEEE Trans. Circ. Syst. I* 69, 4596–4609. doi:10.1109/TCSI.2022.3194465
- Ascoli, A., Demirkol, A. S., Tetzlaff, R., and Chua, L. O. (2022c). Edge of chaos theory resolves smale paradox. *IEEE Trans. Circ. Syst. I* 69, 1252–1265. doi:10.1109/TCSI.2021.3133627
- Ascoli, A., Demirkol, A. S., Tetzlaff, R., Slesazek, S., Mikolajick, T., and Chua, L. O. (2021). On local activity and edge of chaos in a NaMLab memristor. *Front. Neurosci.* 15, 651452. doi:10.3389/fnins.2021.651452
- Ascoli, A., Tetzlaff, R., Chua, L. O., Strachan, J. P., and Williams, R. S. (2016). History erase effect in a non-volatile memristor. *IEEE Trans. Circuits Syst. I* 63, 389–400. doi:10.1109/TCSI.2016.2525043
- Bennett, C. H. (1988). "Logical depth and physical complexity," in *The universal Turing machine, A half-century survey*. Editor R. Herken (New York, NY: Oxford University Press), 227–257.
- Berglund, C. N., and Guggenheim, H. J. (1969). Electronic properties of VO₂ near the semiconductor-metal transition. *Phys. Rev.* 185, 1022–1033. doi:10.1103/PhysRev.185.1022
- Brivio, S., Ly, D. R. B., Vianello, E., and Spiga, S. (2021). Non-linear memristive synaptic dynamics for efficient unsupervised learning in spiking neural networks. *Front. Neurosci.* 15, 580909. doi:10.3389/fnins.2021.580909
- Brown, T. D., Bohachuk, S. M., Islam, M., Kumar, S., Pop, E., and Williams, R. S. (2022a). Electro-thermal characterization of dynamical VO₂ memristors via local activity modeling. *Adv. Mat.* 34, 2205451. doi:10.1002/adma.202205451
- Brown, T. D., Kumar, S., and Williams, R. S. (2022b). Physics-based compact modeling of electro-thermal memristors: negative differential resistance, local activity, and non-local dynamical bifurcations. *Appl. Phys. Rev.* 9, 011308. doi:10.1063/5.0070558
- Brown, T. D., Zhang, A., Nitta, F. U., Grant, E. D., Chong, J. L., Zhu, J., et al. (2024). Axon-like active signal transmission. *Nature* 633, 804–810. doi:10.1038/s41586-024-07921-z
- Chua, L. O. (1969). *Introduction to nonlinear network theory*. New York, NY: McGraw-Hill.
- Chua, L. O. (2005). Local activity is the origin of complexity. *Int. J. Bifurcat. Chaos* 15, 3435–3456. doi:10.1142/S0218127405014337
- Chua, L. O. (2014). If it's pinched it's a memristor. *Semicond. Sci. Technol.* 29, 104001. doi:10.1088/0268-1242/29/10/104001
- Chua, L. O. (2015). Everything you wish to know about memristors but are afraid to ask. *Radioengineering* 24, 319–368. doi:10.13164/re.2015.0319
- Chua, L. O. (2018). Five non-volatile memristor enigmas solved. *Appl. Phys. A* 124, 563. doi:10.1007/s00339-018-1971-0
- Chua, L. O. (2022). Hodgkin-huxley equations implies edge of chaos kernel. *Jpn. J. Appl. Phys.* 61, SM0805. doi:10.35848/1347-4065/ac64e1
- Chua, L. O., Sbitnev, V., and Kim, H. (2012). Hodgkin-Huxley axon is made of memristors. *Int. J. Bifurcat. Chaos* 22, 1230011. doi:10.1142/S021812741230011X
- Cole, K. S. (1941). Rectification and inductance in the giant squid axon. *J. Gen. Physiol.* 25, 29–51. doi:10.1085/jgp.25.1.29
- Covi, E., George, R., Frascaroli, J., Brivio, S., Mayr, C., Mostafa, H., et al. (2018). Spike-driven threshold-based learning with memristive synapses and neuromorphic silicon neurons. *J. Phys. D. Appl. Phys.* 51, 344003. doi:10.1088/1361-6463/aad361
- Crane, H. D. (1960). The neuristor. *IRE Trans. Elect. Comput. EC-9*, 370–371. doi:10.1109/TEC.1960.5219861
- Crane, H. D. (1962). Neuristor – a novel device and system concept. *Proc. IRE* 50, 2048–2060. doi:10.1109/JRPROC.1962.288234
- Dittmann, R., and Strachan, J. P. (2019). Redox-based memristive devices for new computing paradigm. *Appl. Mater* 7, 110903. doi:10.1063/1.5129101
- Dogaru, R., and Chua, L. O. (1998). Edge of chaos and local activity domain of Fitzhugh-Nagumo equation. *Int. J. Bifurcat. Chaos* 8, 211–257. doi:10.1142/S0218127498000152
- Esaki, L. (1958). New phenomenon in narrow germanium p-n junctions. *Phys. Rev.* 109, 603–604. doi:10.1103/PhysRev.109.603
- Farhat, N. H., and Eldefrawy, M. H. (1993). Bifurcating neuron: characterization and dynamics. *Proc. SPIE* 1773, 23–35. doi:10.1117/12.983185
- Freire, E., Ponce, E., and Ros, J. (1999). Limit cycle bifurcation from center in symmetric piecewise-linear systems. *Int. J. Bifurcat. Chaos* 9, 895–907. doi:10.1142/S0218127499000638
- Grobman, D. (1959). Homeomorphisms of systems of differential equations. *Dokl. Akad. Nauk.* 128, 880–881. (in Russian).
- Guckenheimer, J., and Holmes, P. (1983). *Nonlinear oscillations, dynamical systems, and bifurcations of vector fields*. New York, NY: Springer-Verlag.
- Hartman, P. (1960). A lemma in the theory of structural stability of differential equations. *Proc. Amer. Math. Soc.* 11, 610–620. doi:10.1090/s0002-9939-1960-0121542-7
- Hastings, S. P. (1974). The existence of periodic solutions to Nagumo's equation. *Quart. J. Math. Oxf. Ser.* 25, 369–378. doi:10.1093/qmath/25.1.369
- Hodgkin, A. L., and Huxley, A. F. (1952). A quantitative description of membrane current and its application to conduction and excitation in nerve. *J. Physiol.* 117, 500–544. doi:10.1113/jphysiol.1952.sp004764
- Hong, B. (2022). Phase plane and slope field apps. Available online at: <https://github.com/MathWorks-Teaching-Resources/Phase-Plane-and-Slope-Field/releases/tag/v1.1.1>.
- Ignatov, M., Ziegler, M., Hansen, M., Petraru, A., and Kohlstedt, H. (2015). A memristive spiking neuron with firing rate coding. *Front. Neurosci.* 9, 376. doi:10.3389/fnins.2015.00376
- Ilyashenko, Yu. (2002). Centennial history of Hilbert's 16th problem. *B Am. Math. Soc.* 39, 301–355. doi:10.1090/s0273-0979-02-00946-1
- Izhikevich, E. M. (2004). Which model to use for cortical spiking neurons? *IEEE Trans. Neural Netw.* 15, 1063–1070. doi:10.1109/TNN.2004.832719
- Jager, M. F., Ott, C., Kraus, P. M., Kaplan, C. J., Pouse, W., Marvel, R. E., et al. (2017). Tracking the insulator-to-metal phase transition in VO₂ with few-femtosecond extreme UV transient absorption spectroscopy. *P. Natl. Acad. Sci. U. S. A.* 114, 9558–9563. doi:10.1073/pnas.1707602114
- Janninck, R. F., and Whitmore, D. H. (1966). Electrical conductivity and thermoelectric power of niobium dioxide. *J. Phys. Chem. Solids* 27, 1183–1187. doi:10.1016/0022-3697(66)90094-1
- Jeong, D. S., Thomas, R., Katiyar, R. S., Scott, J. F., Kohlstedt, H., Petraru, A., et al. (2012). Emerging memories: resistive switching mechanisms and current status. *Rep. Prog. Phys.* 75, 076502. doi:10.1088/0034-4885/75/7/076502
- Kim, S., Du, C., Sheridan, P., Ma, W., Choi, S., and Lu, W. D. (2015). Experimental demonstration of a second-order memristor and its ability to bio-realistically implement synaptic plasticity. *Nano Lett.* 15, 2203–2211. doi:10.1021/acs.nanolett.5b00697
- Kriegsmann, G. A. (1987). The rapid bifurcation of the Wien bridge oscillator. *IEEE Trans. Circuits Syst.* 34, 1093–1096. doi:10.1109/TCS.1987.1086245

Publisher's note

All claims expressed in this article are solely those of the authors and do not necessarily represent those of their affiliated organizations, or those of the publisher, the editors and the reviewers. Any product that may be evaluated in this article, or claim that may be made by its manufacturer, is not guaranteed or endorsed by the publisher.

- Krupa, M., and Szmolyan, P. (2001). Relaxation oscillation and Canard explosion. *J. Differ. Equations* 174, 312–368. doi:10.1006/jdeq.2000.3929
- Liang, Y., Zhu, Q., Wang, G., Nath, S. K., Lu, H. H.-C., Nandi, S. K., et al. (2022). Universal dynamics analysis of locally-active memristors and its applications. *IEEE Trans. Circuits Syst. I* 69, 1278–1290. doi:10.1109/TCSI.2021.3130938
- Mannan, Z. I., Choi, H., and Kim, H. (2016). Chua cossage memristor oscillator via Hopf bifurcation. *Int. J. Bifurcat. Chaos* 26, 1630009. doi:10.1142/S0218127416300093
- Mannan, Z. I., Choi, H., Rajamani, V., Kim, H., and Chua, L. O. (2017). Chua cossage memristor: phase portraits, basin of attraction, and coexisting pinched hysteresis loops. *Int. J. Bifurcat. Chaos* 27, 1730011. doi:10.1142/S0218127417300117
- Marsden, J. E., and McCracken, M. (1976). *The Hopf bifurcation and its applications*. New York, NY: Springer-Verlag.
- Messaris, I., Brown, T. D., Demirkol, A. S., Ascoli, A., Chawa, M. M. A., Williams, R. S., et al. (2021). NbO₂-Mott memristor: a circuit-theoretic investigation. *IEEE Trans. Circuits Syst. I* 68, 4979–4992. doi:10.1109/TCSI.2021.3126657
- Moon, K., Cha, E., Park, J., Gi, S., Chu, M., Baek, K., et al. (2015). High density neuromorphic system with Mo/Pr_{0.7}Ca_{0.3}MnO₃ synapse and NbO₂ IMT oscillator neuron. *Int. Electron Devices Meet. Wash. D.C. IEEE* 17.6, 1–17.6.4. doi:10.1109/IEDM.2015.7409721
- Nagumo, J., Arimoto, S., and Yoshizawa, S. (1962). An active pulse transmission line simulating nerve axon. *Proc. IRE* 50, 2061–2070. doi:10.1109/JRPROC.1962.288235
- Newcomb, R. W., and Sellami, L. (1999). “Multivibrators,” in *Wiley encyclopedia of electrical and electronics engineering*. Editor J. G. Webster (New York, NY: Wiley, 14, 62–71. doi:10.1002/047134608x.w2265
- Noé, P., Verdy, A., d’Acapito, F., Dory, J.-B., Bernard, M., Navarro, G., et al. (2020). Toward ultimate nonvolatile resistive memories: the mechanism behind ovonic threshold switching revealed. *Sci. Adv.* 6, eaay2830. doi:10.1126/sciadv.aay2830
- Oh, D.-W., Ko, C., Ramanathan, S., and Cahill, D. G. (2010). Thermal conductivity and dynamic heat capacity across the metal-insulator transition in thin film VO₂. *Appl. Phys. Lett.* 96, 151906. doi:10.1063/1.3394016
- Ovshinsky, S. R. (1968). Reversible electrical switching phenomena in disordered structures. *Phys. Rev. Lett.* 21, 1450–1453. doi:10.1103/PhysRevLett.21.1450
- Pearson, S. O., and Anson, H. St. G. (1921). The neon tube as a means of producing intermittent currents. *Proc. Phys. Soc. Lond.* 34, 204–212. doi:10.1088/1478-7814/34/1/341
- Perko, L. (1991). *Differential equations and dynamical systems*. New York, NY: Springer-Verlag.
- Pershin, Y. V., and Slipko, V. A. (2019). Bifurcation analysis of a TaO memristor model. *J. Phys. D: Appl. Phys.* 52, 505304. doi:10.1088/1361-6463/ab4537
- Pickett, M. D., Medeiros-Ribeiro, G., and Williams, R. S. (2013). A scalable neuristor built with Mott memristors. *Nat. Mat.* 12, 114–117. doi:10.1038/nmat3510
- Pickett, M. D., and Williams, R. S. (2012). Sub-100 fJ and sub-nanosecond thermally driven threshold switching in niobium oxide crosspoint nanodevices. *Nanotechnology* 23, 215202. doi:10.1088/0957-4484/23/21/215202
- Pickett, M. D., and Williams, R. S. (2013). Phase transitions enable computational universality in neuristor-based cellular automata. *Nanotechnology* 24, 384002. doi:10.1088/0957-4484/24/38/384002
- Prigogine, I., and Nicolis, G. (1967). On symmetry-breaking instabilities in dissipative systems. *J. Chem. Phys.* 46, 3542–3550. doi:10.1063/1.1841255
- Prinz, V. Y., Mutilin, S. V., Yakovkina, L. V., Gutakovskii, A. K., and Komonov, A. I. (2020). A new approach to the fabrication of VO₂ nanoswitches with ultra-low energy consumption. *Nanoscale* 12, 3443–3454. doi:10.1039/c9nr08712e
- Ridley, B. K. (1963). Specific negative resistance in solids. *Proc. Phys. Soc.* 82, 954–966. doi:10.1088/0370-1328/82/6/315
- Rinzel, J., and Miller, R. N. (1980). Numerical calculation of stable and unstable periodic solutions to the Hodgkin-Huxley equations. *Math. Biosci.* 49, 27–59. doi:10.1016/0025-5564(80)90109-1
- Rotstein, H. G., Coombes, S., and Gheorghie, A. M. (2012). Canard-like explosion of limit cycles in two-dimensional piecewise-linear models of Fitzhugh-Nagumo type. *SIAM J. Appl. Dyn. Syst.* 11, 135–180. doi:10.1137/100809866
- Shashkin, Y. A. (1991). *Fixed points, vol. Mathematical world, 2*. Providence, RI: American Mathematical Society.
- Smale, S. (1976). “A mathematical model of two cells via turing’s equation,” in *The Hopf bifurcation and its applications*. Editors J. E. Marsden, and M. McCracken (New York, NY: Springer-Verlag), 354–367.
- Stoliar, P., Tranchant, J., Corraze, B., Janod, E., Besland, M.-P., Tesler, F., et al. (2017). A leaky-integrate-and-fire neuron analog realized with a mott insulator. *Adv. Funct. Mat.* 27, 1604740. doi:10.1002/adfm.201604740
- Strukov, D. B., Snider, G. S., Stewart, D. R., and Williams, R. S. (2008). The missing memristor found. *Nature* 453, 80–83. doi:10.1038/nature06932
- Troy, W. C. (1978). The bifurcation of periodic solutions in the hodgkin-huxley equations. *Q. Appl. Math.* 36, 73–83. doi:10.1090/qam/472116
- Turing, A. M. (1952). The chemical basis of morphogenesis. *Phil. Trans. R. Soc. Lond. B* 237, 37–72. doi:10.1098/rstb.1952.0012
- van der Pol, B., and van der Mark, J. (1928). LXXII. The heartbeat considered as a relaxation oscillation, and an electrical model of the heart. *Phil. Mag.* 6 (Suppl. 1), 763–775. doi:10.1080/14786441108564652
- Wang, Z., Joshi, S., Savelev, S., Song, W., Midya, R., Li, Y., et al. (2018). Fully memristive neural networks for pattern classification with unsupervised learning. *Nat. Electron.* 1, 137–145. doi:10.1038/s41928-018-0023-2
- Wang, Z., Joshi, S., Savelev, S. E., Jiang, H., Midya, R., Lin, P., et al. (2017). Memristors with diffusive dynamics as synaptic emulators for neuromorphic computing. *Nat. Mat.* 16, 101–108. doi:10.1038/nmat4756
- Waser, R., Dittmann, R., Staikov, G., and Szot, K. (2009). Redox-based resistive switching memories – nanoionic mechanisms, prospects, and challenges. *Adv. Mat.* 21, 2632–2663. doi:10.1002/adma.200900375
- Yi, W. (2022). Active memristor based spiking neuromorphic circuit for motion detection, 238,335.
- Yi, W., and Cruz-Albrecht, J. (2019). “Scalable, energy-efficient, and high-throughput all-memristor neuromorphic processor,” in *DARPA ERI summit (detroit, MI: darpa)*. Available online at: https://eri-summit.darpa.mil/docs/ERIPoster_Materials_FRANC_HRL.pdf.
- Yi, W., Tsang, K. K., Lam, S. K., Bai, X., Crowell, J. A., and Flores, E. A. (2018). Biological plausibility and stochasticity in scalable VO₂ active memristor neurons. *Nat. Commun.* 9, 4661. doi:10.1038/s41467-018-07052-w
- Yi, W., Tsang, K. K., Lam, S. K., Bai, X., Crowell, J. A., and Flores, E. A. (2019). Active memristor neurons for neuromorphic computing. *Int. Electron Devices Meet. (San Francisco, CA IEEE)* 22.7, 22.7.1–22.7.4. doi:10.1109/IEDM19573.2019.8993550